

**Dosimetric Verification
of Intensity Modulated Radiotherapy
with an Electronic Portal Imaging Device**

Cover drawn by Andy Bahnert, a colleague and radiotherapy technician at the Erasmus MC/Daniel den Hoed Cancer Center

ISBN: 90-8559-073-6

Druk: Optima Rotterdam

© Copyright: 2002 America Association of Physicists in Medicine (chapter 2)

2003 IOP Publishing Ltd. (chapter 3)

2002 America Association of Physicists in Medicine (chapter 4)

2003 America Association of Physicists in Medicine (chapter 6)

2004 Elsevier Inc. (chapter 7)

**Dosimetric Verification
of Intensity Modulated Radiotherapy
with an Electronic Portal Imaging Device**

Verificatie van IMRT dosis afgifte met behulp van een EPID

PROEFSCHRIFT

ter verkrijging van de graad van doctor
aan de Erasmus Universiteit Rotterdam
op gezag van de rector magnificus
Prof.dr. S.W.J. Lamberts
en volgens besluit van het College voor Promoties.

De openbare verdediging zal plaatsvinden op
woensdag 7 september 2005 om 11:45 uur
door

Sandra Correia Vieira
geboren te Lissabon, Portugal

Promotiecommissie

Promotor: Prof.dr. P.C. Levendag

Overige leden: Prof.dr.ir. C.J. Snijders
Prof.dr. A. Vossepoel
Prof.dr. M. van Herk

Copromotor: Dr. B.J.M. Heijmen

This thesis has been prepared at the Department of Radiation Oncology, Division of Medical Physics, Erasmus MC/Daniel den Hoed Cancer Center, Rotterdam, The Netherlands.

The work in this thesis was made possible by the Fundação para a Ciência e a Tecnologia.

Address for correspondence:

S. Vieira, Department of Radiation Oncology, Division of Medical Physics,
Erasmus MC/Daniel den Hoed Cancer Center, Groene Hilledijk 301, 3075 EA
Rotterdam, The Netherlands.

Phone: +31.10.4391801. Fax: +31.10.4391012. E-mail: s.vieira@erasmusmc.nl

Extracto de “Há Metafísica Bastante em Não Pensar em Nada”

O mistério das cousas? Sei lá o que é mistério!

O único mistério é haver quem pense no mistério.

Quem está ao sol e fecha os olhos,

Começa a não saber o que é o sol

E a pensar muitas cousas cheias de calor.

Mas abre os olhos e vê o sol,

E já não pode pensar em nada,

Porque a luz do sol vale mais que os pensamentos

De todos os filósofos e de todos os poetas.

A luz do sol não sabe o que faz

E por isso não erra e é comum e boa

Alberto Caeiro, pseudónimo de Fernando Pessoa (1888-1935)

Dedicado ao João, à Regina, à Sónia e ao Joep

CONTENTS

CONTENTS.....	i
Chapter 1. General introduction.....	1
1.1 Radiotherapy.....	1
1.2 External radiotherapy.....	1
1.3 Modulated beams.....	2
1.4 The Electronic portal imaging device (EPID).....	3
1.5 Purpose of the thesis.....	4
1.6 References.....	5
Chapter 2. Portal dose image prediction for dosimetric treatment verification in radiotherapy.II.An algorithm for wedged beams.	9
2.1 Abstract.....	9
2.2 Introduction	9
2.3 Method of transmission prediction	12
2.4 Derivation of the functions used for transmission prediction.....	15
2.5 Comparison of predicted and measured transmissions	22
2.6 Discussion.....	25
2.7 Acknowledgments	26
2.8 References.....	26
Chapter 3. Dosimetric verification of X-ray fields with steep dose gradients using an electronic portal imaging device	29
3.1 Abstract.....	29
3.2 Introduction	30
3.3 Materials and methods.....	30
3.4 Results and discussion	36
3.5 Conclusions.....	41
3.6 Acknowlegments	41
3.7 References.....	42
Chapter 4. Fast and accurate leaf verification for dynamic multileaf collimation using an EPID	43
4.1 Abstract.....	43
4.2 Introduction	43
4.3 Materials and Methods	45
4.4 Results.....	51
4.5 Discussion.....	54
4.6 Conclusions.....	55
4.7 Acknowlegments	55
4.8 References.....	56
Chapter 5. Fast, daily linac verification for segmented IMRT using electronic portal imaging	59

5.1 Abstract.....	59
5.2 Introduction	60
5.3 Materials and methods.....	61
5.4 Results.....	68
5.5 Discussion.....	71
5.6 Conclusions.....	74
5.7 Acknowledgments	75
5.8 References.....	75
Chapter 6. Two-dimensional measurement of photon beam attenuation by the treatment couch and immobilization devices using an electronic portal imaging device.....	
6.1 Abstract.....	77
6.2 Introduction	77
6.3 Materials and Methods	80
6.4 Results.....	85
6.5 Discussion.....	88
6.6 Conclusions.....	90
6.7 Acknowledgments	91
6.8 References.....	91
Chapter 7. SIFT: a method to verify the IMRT fluence delivered during patient treatment using an electronic portal imaging device.....	
7.1 Abstract.....	93
7.2 Introduction	94
7.3 Materials and Methods	95
7.4 Results.....	100
7.5 Discussion.....	109
7.6 Conclusions.....	112
7.7 Acknowledgments	113
7.8 References.....	113
Chapter 8. General discussion.....	
8.1 Introduction	117
8.2 Dosimetry with a CCD-camera based EPID	117
8.3 Current status of dosimetry with commercial flat-panel systems.....	120
8.4 Dosimetric quality assurance protocols for IMRT.....	122
8.5 Is validation of individual IMRT treatments necessary?	127
8.6 Conclusions.....	128
8.7 References.....	128
Chapter 9. Samenvatting.....	
9.1 Inleiding.....	133
9.2 De EPID en de dosis verificatie van gemoduleerde stralenbundels	134
9.3 MLC kwaliteitscontrole.....	135
9.4 Patiëntbehandelingen met IMRT	136

List of abbreviations and symbols	137
Acknowledgments.....	139
Curriculum vitae	143

CHAPTER 1. GENERAL INTRODUCTION

1.1 Radiotherapy

Cancer is the uncontrolled proliferation and spread of cells and may affect almost any tissue of the body. Most cancer diseases are treated by surgery, ionising radiation (radiotherapy), and/or using drugs (chemotherapy). The first cancer patient was treated with radiotherapy in Chicago in 1896, less than one month after Röntgen's discovery of X-rays. Since then, millions of patients have undergone radiotherapy, and cure rates have increased steadily. The critical target of radiotherapy is the DNA of the tumour cell. Radiation may cause deletions, substitutions, and/or actual breaks in the DNA chain. The reproductive death of the tumour cell occurs when the radiation damage is not repaired (correctly), causing abnormalities in the chromosomes. In radiotherapy, the source of radiation can be located outside the patient (external radiotherapy), or within the tumour (brachytherapy). In external radiotherapy, the radiation beams (mostly megavoltage x-rays or electrons) are delivered by a linear accelerator (Fig. 1-1). In this treatment modality, the patient is irradiated from several angles in order to achieve a homogenous dose in the tumour and to spread (and thus reduce) the dose in the healthy organs located in the path of the radiation beam.

1.2 External radiotherapy

Many steps are involved in the external beam radiotherapy process. These steps can be divided into two different groups: preparation and treatment delivery. Often, the preparation phase starts with the production of immobilisation devices to accurately position and immobilise the patient at the treatment couch during daily treatments. Next, a Computerized Tomography (CT) scan is made of the patient in the treatment position (using the immobilization devices, if existent) to obtain a 3D representation of the patient anatomy. To define a common point of reference between the actual anatomy and its 3D representation, ink marks are made on the immobilization device or in the patient's skin (tattoos), which are made visible in the CT-scan by applying small radioopaque markers. The CT-scans is then transferred to the treatment planning

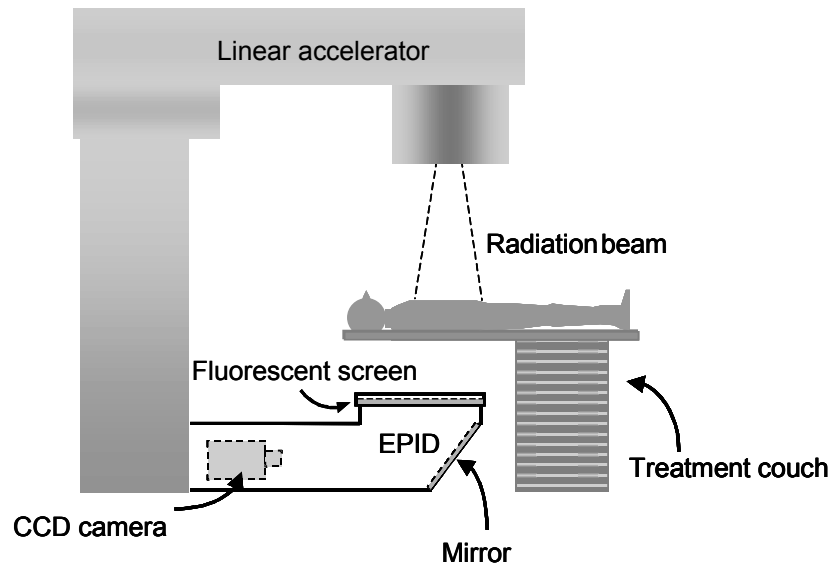


Figure 1-1 Linear accelerator with an electronic portal imaging device (EPID) attached. The EPID is equipped with fluorescent screen, mirror, and CCD camera.

computer system (TPS). A crucial step is now the accurate delineation of the tumour on the CT-scan by the radiation oncologist, and the dose prescription to the tumour and organs at risk. Based on the delineated structures and the dose prescription, a treatment plan is performed by optimising the number of beams used, the beam angles and corresponding weights, and beam energy. After approval of the resulting dose distribution by the radiation oncologist, the treatment preparation phase ends, and the patient may start with the treatment. In this phase, the markings on the patient's skin or on the immobilization device are used to correctly position the patient in relation to the treatment beams. The ultimate goal is to exactly mimic the set-up of the CT data set used in the treatment plan. Depending on the type of cancer, the treatment delivery may vary from one or two daily sessions, up to seven weeks with daily or twice daily sessions.

1.3 Modulated beams

External beam radiotherapy is often performed with flat, static treatment beams (see Fig 1-2a). However, due to the location and/or the shape of the tumour, it is not always possible to achieve a homogenous dose in the tumour and simultaneously spare the surrounding normal tissue structures using these beams. In these cases, (non-

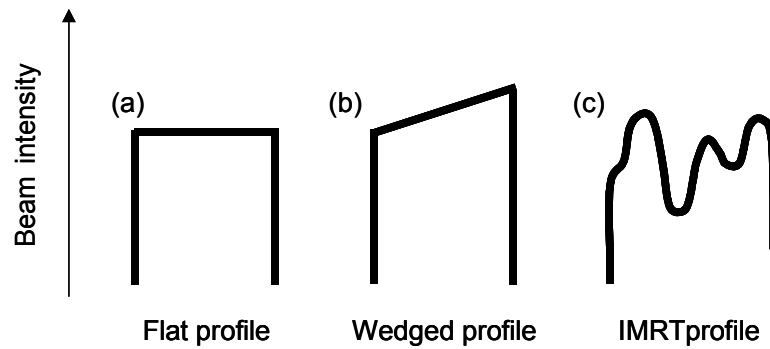


Figure 1-2 Schematic view of (a) a flat beam profile, (b) a wedged beam profile, and (c) a highly modulated beam profile.

flat) modulated beams may be used. The simplest way to modulate a radiation beam is inserting a metal wedge filter in between the radiation focus and the patient. The intensity profile entering the patient with a wedged field is schematically shown in Fig. 1-2b. A decade ago, Intensity Modulated Radiotherapy (IMRT) was introduced in the clinical practice. In this technique, the intensity profiles are tailored to the treatment requirements of the individual patient (see Fig. 1-2c). Generally IMRT fields are delivered with a multi-leaf collimator (MLC). This computer-controlled mechanical beam shaping device is attached to the head of the accelerator and consists of an assembly of metal “fingers” or leaves. The MLC can be made out of 120 movable leaves with 0.5 and/or 1.0 cm diameter. For each beam direction, the optimised intensity profile is realised by sequential delivery of various subfields with optimised shapes and weights. From one subfield to the next, the leaves may move with the X-ray beam on (dynamic multileaf collimation (DMLC)) or with the beam off (segmented multileaf collimation (SMLC), also known as “step and shoot”). In both IMRT techniques, verification of the complex 3D dose distributions delivered to the patient is mandatory, and this will be addressed in this thesis.

1.4 The Electronic portal imaging device (EPID)

An EPID is used to acquire a digital transmission radiograph of the patient using megavoltage treatment beams (Fig. 1-1). EPIDs were introduced in clinical practice in the mid 80s to verify the position of the patient at the time of treatment. With the increasing use of IMRT techniques, EPIDs are now more often also used as a tool for

dose delivery verification.¹⁻⁹ There are several types of EPID detectors used in radiotherapy, from camera-based systems to the more recent amorphous silicon detectors.¹⁰⁻¹⁶ In this thesis, a fluoroscopic Theraview NT camera-based EPID (Cablon Medical, Leusden, The Netherlands) is used for IMRT dose delivery verification. The latter EPID is equipped with a fluorescent screen, a mirror, and a cooled CCD camera (see Fig. 1-1).^{10,16}

1.5 Purpose of the thesis

A relatively small error ($\approx 5\%$) in the delivered dose may (seriously) harm the patient; a too low dose may jeopardize the probability of cure, whereas a too high dose may cause serious damage to healthy tissues surrounding the tumor.¹⁷⁻²³ Modern radiotherapy is a high-tech modality for treatment of cancer patients, involving CT, Magnetic Resonance imaging (MRI), dedicated 3-dimensional treatment planning, image guidance and IMRT. The objective of this study was to analyse the important aspects of IMRT dose delivery with EPIDs, and to develop verification protocols. One of the challenges was to find methods precise enough to detect small relevant deviations ($< 5\%$) in the delivered dose. To allow routine clinical use, the developed tools had to be robust, accurate, easy to use and fast.

In chapter 2, a method is presented for portal dose image (PDI) prediction with wedged beams. In our institute, a method has already been developed and clinically implemented for open fields.²⁴ In this chapter, it is shown that a similar algorithm can be used when 2D beam modulation is applied. This gives an indication that dosimetry for more complex modulated beams is achievable without introducing significant changes. In chapter 3, beam modulation is taken a step further, and highly peaked modulated fields are studied. A function is developed to correct for the (short-range) differences in lateral electron and optical photon transport between water and the metal plate with the fluorescent layer in the EPID, by improving the response of the EPID for highly peaked profiles. This function is derived by comparing EPID measurements with film and ionisation chamber measurements. The EPID is a suitable dose verification tool for IMRT, even when highly peaked beams are used.

In the next chapters, several stages of the developed QA protocol for IMRT are addressed.

In chapter 4 and 5, more focus is given to the part of the QA protocol that concerns the accelerator. In these chapters, fast daily tests to verify the performance of the MLC

for SMLC and DMLC deliveries are proposed. Due to the fact that dose deviations of several percent can be caused by uncertainties in leaf position less than a millimetre, the accuracy of leaf positioning is crucial for the outcome of the IMRT treatment.

When we performed our QA protocol measurements prior to the IMRT treatment, high attenuation of the treatment couch and the immobilisation devices was encountered. In chapter 6, this attenuation is investigated using the EPID. It was found that, even with commercially available carbon fibre inserts, beam attenuation of up to 15% was possible in some parts of the couch. This study showed that, although patients have been lying on the couch during treatment delivery since the early years of radiotherapy, intersections between the treatment beam and the couch and/or the patient immobilisation device have become more frequent with the introduction of IMRT.

The last stage of our QA protocol concerns the dose delivery to the patient. During treatment, large dose differences may be found between the measured PDI and the predicted PDI, which can be either due to deviations in the radiation beam or due to changes in the patient geometry between the planning CT and treatment delivery (e.g. differences in patient positioning or internal organ motion).^{1-3,5} In chapter 7, a new technique, called the Split IMRT Field Technique (SIFT), is presented to verify the delivered fluence independent of changes in patient geometry. This method is based on splitting the IMRT field into a static (non-modulated) field and a residual modulated field. By separating patient geometry errors from radiation beam related errors, a fundamental limitation for any transmission dose measurement is overcome.

Finally in chapter 8, a general discussion is presented on quality assurance in IMRT.

1.6 References

- ¹M. Essers, J. H. Lanson, G. Leunens, et al., "The accuracy of CT-based inhomogeneity corrections and in vivo dosimetry for the treatment of lung cancer," *Radiother. Oncol.* **37**, 199-208 (1995).
- ²R. Boellaard, M. van Herk, H. Uiterwaal, et al., "First clinical tests using a liquid-filled electronic portal imaging device and a convolution model for the verification of the midplane dose," *Radiother. Oncol.* **47**, 303-12 (1998).
- ³M. Kroonwijk, K. L. Pasma, S. Quint, P. C. M. Koper, A. G. Visser, and B. J. M. Heijmen, "In vivo dosimetry for prostate cancer patients using an electronic portal imaging device (EPID): detection of internal organ motion," *Radiother. Oncol.* **49**, 125-32 (1998).
- ⁴K. L. Pasma, M. L. P. Dirkx, M. Kroonwijk, A. G. Visser, and B. J. M. Heijmen, "Dosimetric verification of intensity modulated beams produced with dynamic multileaf collimation using an electronic portal imaging device," *Med. Phys.* **26**, 2373-78 (1999).

- ⁵K. L. Pasma, M. Kroonwijk, S. Quint, A. G. Visser, and B. J. M. Heijmen, "Transit dosimetry with an electronic portal imaging device (EPID) for 115 prostate cancer patient," *Int. J. Rad. Oncol. Biol. Phys.* **45**, 1297-03 (1999).
- ⁶J. Chang, G. S. Mageras, C. S. Chui, C. C. Ling, and W. Lutz, "Relative profile and dose verification of intensity-modulated radiation therapy," *Int. J. Radiat. Oncol. Biol. Phys.* **47**, 231-40 (2000).
- ⁷A. Van Esch, B. Vanstraelen, J. Verstraete, G. Kutcher, and D. Huyskens, "Pre-treatment dosimetric verification by means of a liquid-filled electronic portal imaging device during dynamic delivery of intensity modulated treatment fields," *Radiother. Oncol.* **60**, 181-90 (2001).
- ⁸B. Warkentin, S. Steciw, S. Rathee, and B. G. Fallone, "Dosimetric IMRT verification with a flat-panel EPID," *Med. Phys.* **30**, 3143-55 (2003).
- ⁹S. C. Vieira, M. L. Dirkx, B. J. Heijmen, and H. C. de Boer, "SIFT: a method to verify the IMRT fluence delivered during patient treatment using an electronic portal imaging device," *Int. J. Radiat. Oncol. Biol. Phys.* **60**, 981-93 (2004).
- ¹⁰J. C. J. de Boer, B. J. M. Heijmen, K. L. Pasma, and A. G. Visser, "Characterization of a high elbow, fluoroscopic electronic portal imaging device for portal dosimetry," *Phys. Med. Biol.* **45**, 197-216 (2000).
- ¹¹A. G. Glendinning, S. G. Hunt, and D. E. Bonnett, "Recording accelerator monitor units during electronic portal imaging: application to collimator position verification during IMRT," *Phys. Med. Biol.* **46**, N159-67 (2001).
- ¹²L. S. Ploeger, M. H. Smitsmans, K. G. Gilhuijs, and M. van Herk, "A method for geometrical verification of dynamic intensity modulated radiotherapy using a scanning electronic portal imaging device," *Med. Phys.* **29**, 1071-9 (2002).
- ¹³J. Chang, G. S. Mageras, and C. C. Ling, "Evaluation of rapid dose map acquisition of a scanning liquid-filled ionization chamber electronic portal imaging device," *Int. J. Radiat. Oncol. Biol. Phys.* **55**, 1432-45 (2003).
- ¹⁴A. Van Esch, T. Depuydt, and D. P. Huyskens, "The use of an aSi-based EPID for routine absolute dosimetric pre-treatment verification of dynamic IMRT fields," *Radiother. Oncol.* **71**, 223-34 (2004).
- ¹⁵L. N. McDermott, R. J. Louwe, J. J. Sonke, M. van Herk, and B. J. Mijnheer, "Dose-response and ghosting effects of an amorphous silicon electronic portal imaging device," *Med. Phys.* **31**, 285-95 (2004).
- ¹⁶E. M. Franken, J. C. J. de Boer, J. C. Barnhoorn, and B. J. M. Heijmen, "Characteristics relevant to portal dosimetry of a cooled CCD camera-based EPID," *Med. Phys.* **31**, 2549-51 (2004).
- ¹⁷International Commission on Radiation Units and Measurements (ICRU), "Determination of absorbed dose in a patient irradiated by means of X or gamma rays in Radiotherapy procedures," Report nr. **24** (1976).
- ¹⁸M. Goitein, "Nonstandard deviations," *Med. Phys.* **10**, 709-711 (1983).
- ¹⁹A. Dutreix, "When and how can we improve precision in radiotherapy?," *Radiother. Oncol.* **2**, 275-92 (1984).
- ²⁰B. J. Mijnheer, J. J. Battermann, and A. Wambersie, "What degree of accuracy is required and can be achieved in photon and neutron therapy?," *Radiother. Oncol.* **8**, 237-52 (1987).
- ²¹A. Brahme, "Dosimetric precision requirements in radiation therapy," *Acta Radiol. Oncol.* **23**, 379-91 (1984).

-
- ²²A. Brahme, "Accuracy requirements and quality assurance of external beam therapy with photons and electrons," *Acta Oncologica suppl.* nr.1 **2**, 9-15 (1988).
- ²³A. L. Boyer and T. Schultheiss, "Effects of dosimetric and clinical uncertainty on complication- free local tumor control," *Radiother. Oncol.* **11**, 65-71 (1988).
- ²⁴K. L. Pasma, B. J. M. Heijmen, M. Kroonwijk, and A. G. Visser, "Portal dose image (PDI) prediction for dosimetric treatment verification in radiotherapy I. An algorithm for open beams," *Med. Phys.* **25**, 830–840 (1998).

CHAPTER 2. PORTAL DOSE IMAGE PREDICTION FOR DOSIMETRIC TREATMENT VERIFICATION IN RADIOTHERAPY. II. AN ALGORITHM FOR WEDGED BEAMS.

K L Pasma, S C Vieira, B J M Heijmen

Med. Phys. **29**, 925-931, 2002

2.1 Abstract

A method is presented for calculation of a two-dimensional function, $T_{\text{wedge}}(x,y)$, describing the transmission of a wedged photon beam through a patient. This is an extension of the method that we have published for open (nonwedged) fields [Med. Phys. 25, 830–840 (1998)]. Transmission functions for open fields are being used in our clinic for prediction of portal dose images (PDI, i.e., a dose distribution behind the patient in a plane normal to the beam axis), which are compared with PDIs measured with an electronic portal imaging device (EPID). The calculations are based on the planning CT scan of the patient and on the irradiation geometry as determined in the treatment planning process. Input data for the developed algorithm for wedged beams are derived from (the already available) measured input data set for transmission prediction in open beams, which is extended with only a limited set of measurements in the wedged beam. The method has been tested for a PDI plane at 160 cm from the focus, in agreement with the applied focus-to-detector distance of our fluoroscopic EPIDs. For low and high energy photon beams (6 and 23 MV) good agreement ($\sim 1\%$) has been found between calculated and measured transmissions for a slab and a thorax phantom.

2.2 Introduction

Radiotherapy treatments have become more complex due to the increased use of three-dimensional (3D) treatment planning systems and multileaf collimators. Accurate verification is therefore mandatory. In Sweden and Denmark, dosimetric treatment verification during treatment is already required by law. It is to be expected

that this will become mandatory in other countries too. Traditionally, *in vivo* dosimetry is performed with diodes and TLDs. These devices only provide dose to points and positioning them on the entrance or exit side of the patient requires extra treatment time. Therefore, several groups have studied the application of electronic portal imaging devices (EPIDs) for dosimetric verification of treatments.¹⁻¹² Our approach includes the comparison of portal dose images (PDI, i.e., a dose distribution behind the patient in a plane normal to the beam axis), as derived from measured portal images, with predicted PDIs, which can reveal problems like incorrect (dosimetric) performance of the treatment unit and deviations between the actual patient anatomy during treatment and the anatomy according to the planning CT scan. Comparisons in the first treatment fractions may be useful to determine whether the anatomy according to the planning CT scan will be representative for the average anatomy during the fractionated treatment.¹³ In case of persisting deviations, a new planning CT scan and treatment plan might be generated. In a clinical study with 115 prostate cancer patients we have found that the difference between the average measured on-axis portal dose and the predicted portal dose was $0.4 \pm 3.4\%$ and $-1.5 \pm 2.4\%$ for the anterior field and the open, lateral field segment, respectively. Some large differences were attributed to variations in rectal filling. For seven patients the planning CT scan was found not to be representative.¹³ Large off-axis differences between measured and predicted portal doses may point at organ motion.^{14,15}

In our institute we use fluoroscopic, CCD camera based EPIDs for portal dosimetry.^{11,12,16,17} It was demonstrated that these systems may be used for accurate dose measurements in open^{11,12,16} and wedged fields,¹¹ and in intensity modulated fields, produced with dynamic multileaf collimation.^{11,17} To reduce the detection of electrons generated in the patient when irradiated with a high energy photon beam, our EPIDs are always operated with an extra 1 mm stainless steel slab on top of the standard fluorescent screen (1.65 mm stainless steel¹¹ or 2 mm brass¹⁶ with a coated layer of gadolinium oxysulfide). Image quality is hardly affected by this additional layer so that acquired images can be used for patient set-up verification and portal dose verification simultaneously.

In clinical practice it is convenient to have a large clearance between the patient and the EPID. Therefore, EPIDs are generally positioned at a (fixed) distance between 150 and 200 cm from the focus. Due to the resulting large air gap between the exit plane of the patient and the detector, a standard treatment planning system cannot be used for accurate prediction of PDIs. A few groups have developed and tested dedicated algorithms for prediction of PDIs in open (nonwedged) beams.^{4,5,18,19,20,21} Some

models are based on measured input data, others rely on Monte Carlo simulations. None of these methods have been tested for prediction of PDIs in wedged beams. The aim of the work presented in this paper was to develop an accurate (~2%) algorithm for PDI prediction for irradiations with wedges. The method has been implemented and tested for a PDI plane at 160 cm from the focus, which is equal to the fixed focus-to-detector distance of a Philips SRI-100 EPID (Philips Medical Systems, Crawley, UK).

The developed algorithm for wedged beams is very similar to the algorithm for open beams.¹⁹ It is based on the measured input database for the open beam, extended with a limited set of measured input data for the wedged beam. For the prediction of a PDI in a wedged beam we use the following equation:

$$D_{p,wedge}(x,y) = T_{wedge}(x,y) \cdot D_{p,0,wedge}(x,y) \quad 2-1$$

with $D_{p,wedge}(x,y)$ the portal dose below the patient in point (x,y) of the PDI, $T_{wedge}(x,y)$ a transmission function, and $D_{p,0,wedge}(x,y)$ the portal dose that would have occurred in point (x,y) of the PDI in the absence of the patient. Calculation of $D_{p,0,wedge}(x,y)$ is fairly simple as it is a wedged dose distribution in a water tank at the water equivalent depth of the EPID (around depth of maximum dose in water). As for the open beams¹⁹ we will use the pencil beam algorithm as implemented in the CadPlan treatment planning system for this purpose.²² In this paper we focus on the algorithm that was developed for calculation of transmission functions $T_{wedge}(x,y)$.

As is clear from Eq. (2-1), $T_{wedge}(x,y)$, is the ratio of the wedge beam profile with the patient in the beam and the profile of the same beam in absence of the patient. Nevertheless, as will be explained below, even for a flat absorber, $T_{wedge}(x,y)$ is not constant, which is due to scatter radiation and the impact of the wedge on the beam penetrating quality.

In this paper, the position coordinates x and y are measured in a right-handed system, where the positive y axis points towards the gantry and the origin $(0,0)$ coincides with the isocenter (conforming to IEC 1217). Field sizes and distances are all defined in the plane through the isocenter (i.e., at 100 cm from the focus). Point (x,y) refers to a point in the PDI plane (at 160 cm from the focus), which coordinates are defined by the intersection point of the corresponding ray line and the isocenter plane. The subscript

"wedge" refers to a wedged beam, while no subscript means open (nonwedged) beam. Reported uncertainties are ± 1 standard deviation (σ).

2.3 Method of transmission prediction

The transmission in point (x,y) consists of a primary component, due to photons that reach the detector without interacting with the patient, and a scatter component that stems from photons generated by interactions in the patient. The primary and scatter components, $T^P(x,y)$ and $T^S(x,y)$, of the transmission $T(x,y)$ are calculated separately and subsequently added, i.e.,

$$T(x,y) = T^P(x,y) + T^S(x,y). \quad 2-2$$

The algorithms for the calculation of $T^P(x,y)$ and $T^S(x,y)$ are based on data derived from measured transmissions through flat, water equivalent (polystyrene) phantoms (see Sec. III). To be able to use these data for the prediction of the transmission through an (inhomogeneous) patient, the patient anatomy as described by the planning CT scan is substituted by an (imaginary) equivalent homogeneous phantom (EHP) consisting of polystyrene.¹⁹ For each treatment beam, a separate EHP is calculated. For each ray line from the source to point (x,y) , the patient and the EHP have equal (equivalent) polystyrene thicknesses and equal distances between the center of mass and the detector plane. An EHP is thus defined by two two-dimensional arrays, one with polystyrene thicknesses $t(x,y)$ and the other with distances $L(x,y)$ between the exit point of the EHP and the detector plane. The EHP is derived by tracing rays through the CT data and determining the equivalent polystyrene thicknesses along these ray lines. A recent study, using Monte Carlo simulations, has confirmed the validity of the EHP concept for PDI prediction.²³

2.3.1 Transmission prediction for open beams

For an EHP, the primary component of the transmission at point (x,y) of the PDI, positioned at a distance $r(x,y) = \sqrt{x^2 + y^2}$ from the beam axis, and corresponding to the thickness $t(x,y)$ of the EHP along the ray line through point (x,y) is calculated using

$$T^P(x,y) = C(r_{(x,y)}, t_{(x,y)}) \cdot P(t_{(x,y)}), \quad 2-3$$

with $P(t_{(x,y)})$ the on-axis primary transmission component for irradiation of a flat, polystyrene phantom with thickness $t_{(x,y)}$, and $C(r_{(x,y)}, t_{(x,y)})$ a function to account for the difference in beam quality between the beam axis and the off-axis point (x,y) . This difference is due to the off-axis softening of the beam spectrum, mostly due to the flattening filter.¹⁹

For the calculation of the scatter component of the transmission through an EHP in point (x,y) of the PDI, $T^S(x,y)$, we use

$$T^S(x,y) = \int_{(x',y') \in \text{field}} \frac{f(r_{(x',y')})}{f(r_{(x,y)})} \times s(r_{(x'-x, y'-y)}, t_{(x',y')}, L_{(x',y')}) dx' dy', \quad 2-4$$

with $s(r_{(x'-x, y'-y)}, t_{(x',y')}, L_{(x',y')})$ the scatter contribution at point (x,y) due to the imaginary EHP-column connected to the ray line through (x',y') , with thickness $t_{(x',y')}$ and absorber-to-detector-distance $L_{(x',y')}$, per unit of incoming beam fluence at point (x',y') , $f(r_{(x',y')})$, and EHP-column cross section $dx' dy'$. An example of an EHP is presented in Fig. 2-1. The derivation of $P(t)$, $s(r,t,L)$, $C(r,t)$, and $f(r)$ from measured input data is explained in Sec. III B.

2.3.2 Transmission prediction for wedged beams

The prediction of transmissions $T_{\text{wedge}}(x,y)$, using an EHP, is an extension to the procedure for open beams, which incorporates the effect of the wedge on the beam hardening and beam fluence. As for the open field, $T_{\text{wedge}}(x,y)$ consists of a primary component $T_{\text{wedge}}^P(x,y)$, and a scatter component, $T_{\text{wedge}}^S(x,y)$:

$$T_{\text{wedge}}(x,y) = T_{\text{wedge}}^P(x,y) + T_{\text{wedge}}^S(x,y). \quad 2-5$$

y direction ($<1\%$) are neglected; C_{wedge} in Eq. (2-6) does not explicitly depend on y .

The equation for calculation of the transmission due to scattered radiation, $T_{\text{wedge}}^S(x, y)$, is similar to that used for open beams [Eq. (2-4)]:

$$T_{\text{wedge}}^S(x, y) = \int_{(x', y') \in \text{field}} \frac{f_{\text{wedge}}(x', y')}{f_{\text{wedge}}(x, y)} \times s(r_{(x'-x, y'-y)}, t_{(x', y')}, L_{(x', y')}) dx' dy', \quad 2-7$$

with $f_{\text{wedge}}(x, y)$ the normalized incoming beam fluence profile for a wedged field. The scatter point spread functions $s(r, t, L)$ are derived from measured data in *open* beams. No separate scatter kernels are derived for wedged beams, since they do only weakly depend on the incident beam energy spectrum.²⁴ The derivation of $C_{\text{wedge}}(x, t)$ and $f_{\text{wedge}}(x, y)$ from measured input data is explained in Sec. III C.

2.4 Derivation of the functions used for transmission prediction from measured input data

The functions $P(t)$, $s(r, t, L)$, $C(r, t)$ and $f(r)$ (see Sec. II A), which are the input for the algorithm for open fields, are also used for transmission prediction in wedged beams. However, for wedged beams two extra functions are required, $C_{\text{wedge}}(x, t)$ and $f_{\text{wedge}}(x, y)$ (Sec. II B). In this section, we will summarize the derivation of the input functions from measured input data for the open beams and discuss in detail the derivation of the two extra functions for the wedged beams.

2.4.1 Experimental set-up for measurement of input data

Dose measurements were performed with a N31002 ionization chamber (PTW, Freiburg, Germany), positioned in a polystyrene mini phantom with a transversal cross section of $7 \times 7 \text{ cm}^2$ and a thickness of 3 cm.¹⁹ The short term reproducibility of the dose measurements was 0.2%. To minimize the effect of long term output fluctuations, the time between a measurement with and without absorber inserted was kept minimal. The top of the mini phantom was positioned at a distance of 160 cm from the focus, which is equal to the fixed focus-to-fluorescent screen distance of the

SRI-100 EPID. On top of this mini phantom, extra buildup could be added using 0.5 cm thick polystyrene slabs with the same cross section as the mini phantom. The depth of the ionization chamber in the mini phantom should be equal to the water equivalent depth of the fluorescent screen of the EPID. This effective depth is defined as the depth of the ionization chamber for which the variations in on-axis EPID response [(gray scale value measured with the EPID)/(portal dose measured with the ionization chamber)] for a set of flat, polystyrene absorbers with various thicknesses t and exit plane-to-detector distances L are minimal.¹¹ For the 6 MV beam the depth was 1 cm (mini phantom plus one slab) and for the 23 MV beam the depth was 2.5 cm (mini phantom plus four slabs). For off-axis measurements, the mini phantom with the ionization chamber inserted, was scanned in an empty RFA-300 water phantom (Scanditronix Medical AB, Uppsala, Sweden).

2.4.2 Derivation of $P(t)$, $s(r,t,L)$, $C(r,t)$, and $f(r)$: A summary

On-axis, a series of transmissions $T(w,t,L)$ through flat, polystyrene absorbers for clinically relevant combinations of field size $w \times w$, absorber thickness t , and absorber to detector distance L are measured.¹⁹ The set-up is depicted in Fig. 2-2. The contribution of scattered photons to the measured on-axis transmission reduces to zero for an infinitely small field. To estimate the on-axis primary component $P(t)$, for all t,L -combinations, the transmissions are extrapolated to zero field size, yielding extrapolated transmissions $T(w = 0, t, L)$. Next, for each thickness t , $T(w = 0, t, L)$ for all L are averaged, yielding the primary contribution $P(t)$. The primary contribution is independent of L since it stems from photons which have not interacted with the phantom.¹⁹

For each field $w \times w$, the total scatter contribution to the beam axis $S(w,t,L)$ is obtained by subtracting the transmission $T(w,t,L)$ and the primary component $P(t)$. For each t,L -combination, a corresponding scatter kernel $s(r,t,L)$ is then derived such that it obeys the following equation for each field $w \times w$:

$$S(w,t,L) = \int_{(x',y') \in w \times w} f(r_{(x',y')}) s(r_{(x',y')}, t, L) dx' dy', \quad 2-8$$

The integral on the right-hand side of this equation equals the expression of Eq. (2-4) for the on-axis scatter contribution $T^S(0,0)$ for a flat polystyrene absorber with a thickness t , positioned at a distance L from the PDI plane. $s(r,t,L)$ is the contribution to the on-axis scatter of an imaginary column at distance r from the beam axis with thickness t and absorber to detector distance L . $f(r)$ is a dose profile measured along the diagonal of a large open field without absorber inserted, which is normalized at the beam axis.

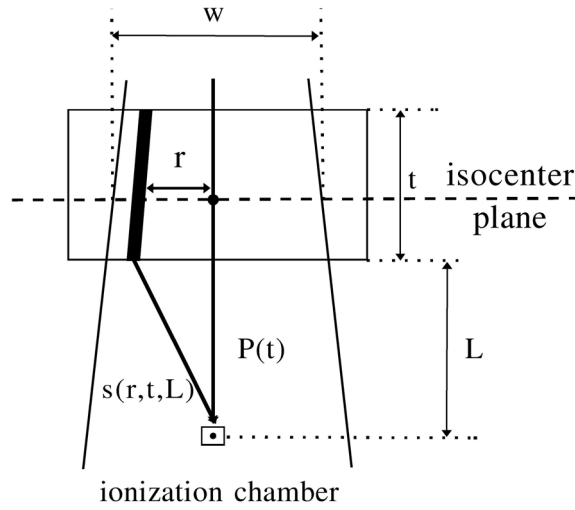


Figure 2-2 Set-up for measurement of beam data used to derive the required input functions for the algorithm for transmission prediction. The absorber is made out of polystyrene. The scatter kernel $s(r,t,L)$ and the primary contribution $P(t)$ are examples of derived input data.

The functions $C(r,t)$, used in Eq. (2-3), describe the off-axis change in penetrating quality of the beam. They are calculated using

$$C(r,t) = \frac{P(r,t)}{P(t)}, \quad 2-9$$

with $P(t)$ and $P(r,t)$ primary contributions to, respectively, on- and off-axis transmissions through flat, polystyrene phantoms of thicknesses t . Off-axis primary contributions $P(r,t)$, needed for calculation of $C(r,t)$, are determined using

$$P(r,t) = T(r, a \times b, t, L) - T^S(r, a \times b, t, L), \quad 2-10$$

with $T(r, a \times b, t, L)$ a measured off-axis transmission in a rectangular field $a \times b$ and $T^S(r, a \times b, t, L)$ the corresponding scatter contribution calculated with Eq. (2-4). As primary contributions do not depend on L , $C(r, t)$ functions are derived from transmissions measured for only one L .

2.4.3 Derivation of the functions $f_{\text{wedge}}(x, y)$ and $C_{\text{wedge}}(x, t)$

For each wedge, the normalized incoming beam fluence profile $f_{\text{wedge}}(x, y)$ is derived using

$$f_{\text{wedge}}(x, y) = \frac{D_{p, \text{wedge}}(x, y = 0)}{D_{p, \text{wedge}}(0, 0)} \frac{f(r_{(x, y)})}{f(r_{(x, y=0)})}, \quad 2-11$$

with $D_{p, \text{wedge}}(x, y = 0)$ a dose profile in the wedge direction (along the x axis), measured in the absence of absorbers and $f(r_{(x, y)})$ the normalized fluence profile measured in the largest open field along the diagonal. The penumbra's are replaced by a linear extrapolation of the remaining central part of the profile. An example of f_{wedge} for a 6 MV photon beam of a Siemens KD-2 accelerator with a 60° wedge inserted is presented in Fig. 2-3.

The function $C_{\text{wedge}}(x, t)$ is derived using Eq. (2-6) for $y = 0$:

$$C_{\text{wedge}}(x, t) = \frac{P_{\text{wedge}}(x, t)}{P(x, t)}, \quad 2-12$$

with $P_{\text{wedge}}(x, t)$ the primary component of the transmission measured beneath a flat absorber with thickness t in a wedged beam and $P(x, t)$ the primary component of the transmission for the same absorber in an open beam. $P(x, t)$ is the product of the on-axis primary transmission in the open beam, $P(t)$, with $C(x, t)$ as explained in Sec. III B. $P_{\text{wedge}}(x, t)$ is derived using

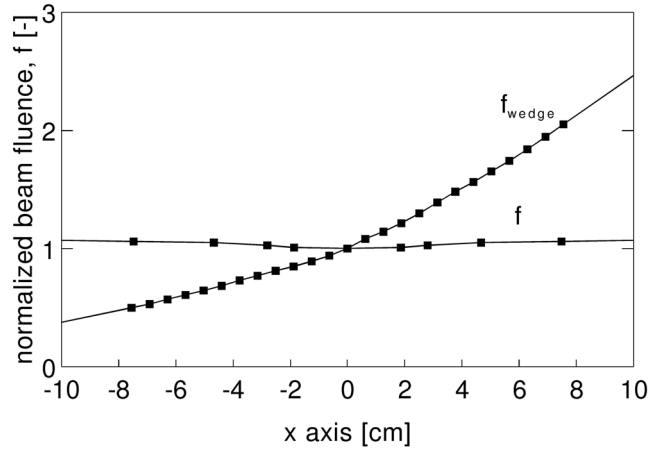


Figure 2-3 Normalized beam fluence f_{wedge} profile along the wedge direction for the 6 MV photon beam of a Siemens KD-2 accelerator with a 60° wedge inserted. The maximum field size with the 60° wedge inserted is $20 \times 30 \text{ cm}^2$. f is the fluence profile of the open beam.

$$P_{\text{wedge}}(x, t) = T_{\text{wedge}}(x, a \times b, t, L) - T_{\text{wedge}}^S(x, a \times b, t, L), \quad 2-13$$

with $T_{\text{wedge}}(x, a \times b, t, L)$ the measured transmission at position $(x, 0)$ in a wedged rectangular field $a \times b$ and $T_{\text{wedge}}^S(x, a \times b, t, L)$ the corresponding scatter contribution calculated with Eq. (2-7).

As for the open field, the derivation of C_{wedge} can be performed using one elongated rectangular field. However, we used three fields 20×8 , 20×14 , and $20 \times 20 \text{ cm}^2$. This was done to confirm the validity of Eq. (2-7) for calculation of T_{wedge}^S , using scatter point spread functions derived from the open field transmission measurements. For those fields, transmissions were measured for absorber thicknesses 10, 20, and 30 cm (and 5 cm for 6 MV) at positions $x = -8, -4, 0, 4$, and 8 cm using the set-up described in Sec. III A. The exit plane to detector distance of the absorbers, L , was 50 cm. In Tables 2-1 and 2-2 results are presented for the primary transmissions $P_{\text{wedge}}(x, t)$ in the 6 and 23 MV beams at position $x = -8, 0$, and 8 cm for three (four) polystyrene absorbers and

	t (cm)		
	10	20	30
23 MV			
$a \times b$ (cm ²)	$P_{\text{wedge}}(x=-8 \text{ cm}, t)$		
20×8	0.7555	0.5759	0.4424
20×14	0.7561	0.5753	0.4431
20×20	0.7550	0.5756	0.4440
mean	0.7555	0.5756	0.4432
σ	0.0004	0.0002	0.0007
$a \times b$ (cm ²)	$P_{\text{wedge}}(x=0 \text{ cm}, t)$		
20×8	0.7576	0.5770	0.4445
20×14	0.7593	0.5776	0.4452
20×20	0.7580	0.5766	0.4446
mean	0.7583	0.5771	0.4447
σ	0.0008	0.0004	0.0003
$a \times b$ (cm ²)	$P_{\text{wedge}}(x=8 \text{ cm}, t)$		
20×8	0.7397	0.5523	0.4182
20×14	0.7400	0.5530	0.4190
20×20	0.7408	0.5545	0.4205
mean	0.7401	0.5533	0.4193
σ	0.0005	0.0010	0.0010

Table 2-1 Primary transmissions $P_{\text{wedge}}(x, t)$ in a 23 MV beam with a 60° wedge inserted at positions $x = -8, 0$, and 8 cm for three polystyrene absorbers and three field sizes. The lower two rows in each block represent the mean of derived primary transmissions and the standard deviations therein.

three field sizes. The derived primary transmissions are effectively independent of the applied field size.

Derived functions $C_{\text{wedge}}(x, t)$ for the 6 MV and 23 MV photon beam of a Siemens KD-2 linear accelerator with a 60° wedge inserted are depicted in Fig. 2-4. For $t = 0$, $C_{\text{wedge}}(x, t)$ is by definition one. C_{wedge} increases towards the thick part of the wedge; the thicker the wedge the larger the penetrating quality of the beam. Note that the

	t (cm)			
	5	10	20	30
6 MV				
$a \times b$ (cm ²)	$P_{\text{wedge}}(x=-8 \text{ cm}, t)$			
20×8	0.8097	0.6638	0.4456	0.3056
20×14	0.8146	0.6643	0.4492	0.3097
20×20	0.8166	0.6677	0.4530	0.3144
mean	0.8136	0.6653	0.4493	0.3099
σ	0.0029	0.0017	0.0030	0.0036
$a \times b$ (cm ²)	$P_{\text{wedge}}(x=0 \text{ cm}, t)$			
20×8	0.8086	0.6529	0.4312	0.2902
20×14	0.7937	0.6550	0.4331	0.2919
20×20	0.8096	0.6538	0.4329	0.2917
mean	0.8040	0.6539	0.4324	0.2913
σ	0.0073	0.0009	0.0009	0.0007
$a \times b$ (cm ²)	$P_{\text{wedge}}(x=8 \text{ cm}, t)$			
20×8	0.7841	0.6174	0.3909	0.2544
20×14	0.7852	0.6193	0.3930	0.2565
20×20	0.7865	0.6212	0.3955	0.2585
mean	0.7853	0.6193	0.3931	0.2565
σ	0.0010	0.0016	0.0019	0.0017

Table 2-2 Primary transmissions $P_{\text{wedge}}(x, t)$ in a 6 MV beam with a 60° wedge inserted at positions $x = -8, 0$, and 8 cm for four polystyrene absorbers and three field sizes. The lower two rows in each block represent the mean of derived primary transmissions and the standard deviations therein.

penetrating quality of the beam, and thus the transmission below the thick part of the wedge is higher, whereas the beam fluence will be lower.

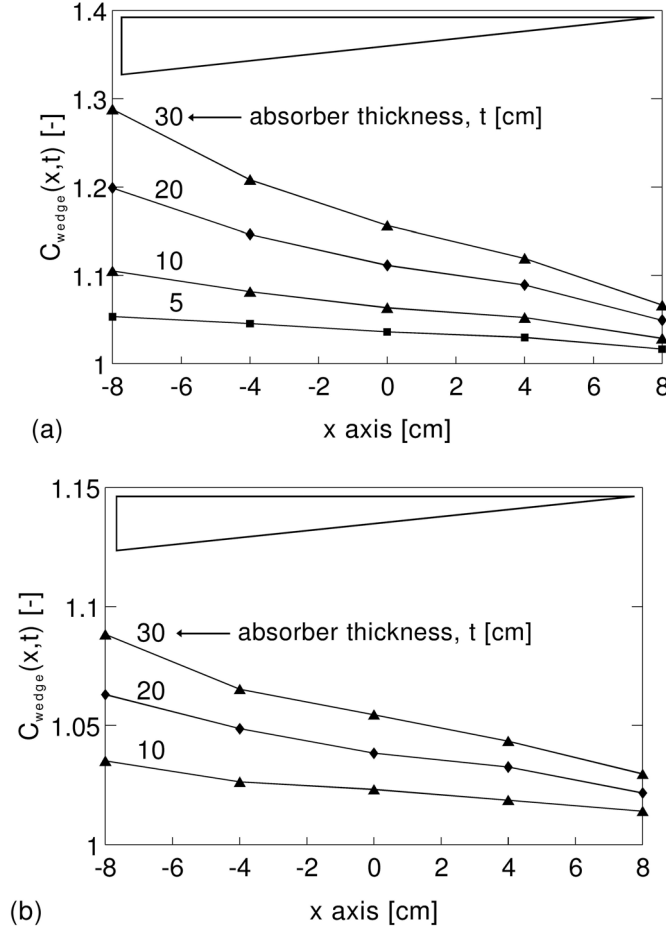


Figure 2-4 $C_{\text{wedge}}(x,t)$ for a 6 MV (a) and a 23 MV (b) photon beam of a Siemens KD-2 accelerator with a 60° wedge inserted.

2.5 Comparison of predicted and measured transmissions

The accuracy of the method to predict patient transmissions for wedged beams was assessed by comparing predictions with transmission measurements. The measurement set-up is described in Sec. III A. The ionization chamber was used as the gold standard for dose measurements. Predictions were performed at a 0.25 cm grid using Eq. (2-6) for the primary component and Eq. (2-7) for the scatter component. The calculation of the EHPs is described elsewhere¹⁹ and reviewed in Sec. II. Reported percent differences between predicted and measured transmissions are defined by $(\text{calculation} - \text{measurement}) / \text{measurement} \times 100$.

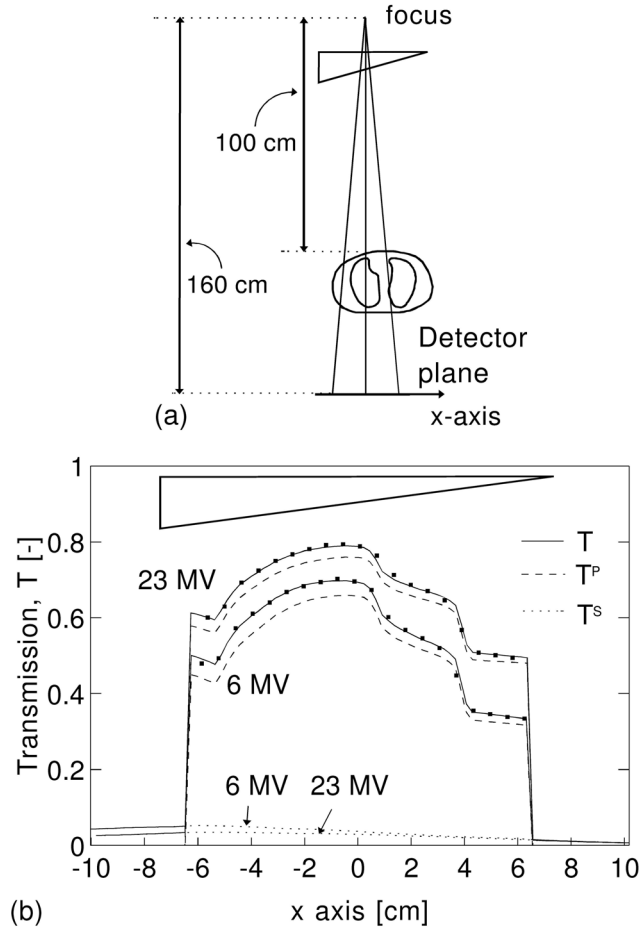


Figure 2-5 (a) Set-up with the thorax phantom. (b) Measured and predicted transmissions for this phantom irradiated with a rectangular $14 \times 12 \text{ cm}^2$ field using 6 and 23 MV photon beams with a 60° wedge inserted. The markers represent transmission measurements, the continuous lines the calculated transmissions. The dashed and dotted lines represent the calculated primary and scatter components, respectively.

The thorax phantom depicted in Fig. 2-5(a) was irradiated with a rectangular $14 \times 12 \text{ cm}^2$ field with the 6 and 23 MV photon beam. The phantom consists of lucite and cork and is symmetrical in the cranial–caudal direction. The SSD was 100 cm and the distance between the exit plane and the detector (L) 37.5 cm. The observed agreement for 19 points [excluding the point at the steep gradient ($x = 3.7 \text{ cm}$)] was $0.3 \pm 0.9\%$ for the 6 MV beam and $0.2 \pm 0.7\%$ for the 23 MV beam [Fig. 2-5(b)]. The dotted lines in

Fig. 2-5(b) show that T_{wedge}^s increases towards the thick end of the wedge, in contrast with the wedge fluence profile (Fig. 2-3). This behavior is due to the term $f_{wedge}(x,y)$ in the denominator of the integrand in Eq. (2-7), which causes T_{wedge}^s to rise with increasing wedge thickness. The presence of $f_{wedge}(x,y)$ in the denominator stems from the definition of T_{wedge}^s ; T_{wedge}^s is the ratio of the portal dose due to photons scattered from the patient towards the PDI plane and the (total) dose that would have been measured without the patient in the beam, the latter dose being proportional to $f_{wedge}(x,y)$.

We have also verified an off-axis profile below a flat polystyrene absorber. This was done to test the validity of the prediction of T_{wedge}^P with Eq. (2-6), in which a correction is applied for the combined effect on the beam hardening by the flattening filter and the wedge, and in which the divergence of the beam is partly neglected (Sec. II B).

Transmissions were measured along a profile parallel to the x axis at position $y = 4.5$ cm. Results are presented in Table 2-3. The difference between the predictions and measurements is $-0.2 \pm 0.4\%$. Table 2-3 shows that both T^P and T^s increase towards the thicker part of the wedge. The increase in T^s has been explained above. The increase in T^P is related to the C_{wedge} curves presented in Fig. 2-4, which demonstrates an increasing beam penetrating quality with increasing wedge thickness. This behavior is attributed to a more efficient filtering of the low energy x-ray photons for

x	y	T^P	T^s	T	$T_{measured}$	difference (%)
0	0	0.3956	0.0344	0.4300	0.429	0.2
-6	4.5	0.4033	0.0428	0.4461	0.445	0.2
-4	4.5	0.3976	0.0384	0.4360	0.439	-0.7
-2	4.5	0.3940	0.0342	0.4282	0.431	-0.6
0	4.5	0.3884	0.0297	0.4181	0.421	-0.7
2	4.5	0.3827	0.0242	0.4069	0.407	0.0
4	4.5	0.3751	0.0193	0.3944	0.395	-0.2
6	4.5	0.3637	0.0157	0.3793	0.380	-0.2
mean $\pm \sigma$:						$-0.2 \pm 0.4\%$

Table 2-3 Primary transmissions $P_{wedge}(x,t)$ in a 6 MV beam with a 60° wedge inserted at positions $x = -8, 0$, and 8 cm for four polystyrene absorbers and three field sizes. The lower two rows in each block represent the mean of derived primary transmissions and the standard deviations therein.

longer pathlengths through the wedge.

2.6 Discussion

In this paper, a method is described to accurately ($\sim 1\%$) calculate patient transmissions to be used for PDI predictions in wedged beams. These transmission functions will be used in our clinic for predicting PDIs, which are compared with PDIs measured with an EPID. Transmission functions for open fields have been used clinically for verification of irradiations of prostate cancer patients.^{13,14} The input for the algorithm is largely based on measured data that are already used for predictions in open fields. For each wedge, up to 75 additional dose measurements and one profile are required. Since for the measurements the position of the ionization chamber and the field size can be changed without entering the treatment room this can be done in 1.5 hours, excluding the time required to set-up the water phantom. On Siemens linacs traditionally four physical wedges (15° , 30° , 45° , and 60°) are used, which would thus require 6 hours of measurements. It was justified that the number of measurements can be reduced by a factor of 3 by using a single field, instead of three fields, for the derivation of $C_{wedge}(x,t)$ (see Sec. III C).

Dynamic or virtual wedges and IMRT fields, realized by a moving collimator jaw or moving leaves, do not alter the open beam photon spectrum. Therefore the off-axis transmission measurements to determine $C_{wedge}(x,t)$ can be skipped and $T^P(x,y)$ can be calculated with Eq. (2-4), like in open beams. We are investigating to also use Eq. (2-5) for calculation of $T^S(x,y)$ for IMRT fields produced with dynamic multileaf collimation (DMLC). For DMLC, $f(x,y)$ in Eq. (2-5) is different for all patient fields, yielding measurements like for open and wedged beams impractical. Preliminary results show however that we can use the fluence profile calculated by the treatment planning system.

So far we have not expanded the method to compensators. However, we have developed a method to verify compensator thicknesses using the measured transmission through the compensator, defined by the ratio of two EPID images, with and without compensator inserted.²⁵ Compensator thicknesses are derived from the primary component of the transmission. The technique is very similar to the one described in this paper.

2.7 Acknowledgments

This work was financially supported by the Dutch Cancer Society (Grant DDHK 98-1681) and by the 'Fundação para a Ciência e a Tecnologia'. The Netherlands Organization for Scientific Research (NWO) is acknowledged for a travel grant.

2.8 References

- ¹R. Boellaard, M. van Herk, H. Uiterwaal, and B. J. Mijnheer, "First clinical tests using a liquid-filled electronic portal imaging device and a convolution model for the verification of the midplane dose," *Radiother. Oncol.* **47**, 303–312 (1998).
- ²V. N. Hansen, P. M. Evans, and W. Swindell, "The application of transit dosimetry to precision radiotherapy," *Med. Phys.* **23**, 713–721 (1996).
- ³H. Keller, M. Fix, and P. Ruegsegger, "Calibration of a portal imaging device for high-precision dosimetry: A Monte Carlo study," *Med. Phys.* **25**, 1891–1902 (1998).
- ⁴T. R. McNutt, T. R. Mackie, P. Reckwerdt, N. Papanikolaou, and B. R. Paliwal, "Calculation of portal dose using the convolution/superposition method," *Med. Phys.* **23**, 527–535 (1996).
- ⁵J. W. Wong, E. D. Slessinger, R. E. Hermes, C. J. Offutt, T. Roy, and M. W. Vannier, "Portal dose images 1: Quantitative treatment plan verification," *Int. J. Radiat. Oncol., Biol., Phys.* **18**, 1455–1463 (1990).
- ⁶A. G. Glendinning and D. E. Bonnett, "Dosimetric properties of the Theraview fluoroscopic electronic portal imaging device," *Br. J. Radiol.* **73**, 517–530 (2000).
- ⁷H. Parsaei, E. el Khatib, and R. Rajapakshe, "The use of an electronic portal imaging system to measure portal dose and portal dose profiles," *Med. Phys.* **25**, 1903–1909 (1998).
- ⁸M. C. Kirby and P. C. Williams, "The use of an electronic portal imaging device for exit dosimetry and quality control measurements," *Int. J. Radiat. Oncol., Biol., Phys.* **31**, 593–603 (1995).
- ⁹Y. Zhu, X.-Q. Jiang, and J. van Dyk, "Portal dosimetry using a liquid ion chamber matrix: Dose response studies," *Med. Phys.* **22**, 1101–1106 (1995).
- ¹⁰A. van Esch, B. Vanstraelen, J. Verstraete, G. Kutcher, and D. Huyskens, "Pre-treatment dosimetric verification by means of a liquid-filled electronic portal imaging device during dynamic delivery of intensity modulated treatment fields," *Radiother. Oncol.* **60**, 181–190 (2001).
- ¹¹K. L. Pasma, M. Kroonwijk, J. C. J. de Boer, A. G. Visser, and B. J. M. Heijmen, "Accurate portal dose measurement with a fluoroscopic electronic portal imaging device (EPID) for open and wedged beams and for dynamic multileaf collimation," *Phys. Med. Biol.* **43**, 2047–2060 (1998).
- ¹²B. J. M. Heijmen, K. L. Pasma, M. Kroonwijk, V. G. M. Althof, J. C. J. de Boer, A. G. Visser, and H. Huizenga, "Portal dose measurement in radiotherapy using an electronic portal imaging device (EPID)," *Phys. Med. Biol.* **40**, 1943–1955 (1995).
- ¹³K. L. Pasma, M. Kroonwijk, S. Quint, A. G. Visser, and B. J. M. Heijmen, "Transit dosimetry with an electronic portal imaging device (EPID) for 115 prostate cancer patients," *Int. J. Radiat. Oncol., Biol., Phys.* **45**, 1297–1303 (1999).

-
- ¹⁴M. Kroonwijk, K. L. Pasma, S. Quint, P. C. M. Koper, A. G. Visser, and B. J. M. Heijmen, "In vivo dosimetry for prostate cancer patients using an electronic portal imaging device (EPID); detection of internal organ motion," *Radiother. Oncol.* **49**, 125–132 (1998).
- ¹⁵J. C. Stroom, M. Kroonwijk, K. L. Pasma, P. C. M. Koper, E. B. von Dieren, and B. J. M. Heijmen, "Detection of internal organ movement in prostate cancer patients using portal images," *Med. Phys.* **27**, 452–461 (2000).
- ¹⁶J. C. J. de Boer, B. J. M. Heijmen, K. L. Pasma, and A. G. Visser, "Characterization of a high elbow, fluoroscopic electronic portal imaging device for portal dosimetry," *Phys. Med. Biol.* **45**, 197–216 (2000).
- ¹⁷K. L. Pasma, M. L. P. Dirkx, M. Kroonwijk, A. G. Visser, and B. J. M. Heijmen, "Dosimetric verification of intensity modulated beams produced with dynamic multileaf collimation using an electronic portal imaging device," *Med. Phys.* **26**, 2373–2378 (1999).
- ¹⁸B. J. M. Heijmen, P. R. M. Storchi, and J. B. van de Kamer, "A method for prediction of portal dose images," in *Proceedings of the XIth ICCR (International Congress on the use of Computers in Radiation Therapy, Manchester, UK, 20-24 March, 1994)*, edited by A. R. Hounsell, J. M. Wilkinson, and P. C. Williams (Handley, Stockport, UK, 1994), pp. 112–113.
- ¹⁹K. L. Pasma, B. J. M. Heijmen, M. Kroonwijk, and A. G. Visser, "Portal dose image (PDI) prediction for dosimetric treatment verification in radiotherapy I. An algorithm for open beams," *Med. Phys.* **25**, 830–840 (1998).
- ²⁰L. Spies and T. Bortfeld, "Analytical scatter kernels for portal imaging at 6 MV," *Med. Phys.* **28**, 553–559 (2001).
- ²¹B. M. C. McCurdy and S. Pistorius, "A two-step algorithm for predicting portal dose images in arbitrary detectors," *Med. Phys.* **27**, 2109–2116 (2000).
- ²²P. Storchi and E. Woudstra, "Calculation of the absorbed dose distribution due to irregularly shaped photon beams using pencil beam kernels derived from basic input data," *Phys. Med. Biol.* **41**, 637–656 (1996).
- ²³B. M. C. McCurdy and S. Pistorius, "Photon scatter in portal images: accuracy of a fluence based pencil beam superposition algorithm," *Med. Phys.* **27**, 913–922 (2000).
- ²⁴B. M. C. McCurdy and S. Pistorius, "Photon scatter in portal images: Physical characteristics of pencil beam kernels generated using EGS Monte Carlo code," *Med. Phys.* **27**, 312–320 (2000).
- ²⁵K. L. Pasma, M. Kroonwijk, E. B. van Dieren, A. G. Visser, and B. J. M. Heijmen, "Verification of compensator thicknesses using a fluoroscopic electronic portal imaging device," *Med. Phys.* **26**, 1524–1529 (1999).

CHAPTER 3. DOSIMETRIC VERIFICATION OF X-RAY FIELDS WITH STEEP DOSE GRADIENTS USING AN ELECTRONIC PORTAL IMAGING DEVICE

S C Vieira, M L P Dirkx, K L Pasma, B J M Heijmen

Phys. Med. Biol. **48**, 157-166, 2003

3.1 Abstract

Regions with steep dose gradients are often encountered in clinical x-ray beams, especially with the growing use of intensity modulated radiotherapy (IMRT). Such regions are present both at field edges and, for IMRT, in the vicinity of the projection of sensitive anatomical structures in the treatment field. Dose measurements in these regions are often difficult and labour intensive, while dose prediction may be inaccurate. A dedicated algorithm developed in our institution for conversion of pixel values, measured with a charged coupled device camera based fluoroscopic electronic portal imaging device (EPID), into absolute absorbed doses at the EPID plane has an accuracy of 1-2% for flat and smoothly modulated fields. However, in the current algorithm there is no mechanism to correct for the (short-range) differences in lateral electron transport between water and the metal plate with the fluorescent layer in the EPID. Moreover, lateral optical photon transport in the fluorescent layer is not taken into account. This results in large deviations ($>10\%$) in the penumbra region of these fields. We have investigated the differences between dose profiles measured in water and with the EPID for small heavily peaked fields. A convolution kernel has been developed to empirically describe these differences. After applying the derived kernel to raw EPID images, a general agreement within 2% was obtained with the water measurements in the central region of the fields, and within 0.03 cm in the penumbra region. These results indicate that the EPID is well suited for accurate dosimetric verification of steep gradient X-ray fields.

3.2 Introduction

In clinical practice and for intensity modulated radiotherapy (IMRT) in particular, steep dose gradient regions are often encountered, especially at field edges and near the projection of sensitive anatomical structures in the treatment field.^{1,3} The verification of these steep gradient regions is important but complicated and labour intensive, being performed with film and/or in water with a small detector. On the other hand, treatment planning systems may fail to accurately predict dose in these regions.³

In our institution, the use of charged coupled device (CCD) camera based fluoroscopic electronic portal imaging devices (EPIDs) for dosimetical measurements has been investigated in detail, e.g. for pre-treatment verification of IMRT fields produced with dynamic multileaf collimation (DMLC)⁹ and for in-vivo dosimetry.^{2,4,5,8,10} A dedicated algorithm has been developed which converts measured pixel values into absolute absorbed doses at the EPID plane with an accuracy of 1-2% when compared with water measurements. This accuracy is achieved outside the penumbra regions of flat and wedged fields and for smoothly modulated IMRT fields.⁹ However, large deviations ($> 10\%$) do occur in the penumbra regions. The main reason is that the current algorithm does not adequately take into account the differences in lateral electron transport between water and the metal plate with fluorescent layer in the EPID. Moreover, lateral optical photon transport in the fluorescent layer is not accounted for.

In the current paper, we have performed dosimetical studies to assess the impact of the aforementioned differences between water and the EPID on measured profiles for small, heavily peaked square and rectangular fields (width 0.4 cm - 4 cm). A short-range kernel has been derived for convolution with raw EPID images to improve the agreement between EPID measurements and water dose measurements.

3.3 Materials and methods

3.3.1 The EPID

The applied fluoroscopic Theraview NT EPID (Cablion Medical, Leusden, The Netherlands), low elbow type, is equipped with a fluorescent screen, a mirror, and a CCD camera (Adimec MX12). The fluorescent screen contains a layer of 150 mg cm^{-2} gadolinium oxysulphide coated onto a 2 mm thick brass build-up plate.² An additional build up layer of 1 mm stainless steel is used for dosimetric purposes.⁸ X-ray photons

are absorbed by the build up layers and the fluorescent screen generating optical photons, which are reflected by the 45° tilted mirror and detected by the CCD camera. The CCD camera is connected to a PC containing a frame grabber. The analogue video signal of the camera is digitised by the frame grabber, yielding frames with 512×512 pixels with a pixel range of 0-1023 ADC units. Individual camera frames are acquired with a given integration time, which can vary from 40 ms to 1280 ms, and summed. The summed image, divided by the total number of individual frames, is corrected for the dark current, acquired prior to irradiation. This approach minimises the contribution of the camera read-out noise on the final image. Image acquisition is performed using the EPID software running on a Windows application. The EPID system has an excellent short and long-term sensitivity stability.²

3.3.2 Measurements

All measurements were performed on the MM50 Racetrack Microtron (Scanditronix Medical AB, Uppsala, Sweden) with a 25 MV photon beam running at 300 monitor units per minute. The MM50 is equipped with a multileaf collimator, consisting of 64 leaves with a width of 1.25 cm projected at isocentre level. The width of the fields used was set by the multileaf collimator, and the length by the collimator blocks.

The EPID was placed at a fixed focus-to-fluorescent screen distance of 150 cm, yielding a pixel size of $0.059 \times 0.059 \text{ cm}^2$ at the isocentre plane. Image acquisition was performed with an integration time of 1280 ms and a camera gain set to 1.

Water measurements were done using a linear diode array (LDA) (Scanditronix Medical AB, Uppsala, Sweden) at a depth of 3 cm. For this depth, it was experimentally found that the deviations in the on-axis response of the EPID (as compared with an ionisation chamber) were minimal for field sizes ranging from $3 \times 3 \text{ cm}^2$ to $18 \times 18 \text{ cm}^2$.⁸ The LDA contains 11 p-type diodes with a spacing of 2.5 cm. Each LDA diode has a sensitive diameter of 0.25 cm and a sensitive volume thickness of $6 \times 10^{-3} \text{ cm}$. Generally, the LDA was scanned with a resolution of 0.1 cm at the EPID plane, except for the fields with a width equal to or less than 1 cm, where a resolution of 0.05 cm was used.

Measurements were also performed using film (Kodak XV) in order to offer an extra comparison with EPID data. These measurements were done in polystyrene at the same depth as used for the water measurements (3 cm). The films were digitised using a Lumiscan100 (Lumisys Inc., Sunnyvale, USA) with a spot size of 0.04 cm. To be

able to convert the film readings to dose values, a sensitometric curve was measured using the same set up. The source to detector distance for the water and the film measurements was the same as for the EPID measurements (150 cm).

In this paper, the x and y position coordinates are defined in the direction of leaf motion, and perpendicular to this, respectively. All coordinates are presented in the isocentre plane.

3.3.2.1 Small square and rectangular static fields

First, the reproducibility of small field measurements was investigated. For a field of $0.4 \times 5 \text{ cm}^2$, EPID images were acquired four times. In between these measurements, the field size was changed to $10 \times 10 \text{ cm}^2$. In this way, the reproducibility of leaf positioning could be assessed.

Subsequently, measurements were performed to investigate the existing differences between EPID and water dose measurements for highly peaked fields. Both square

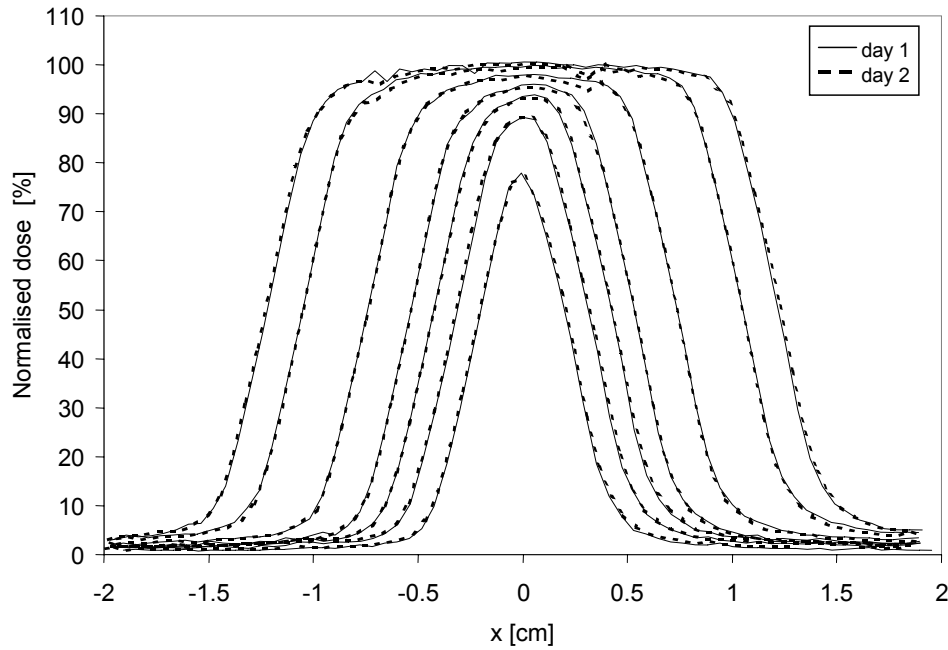


Figure 3-1 EPID measurements for small rectangular fields on two days separated by a month. The widths of the fields are 0.4, 0.6, 0.8, 1.0, 1.4, 2.0 and 2.4 cm, respectively. The length of all fields is 5 cm. All profiles are normalised to the on-axis pixel value for the $2.4 \times 5 \text{ cm}^2$ field.

and rectangular fields were investigated. The square fields ranged from $1 \times 1 \text{ cm}^2$ to $4 \times 4 \text{ cm}^2$. The rectangular fields had a fixed length of 5 cm and a width varying from 0.4 cm to 2.4 cm. All measured profiles were normalised to the on-axis value of the $2.4 \times 5 \text{ cm}^2$ field. For the EPID profiles, this on-axis value was derived by averaging 5 pixels in the y direction to minimise the effect of pixel noise. The $2.4 \times 5 \text{ cm}^2$ field is small enough to avoid optical cross talk effects in the EPID-profile^{4,8} and large enough to avoid the on-axis dose reading being affected by the short-range scatter effects investigated in this paper. The measurements were performed twice with an interval of one month, thereby investigating the reproducibility in time.

3.3.2.2 Rectangular fields separated by a narrow gap

In IMRT, steep dose gradients may occur near the projection of sensitive anatomical structures. To simulate the sparing of a small structure, dose measurements were performed using two static fields of $3 \times 4 \text{ cm}^2$ separated by a gap of 0.6 cm, 0.8 cm, 1 cm, or 2 cm, respectively. For each of these distances, the two $3 \times 4 \text{ cm}^2$ fields were

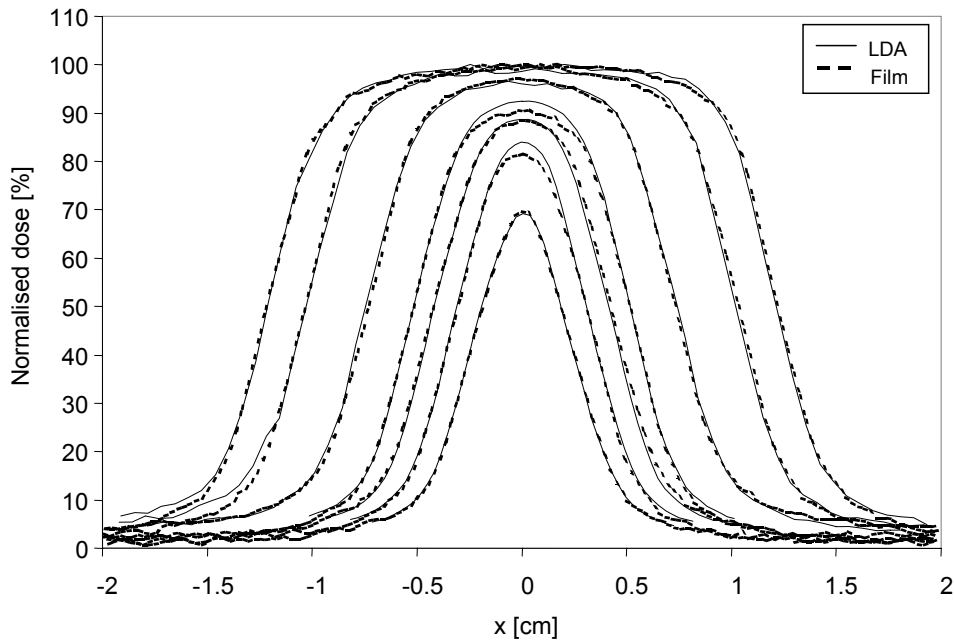


Figure 3-2 Comparison of film and LDA measurements. The width of the fields is 0.4, 0.6, 0.8, 1.0, 1.4, 2.0 and 2.4 cm, respectively. The length of all fields is 5 cm. All profiles are normalised to the on-axis dose measured for the $2.4 \times 5 \text{ cm}^2$ field.

measured separately, and then summed. One field was kept in a fixed position for all gaps, while the other field changed position, thereby changing the gap between the fields. Measurements were performed with the EPID and with the LDA. Both the summed water and EPID measurements were divided by a static reference field of $14 \times 4 \text{ cm}^2$. In this way, the (small) optical cross talk in the EPID images was removed and small imperfections in the fluorescent screen were corrected for.⁸ The dimension of the static reference field in the x direction was chosen as such to encompass the two measured off-axis fields. In the y direction, the reference field has the same size as the off-axis fields, and therefore a similar cross talk.

3.3.3 Kernel derivation

After assessing the differences between the water and EPID measurements in the small, highly peaked fields (section 3.3.2.1), a short-range convolution kernel was derived for correction of measured EPID images. The kernel was assumed to be

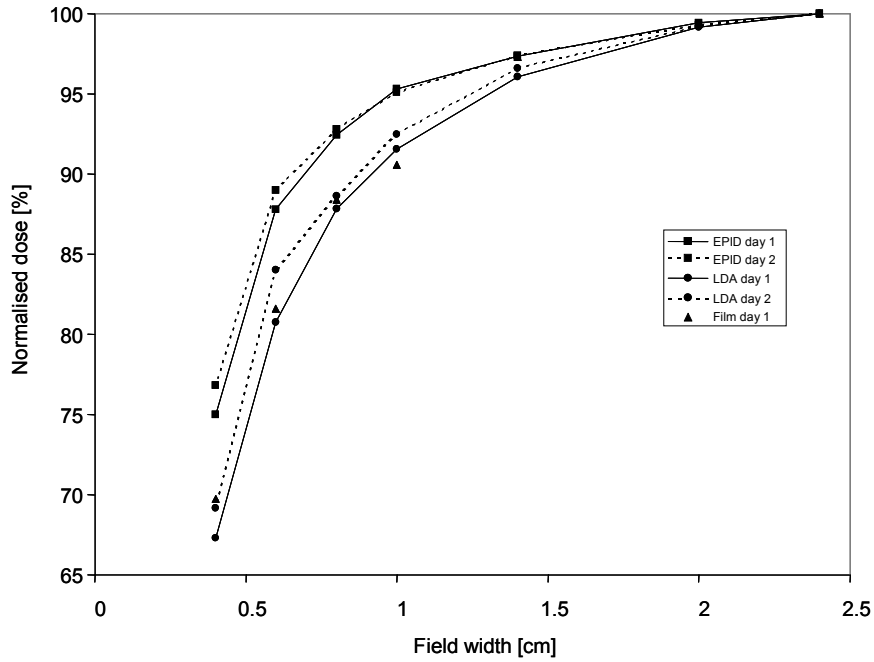


Figure 3-3 On-axis doses measured with EPID, film, and LDA for fields of $0.4 \times 5 \text{ cm}^2$ to $2.4 \times 5 \text{ cm}^2$. All profiles are normalised to the on-axis dose measured for the $2.4 \times 5 \text{ cm}^2$ field.

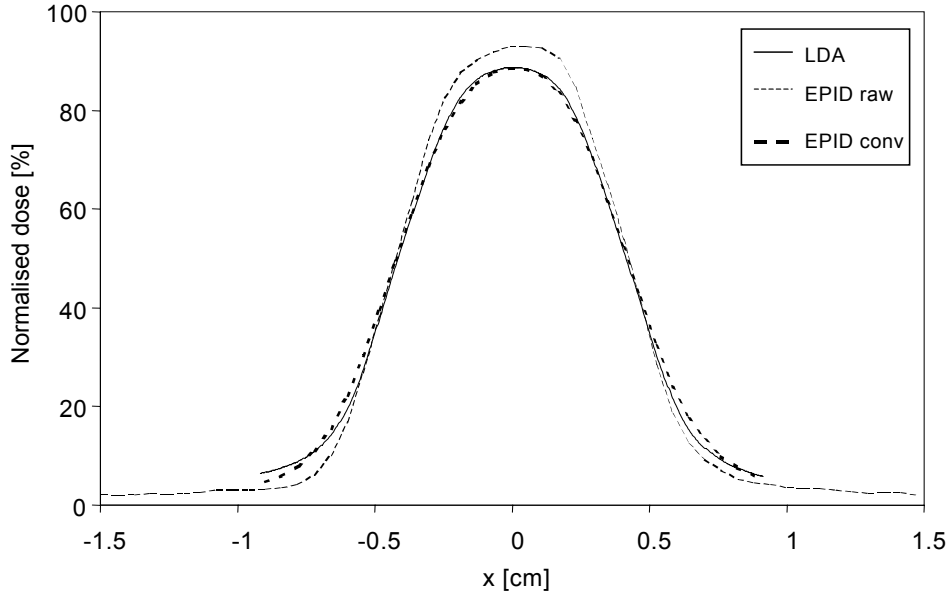


Figure 3-4 Dose profiles measured in water (LDA), measured with the EPID (EPID raw), and obtained after convolution of the raw EPID data with the derived kernel (EPID conv), for a 0.8×5 cm² field. All profiles are normalised to the on-axis dose measured for the 2.4×5 cm² field.

circular symmetric and has a resolution equal to the pixel size of the EPID (0.059 cm). The kernel values, k_i , located at distances $r_i = i \times \text{pixel size of the EPID}$ were determined with an exhaustive search algorithm. For all investigated sets $\{k_i\}$, the kernel values were first divided by their total sum for normalisation. A selected EPID image was then convolved with the kernel and compared with the corresponding water dose measurements using the method of Low *et al.*⁶ First, for each point m of the EPID profile, a quality index γ_m was produced to summarise the distance and dose difference with neighbouring points in the water dose distribution, using tolerance values of 3 mm and 3%, respectively. The selected kernel $\{k_i\}$ had the lowest γ , which is the sum of all γ_m . The kernel was derived using measured data for a 0.8×5 cm² field. A software routine written in the Interactive Data Language 5.3 (Research Systems, Boulder, CO) was applied.

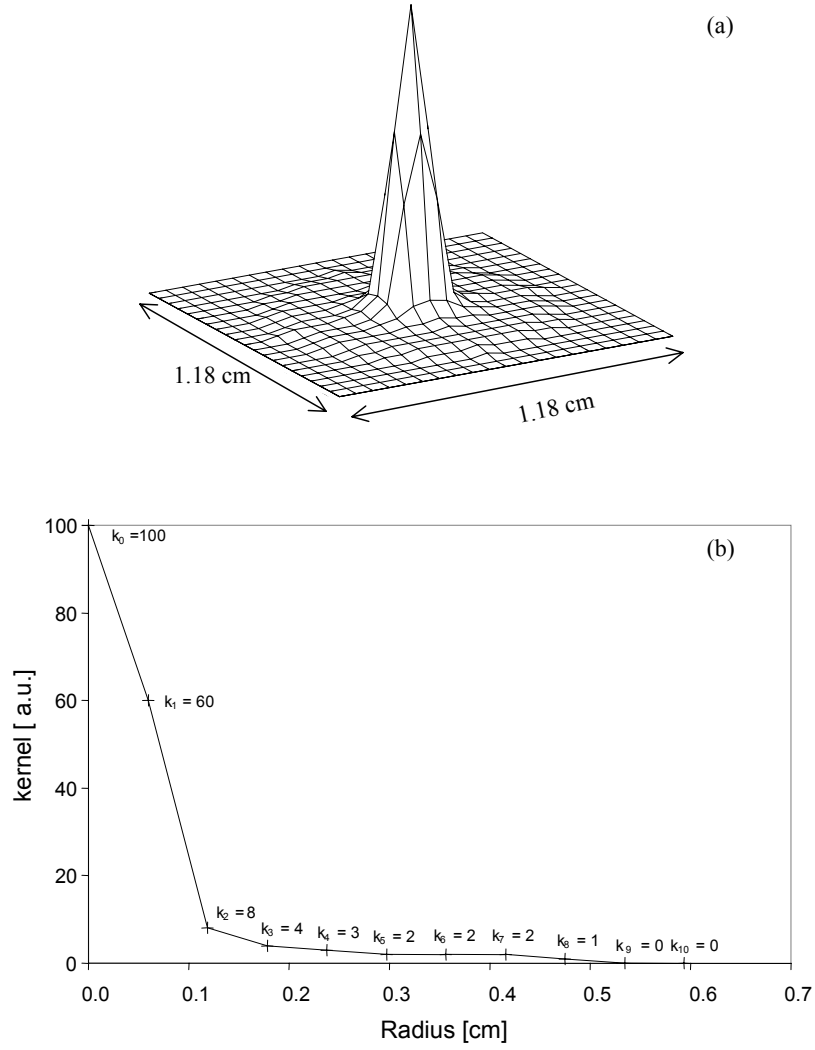


Figure 3-5 The derived circular symmetric kernel normalised to 100 at the center. (a) 3D view, (b) profile of the kernel as a function of the radius.

3.4 Results and discussion

3.4.1 Reproducibility of the measurements

The short-term reproducibility of the acquired EPID images for a $0.4 \times 5 \text{ cm}^2$ field, which were set up by alternating with a field of $10 \times 10 \text{ cm}^2$, was within 1%. This

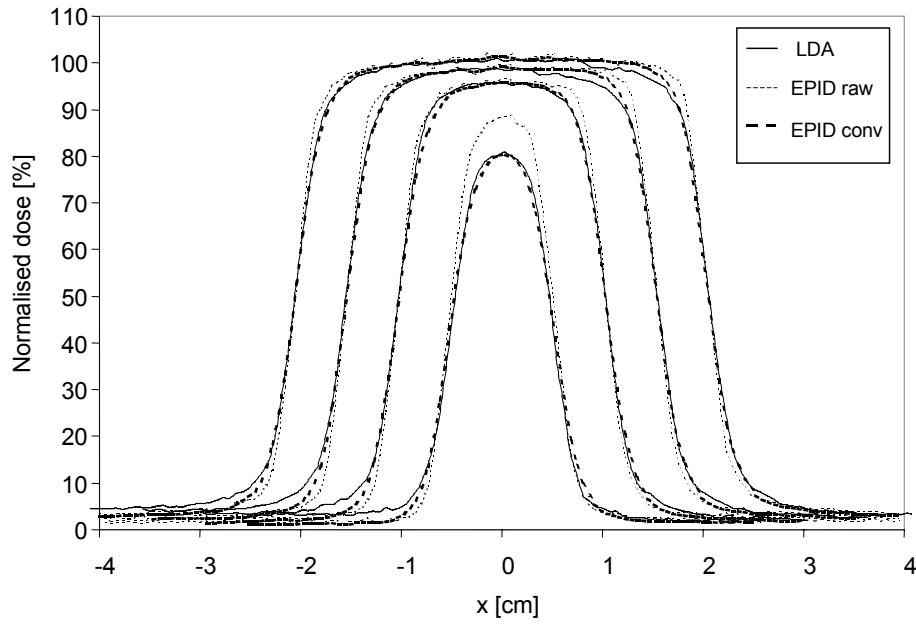


Figure 3-6 Dose profiles measured in water (LDA), with the EPID (EPID raw), and obtained after convolution of the raw EPID data with the derived kernel (EPID conv), for square fields of $1 \times 1 \text{ cm}^2$, $2 \times 2 \text{ cm}^2$, $3 \times 3 \text{ cm}^2$, and $4 \times 4 \text{ cm}^2$. All profiles are normalised to the on-axis dose measured for the $2.4 \times 5 \text{ cm}^2$ field.

shows that repositioning of the leaves is very accurate for the MM50 Racetrack Microtron.

Figure 3-1 shows the long-term reproducibility of the measurements. The agreement between both profiles is better than 1% or within 0.01 cm in the penumbra region. Therefore, both the EPID system and the linear accelerator show a good reproducibility over the one-month period. In figure 3-2, a comparison is made between film and LDA measurements. LDA and film generally agree within less than 2% in the central regions and within 0.02 cm in the penumbra region. Given this overall agreement between film and LDA profiles, the LDA was selected as the reference against which the EPID is validated in this study.

3.4.2 Kernel derivation

In figure 3-3, an overview of the on-axis dose values measured with film, LDA and EPID are shown. It is clear that, with the EPID, systematically higher peak values were measured than with film and LDA. These differences become larger with decreasing field size. Figure 3-4 clearly demonstrates that the higher peak values for the EPID are accompanied by a steeper beam penumbra. Based on the data presented in figure 3-4, the kernel shown in figure 3-5 was derived. After convolving the raw EPID data with the kernel, a very good agreement between water measurements and EPID measurements is obtained, both in the peak value and in the penumbra (see figure 3-4).

3.4.3 Small square and rectangular fields

Figure 3-6 shows the effect of the convolution with the kernel on profiles measured for square fields of $1 \times 1 \text{ cm}^2$, $2 \times 2 \text{ cm}^2$, $3 \times 3 \text{ cm}^2$ and $4 \times 4 \text{ cm}^2$. Clearly the kernel has the largest impact for the $1 \times 1 \text{ cm}^2$ field. Differences between LDA and EPID raw data are reduced from 8% to less than 2% in the central part of this field, after the kernel is applied. For the larger fields, significant improvements are obtained as well, especially in the penumbra regions. Figures 3-7a and 3-7b show similar data for the rectangular fields. As for the square fields, convolution with the kernel results in a significant reduction in the differences between LDA data and EPID profiles for all fields. After the kernel is applied, an overall agreement within 2% is obtained in the central parts, except for the fields with a width of 0.4 and 0.6 cm (4% and 3%, respectively). However, for these two fields, the largest reduction in dose difference is achieved due to the convolution. After convolution, the differences in the penumbra region are less than 0.03 cm for all profiles.

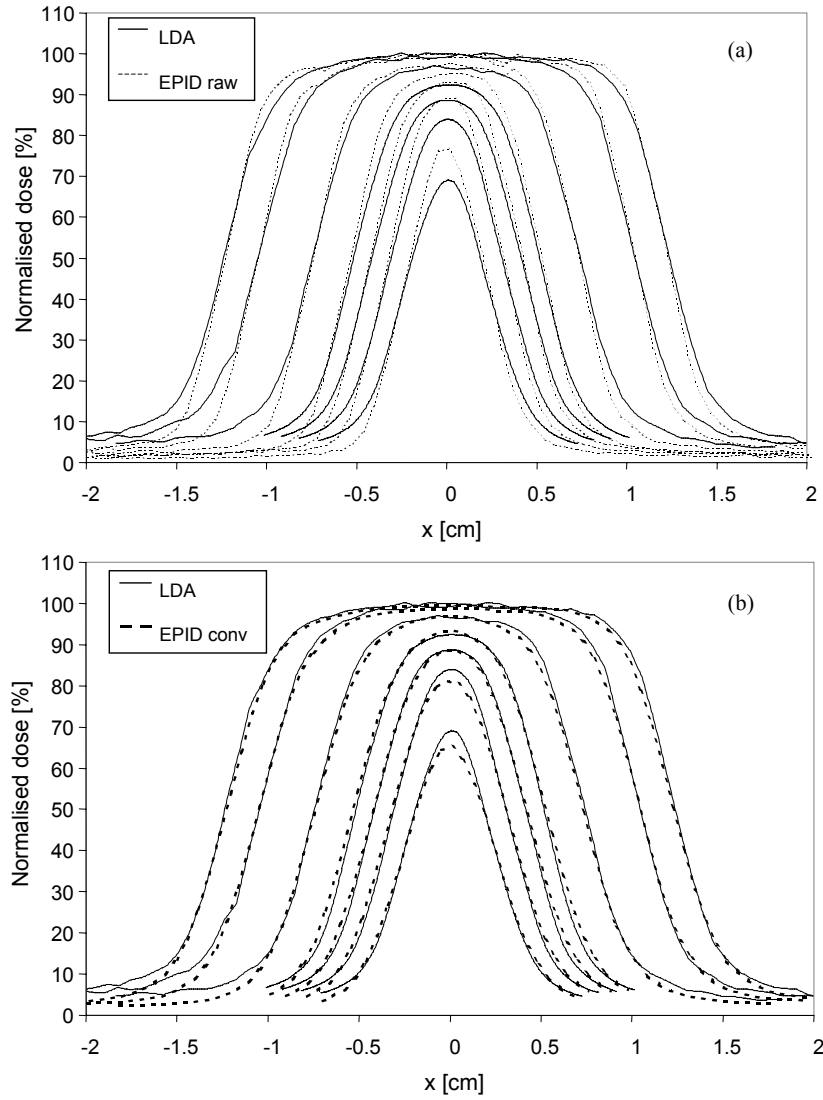


Figure 3-7 Comparison of dose profiles for rectangular fields (a) measured in water and with the EPID, and (b) measured in water and after convolution of the raw EPID data with the obtained kernel. The widths of the fields are 0.4, 0.6, 0.8, 1.0, 1.4, 2.0 and 2.4 cm, and the length of all fields is 5 cm. All profiles are normalised to the on-axis dose measured for the $2.4 \times 5 \text{ cm}^2$ field.

3.4.4 Rectangular fields separated by a narrow gap

The measurements performed with varying gaps between two static fields are presented in figure 3-8. After applying the kernel, a difference of less than 2% between the LDA measurements and the EPID profiles was found for all cases studied, except for the smallest gap. For this case, a difference of about 4% occurs in the region between the two fields. Nevertheless, one should bear in mind that the result obtained for the 0.6 cm gap still shows a huge improvement (about 12%) with respect to the raw EPID data. Overall, the best agreement is obtained for the distance of 0.8 cm, which is understandable given the fact that the kernel was derived using data from this field.

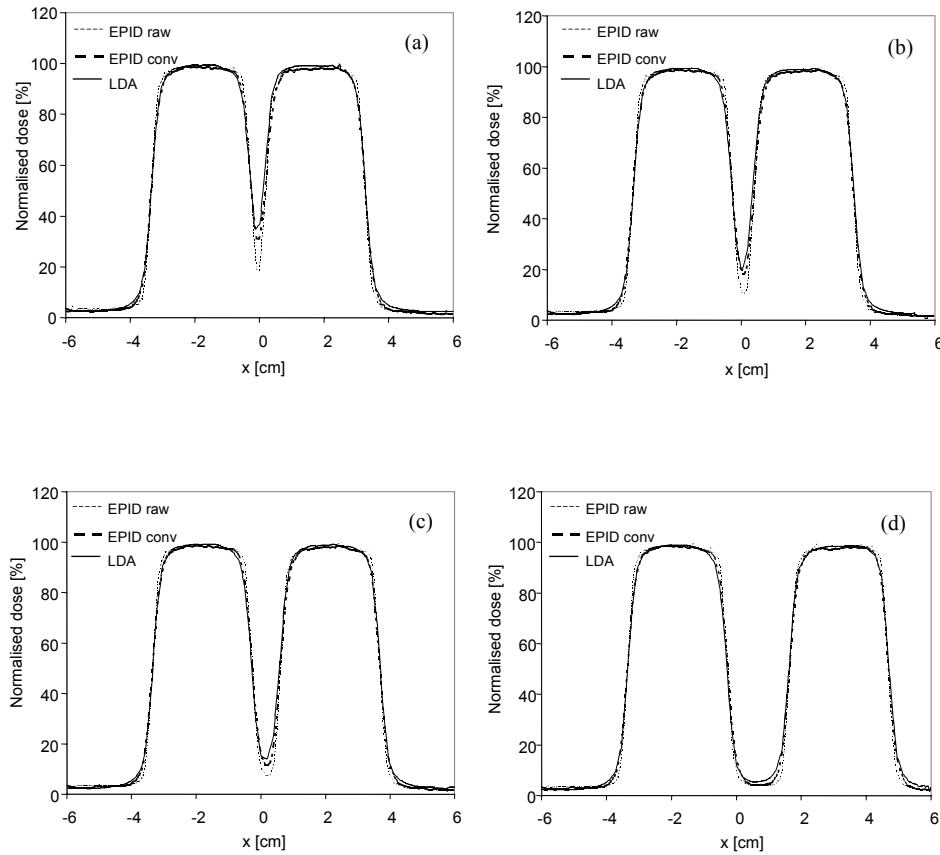


Figure 3-8 Measured dose profile for two static fields of $3 \times 4 \text{ cm}^2$ separated by a gap of (a) 0.6 cm, (b) 0.8 cm, (c) 1.0 cm, and (d) 2.0 cm. All profiles are normalised to the on-axis dose measured for a $14 \times 4 \text{ cm}^2$ field.

3.5 Conclusions

Large differences occur between water and raw EPID dose measurements. The smaller the field, and the smaller the distance between adjacent fields, the larger the differences encountered between raw EPID data and water or film measurements. A kernel was derived which corrects for the short-range differences. After convolving the raw EPID images with the kernel, an overall agreement within 2%, or 0.03 cm in the penumbra region, was obtained between the water measurements and the corrected EPID images. Keeping in mind the overall accuracy in absolute dose delivered to the patient of $\pm 3.5\%$ (1SD), which is aimed at clinical practice,⁷ the observed maximum dose differences are clinically acceptable. This is also true for the narrow fields (0.4 cm and 0.6 cm wide), for which deviations up to 4 % were observed, because in IMRT these fields are generally used in combination with wider fields resulting in better overall accuracy. For small fields (with widths equal to or less than 1 cm), the kernel improves the EPID profile both in the central part of the field and in the penumbra region. For larger fields, improvements are seen in the penumbra region, where before significant differences between water and EPID measurements existed.

The next step is to integrate the derived kernel in our existing algorithm, which converts pixel values into absorbed dose at the EPID plane. By applying this kernel to the raw EPID images, we should be able to accurately perform 2D dosimetric verification of highly modulated dose profiles, which may occur in IMRT. As a-Si flat panel imagers also contain a metal plate with a fluorescent layer for conversion of X-rays into visible photons, it is believed that the results in this paper will also be relevant for these EPIDs.

3.6 Acknowledgments

The authors would like to thank Gijs van Schelven for his participation in the measurements and his contribution to the analysis of the measured data. This work was supported by the 'Fundação para a Ciência e a Tecnologia' and by the Dutch Cancer Society (grant DDHK 98-1681).

3.7 References

- ¹C. Burman, C. S. Chui, G. Kutcher, S. Leibel, M. Zelefsky, T. LoSasso, S. Spirou, Q. Wu, J. Yang, J. Stein, R. Mohan, Z. Fuks, and C. C. Ling, "Planning, Delivery, and quality assurance of intensity modulated radiotherapy using dynamic multileaf collimator: a strategy for large-scale implementation for the treatment of carcinoma of the prostate," *Int. J. Radiat. Oncol. Biol. Phys.* **39**, 863-73 (1997).
- ²J. C. J. de Boer, B. J. M. Heijmen, K. L. Pasma, and A. G. Visser, "Characterization of a high elbow, fluoroscopic electronic portal imaging device for portal dosimetry," *Phys. Med. Biol.* **45**, 197-16 (2000).
- ³M. Essers, M. de Langen, M. L. P. Dirkx, and B. J. M. Heijmen, "Commissioning of a commercially available system for intensity-modulated radiotherapy dose delivery with dynamic multileaf collimation," *Radiother. Oncol.* **60**, 215-24 (2001).
- ⁴B. J. M. Heijmen, K. L. Pasma, M. Kroonwijk, V. G. M. Althof, J. C. J. de Boer, A. G. Visser, and H. Huizenga, "Portal dose measurement in radiotherapy using an electronic portal imaging device (EPID)," *Phys. Med. Biol.* **40**, 1943-55 (1995).
- ⁵M. Kroonwijk, K. L. Pasma, S. Quint, P. C. M. Koper, A. G. Visser, and B. J. M. Heijmen, "In vivo dosimetry for prostate cancer patients using an electronic portal imaging device (EPID): detection of internal organ motion," *Radiother. Oncol.* **49**, 125-32 (1998).
- ⁶D. A. Low, W. B. Harms, S. Mutic, and J. A. Purdy, "A technique for the quantitative evaluation of dose distributions," *Med. Phys.* **25**, 656-61 (1998).
- ⁷B. J. Mijnheer, J. J. Battermann, and A. Wambersie, "What degree of accuracy is required and can be achieved in photon and neutron therapy?," *Radiother. Oncol.* **8**, 237-52 (1987).
- ⁸K. L. Pasma, M. Kroonwijk, J. C. J. de Boer, A. G. Visser, and B. J. M. Heijmen, "Accurate portal dose measurement with a fluoroscopic electronic portal imaging device for open and wedged beams and dynamic multileaf collimation," *Phys. Med. Biol.* **43**, 2047-60 (1998).
- ⁹K. L. Pasma, M. L. P. Dirkx, M. Kroonwijk, A. G. Visser, and B. J. M. Heijmen, "Dosimetric verification of intensity modulated beams produced with dynamic multileaf collimation using an electronic portal imaging device," *Med. Phys.* **26**, 2373-78 (1999a).
- ¹⁰K. L. Pasma, M. Kroonwijk, S. Quint, A. G. Visser, and B. J. M. Heijmen, "Transit dosimetry with an electronic portal imaging device (EPID) for 115 prostate cancer patients prostate," *Int. J. Radiat. Oncol. Biol. Phys.* **45**, 1297-03 (1999b).

CHAPTER 4. FAST AND ACCURATE LEAF VERIFICATION FOR DYNAMIC MULTILEAF COLLIMATION USING AN EPID

S C Vieira, M L P Dirkx, K L Pasma, B J M Heijmen

Med. Phys. **29**, 2034-2040, 2002

4.1 Abstract

A prerequisite for accurate dose delivery of IMRT profiles produced with dynamic multileaf collimation (DMLC) is highly accurate leaf positioning. In our institution, leaf verification for DMLC was initially done with film and ionization chamber. To overcome the limitations of these methods, a fast, accurate and two-dimensional method for daily leaf verification, using our CCD-camera based electronic portal imaging device (EPID), has been developed. This method is based on a flat field produced with a 0.5 cm wide sliding gap for each leaf pair. Deviations in gap widths are detected as deviations in grey scale value profiles derived from the EPID images, and not by directly assessing leaf positions in the images. Dedicated software was developed to reduce the noise level in the low signal images produced with the narrow gaps. The accuracy of this quality assurance procedure was tested by introducing known leaf position errors. It was shown that errors in leaf gap as small as 0.01-0.02 cm could be detected, which is certainly adequate to guarantee accurate dose delivery of DMLC treatments, even for strongly modulated beam profiles. Using this method, it was demonstrated that both short and long term reproducibility in leaf positioning were within 0.01 cm (1σ) for all gantry angles, and that the effect of gravity was negligible.

4.2 Introduction

Intensity modulated radiotherapy (IMRT) is a powerful tool for delivery of conformal dose distributions. There are several ways of producing IMRT fields: by compensators,¹ tomotherapy,² segmental multileaf collimation ("step and shoot"),^{3,4} or dynamic multileaf collimation (DMLC).⁵⁻¹² The first DMLC treatment was performed in 1995

for a prostate cancer patient at the Memorial Sloan-Kettering Cancer Center, NY.¹¹ At the Daniel den Hoed Cancer Center (DDHCC, Rotterdam, The Netherlands), we started using DMLC in 1999 for patients with head and neck cancer who were treated on the MM50 Racetrack Microtron (Scanditronix Medical AB, Uppsala, Sweden).¹² Due to the complexity of these treatments, rigorous quality assurance (QA) is mandatory. An important aspect of the QA procedure is related to the mechanical accuracy of the multileaf collimator (MLC) in DMLC mode, including leaf calibration, stability of leaf speed, and effects of acceleration and deceleration of leaf motion.

To perform leaf verification for DMLC, Chui *et al.*¹³ proposed the use of a sliding slit beam of 0.1 cm width, which was stopped at several equally spaced control positions. At these positions, film measurements showed straight dark lines, if the leaves were positioned correctly. Using this method, they could detect errors in leaf position of about 0.02 cm. To monitor the stability in gap width, LoSasso *et al.*¹⁴ measured the dose in the center of a uniform 10×10 cm² field, realized by a 0.4 cm slit beam, using an ionization chamber. The dose delivered within this DMLC field is highly sensitive to the actual leaf gap sweeping across the field; a deviation of only 0.01 cm in a 0.4 cm leaf gap width, results in a dose difference of about 2.5%. Both tests were also used in our institute as part of a quality assurance procedure for DMLC treatments on the MM50 Racetrack¹⁵ and on the Varian 2300C/D (Varian Oncology Systems, Palo Alto, CA).¹⁶ Several groups have used Electronic Portal Imaging Devices (EPID) for geometrical approaches to verify leaf motion while delivering a DMLC treatment.¹⁷ A difference of about 0.1 cm between prescribed and realized leaf positions, as assessed from the EPID images, could be detected.

The above mentioned methods for QA on leaf positioning have some drawbacks. The procedure developed by Chui *et al.*¹³ using film is accurate but allows leaf verification to be performed only at the control positions where the sliding gap stops, by comparing leaf pairs relative to each other. In our experience, to quantify leaf gap deviations with an accuracy of 0.02 cm, the film should be scanned, which is time consuming. The ionization chamber method used by LoSasso *et al.*¹⁴ can measure the reproducibility of a leaf gap accurately, but offers the possibility to perform this check for one leaf pair and one point at a time only. Moreover, for this method quite some set-up time at the treatment unit is required. On the other hand, the reported accuracy of 0.1 cm, encountered by monitoring leaf positions with an EPID,¹⁷ may not be sufficient if highly modulated beams are used.¹⁸

In DDHCC, we are using fluoroscopic EPIDs for dosimetric verification.¹⁹⁻²² Since 1994, these systems are applied for daily verification of the beam output and beam flatness of static fields on the MM50 Racetrack Microtron.¹⁹ Recently, we started using the EPID to perform pre-treatment dosimetric verification of each clinically used IMRT field realized with DMLC.²² Based on this experience with EPIDs, we have extended the method described by LoSasso *et al.*¹⁴ to a full 2D, fast and accurate QA procedure for leaf verification. This procedure overcomes the drawbacks of the previously mentioned methods. In this paper, the method is described in detail and its level of accuracy is assessed. The reproducibility in gap width of a sliding slit beam is investigated by examining short and long term variations, and variations under gantry rotation.

4.3 Materials and Methods

4.3.1 The MLC

In this study, all measurements were performed on a Varian 2300C/D. This linac is equipped with a 40 leaf pair MLC (Mark II), each leaf having a width of 1 cm at the isocenter plane. The maximum field realized with the MLC is $40 \times 40 \text{ cm}^2$. The leaves have a maximum overtravel across the beam axis of 16 cm. The maximum distance that one leaf can be extended beyond another on the same carriage is 14.5 cm. The maximum leaf speed is 3 cm s^{-1} .

A DMLC treatment field is divided in a number of segments; each segment contains a fraction of the number of monitor units (MU) to be delivered and the prescribed leaf positions at that time. The leaf positions are transferred from the treatment planning system to the MLC controller of the treatment unit by network, using an ascii file.

When the linac is powered on, leaves are automatically calibrated by successively positioning each leaf in front of an infrared beam. The infrared beam source is located inside the treatment unit head, generating a light beam perpendicular to the direction of leaf motion. The calibration of each leaf can be assessed because the distance between the leaf carriage and the infrared beam is known.

4.3.2 The EPID

A fluoroscopic Theraview NT EPID (Cablon Medical, Leusden, The Netherlands), low elbow type, is attached to the Varian linac. The EPID is equipped with a CCD camera (Adimec MX12), which detects the optical signal, originated from a fluorescent screen and reflected by a 45° tilted mirror. The fluorescent screen (FS), positioned for this study at 150 cm from the focus, contains a layer of gadolinium oxysulphide coated onto a 2 mm thick brass build-up plate.²³ An additional buildup layer of 1 mm stainless steel is used for dosimetric purposes.²⁰ This extra layer hardly affects image quality. The CCD camera is connected by means of an optical fiber to a PC containing a frame grabber. Image acquisition is performed using the EPID software running on a Windows application. In the EPID image, pixel (or grey scale) values can range from 0 to 1023 ADC units. Each EPID image is the sum of a number of individual frames, acquired with a given integration time. The summed image, divided by the total number of frames, is then corrected for the dark current, which is measured just prior to the start of the irradiation. In the clinical software version, only the resulting EPID image is stored. For this study, a research version of the EPID software was used, which made possible to store not only the summed EPID image but also the individual frames. This feature was used to enable noise reduction (Sec. II D.).

The EPID system has three characteristics most relevant to our measurements: (i) the signal is integrated simultaneously in 1024×1024 pixels, each measuring $0.025 \times 0.025 \text{ cm}^2$ at the isocenter plane, (ii) the CCD read out time for a measured frame (during which no signal is accumulated) is only 2 ms, and (iii) an excellent short and long term stability.²³

4.3.3 Description of the sliding gap measurements

All measurements were performed using a 6 MV photon beam, running at a dose rate of 600 MU/min. Except for the measurements described in Sec. II E., a uniform $10.5 \times 20 \text{ cm}^2$ field was delivered dynamically by sweeping a prescribed $0.5 \times 20 \text{ cm}^2$ slit across the field with constant velocity (0.3 cm s^{-1}). The blocks were set to $10.5 \times 20 \text{ cm}^2$ in order to minimize transmission through the leaves outside the field. During each measurement, a total of 30 EPID frames were acquired, one of these frames is shown in Fig. 4-1(a). The integration time for each frame was 1.4 s. The total acquisition time was always longer than the time required for the DLMC field delivery. The

field center in the EPID images was derived from the borders of a static $20 \times 20 \text{ cm}^2$ field image, acquired for the same gantry angle. This static field is also used to verify the performance of the EPID on the day of measurement.¹⁹

In this paper, the x and y position coordinates are defined in the direction of leaf motion, and perpendicular to this, respectively [Fig.4-1]. Unless mentioned otherwise, all dimensions are measured in the isocenter plane. For coordinates measured in the EPID plane, (x_{FS}, y_{FS}) are used.

4.3.4 Image processing

In the sliding gap measurement, most points in the EPID plane receive primary radiation during one camera frame only, due to the applied narrow leaf gap; for these points, the other camera frames are only filled with signal resulting from leaf transmission and camera noise. Consequently, when simply summing the individual frames, as is done in the clinical version of the EPID software, noise significantly contributes to the signal in the resulting EPID image. Due to the poor signal to noise ratio, small deviations in leaf gap width cannot be detected.

In order to reduce this noise level, four steps were performed for each individual frame, after subtracting the dark current and prior to adding the frames. First, a median filter was applied within a region of $0.075 \times 0.075 \text{ cm}^2$ to remove isolated high or low values resulting from damage to the CCD chip. Secondly, for each leaf pair, j , the middle 13 grey scale value profiles, $g_{j, \text{raw}}(x)$, were averaged in the direction perpendicular to the leaf motion [Fig. 4-1(b)]. In this direction, only minor variations in pixel values were observed for these 13 middle profiles, but for adjacent lines, $g_{j, \text{raw}}(x)$ was increasing due to the influence of leaf leakage between adjacent leaves, as observed in the measured y profiles. Thirdly, transmission through the leaves and the blocks was subtracted, as shown in Fig. 4-1(c) by the horizontal line. The transmission was determined by averaging the pixel values at a distance larger than 3 cm (at the EPID plane) from the peak. After transmission subtraction, all negative pixel values were set to zero. Finally, and most importantly, the pixel values at all points within the frame, located at a distance larger than 3 cm (at the EPID plane) from the peak center, were set to zero (as indicated by the vertical lines in Fig. 4-1(d)). By setting the pixel values to zero beyond 3 cm from the peak center, where the signal reached a plateau, all primary and scattered radiation were still included in the signal of the frame, while minimizing the contribution of noise. Cross-talk within the EPID images²⁰ was also

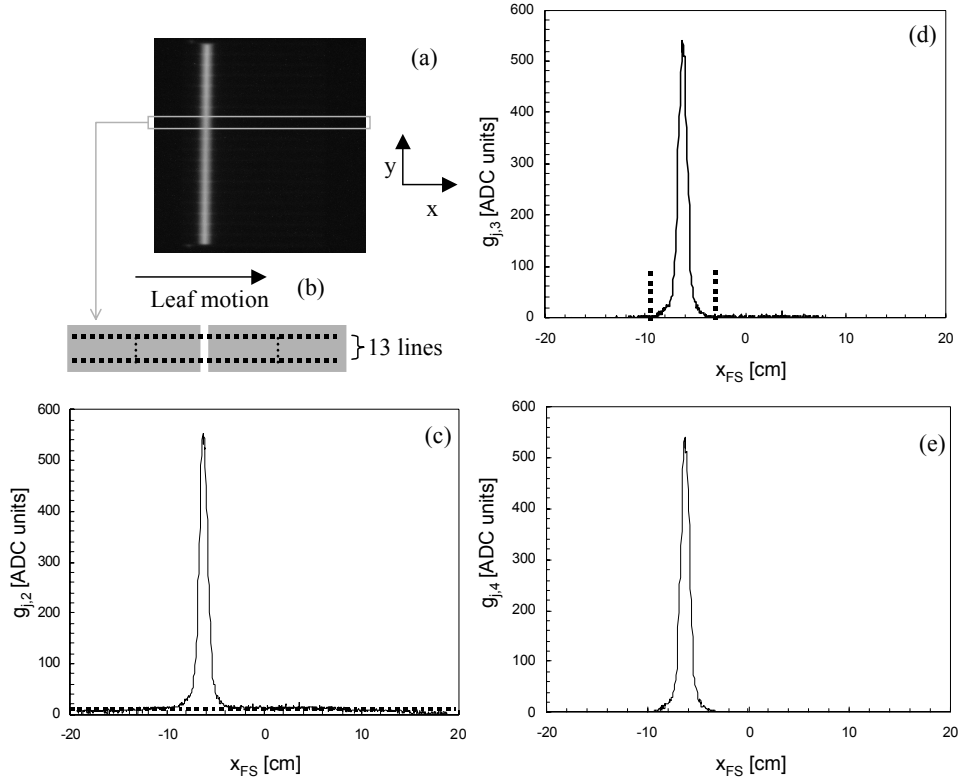


Figure 4-1 (a) A single frame image of a sweeping $0.5 \times 20 \text{ cm}^2$ slit beam. In (b), (c), and (d), different steps of our image processing are represented, finally yielding the processed frame depicted in (e). In the second step (b), 13 grey scale value profiles in the middle of the leaf pair are averaged perpendicularly to the direction of leaf motion, yielding $g_{j,2}(x)$. In the third step (c), leaf transmission is subtracted in each frame as represented by the horizontal dashed line, yielding $g_{j,3}(x)$. In the fourth step (d), measured grey scale values beyond the two vertical dashed lines are set to zero, yielding $g_{j,4}(x)$. For the measurements, collimator blocks were placed at $x_{FS} = -8.5 \text{ cm}$ and $x_{FS} = 8.5 \text{ cm}$.

removed by performing this step. In Fig. 4-1(e) is shown the resulting frame image after these four steps. Next, the frames were summed to get the final grey scale profile, $G_j(x)$, for each individual leaf pair. In the end, a smoothing filter was applied within a region of $0.125 \times 0.125 \text{ cm}^2$, in order to remove remaining high frequency noise from the images.

The above mentioned image processing was performed by means of a routine developed in our institute and programmed using the Interactive Data Language 5.3 (Research Systems, Boulder, CO). The total amount of time required for the acquisi-

tion of the static field and the IMRT field, and for the succeeding image processing, is 3 minutes.

4.3.5 Relation between leaf gap width and measured EPID signal

In order to establish the relation between the *nominal* leaf gap width, w , and the EPID signal for our measurements, the procedure described in Sec. II C. was performed for a uniform $10 \times 20 \text{ cm}^2$ field realized by sweeping a 0.3, 0.4, 0.5, 0.6, 0.7, and 0.8 cm nominal gap, respectively. All leaf gaps traveled at the same velocity (0.3 cm s^{-1}). After image processing (Sec. II D.), the grey scale values of the resulting profiles, $G_j(x)$, were averaged in the direction of leaf motion over 8 cm, therefore neglecting the penumbra, yielding $G_{j,c}$. These average grey scale values were then normalized to the average value of the uniform field realized by the 0.5 cm gap. This gap width was chosen because it is used in all our QA measurements. In this way, for a given QA check, differences in EPID signal can directly be related to differences in leaf gap width.

4.3.6 Detection of leaf position errors

To assess the accuracy of our method, we simulated leaf position errors, Δw . Each simulated error was introduced in one leaf pair only. In the DMLC file sent to the treatment unit, the sliding leaf gap was programmed to have a nominal width of 0.5 cm at the start of the irradiation, $(0.5 - \Delta w)$ half way, and again 0.5 cm at the end of the treatment. These images were compared with an EPID image acquired using a dynamic field of 0.5 cm gap width, without simulated errors in leaf positions.

4.3.7 Reproducibility of QA measurements

In order to establish the short term reproducibility of the QA measurements performed on our linac, four EPID images were successively acquired, as described in Sec. II C., within a short time interval. After performing image processing in each image, the grey scale values in the resulting profile of each leaf pair, $G_j(x)$, were averaged in the direction of leaf motion, yielding $G_{j,c}$ (Sec. II E.). The short term stability was defined as the standard deviation, σ , of these values in the four images. This standard deviation was determined separately for gantry angles 0° , 90° and 270° .

Differences in leaf calibration between different leaf pairs were assessed, by calculating the average grey scale values over a region of $0.25 \times 0.25 \text{ cm}^2$, at the central axis of each leaf pair. These values were then divided by the grey scale values measured in a static centered field of $1 \times 20 \text{ cm}^2$, to correct for variations in the y direction, in EPID response²⁰ and shape of the dose profile, as delivered by the treatment unit.

To study the long term reproducibility, a sliding gap field was measured 21 times over a 50 days period, for gantry angles of 0° , 90° , and 270° . To overcome the limitation that leaves have a limited range of travel with respect to their corresponding carriage, and to be able to verify the reproducibility of the sliding leaf gap over the maximum field that can be detected with the EPID, two, 1 cm overlapping, fields (left and right) with dimensions of $10.5 \times 20 \text{ cm}^2$, were used. On the first day, the measurements were repeated three times. For each field, image processing was performed for the four EPID images and the average image was calculated, which was then defined as the reference. On the same day, a film was irradiated following the method proposed by Chui *et al.*¹³ to ensure that the reference images were acquired in currently acceptable conditions of leaf calibration. In the following days, one EPID image was acquired for each field. The percentage differences between these grey scale values and the grey scale values in the reference image were calculated, for each gantry angle and for each field. The long term stability was defined as the standard deviation of this percentage differences averaged over all leaf pairs, in the 50 days study period.

The EPID images used to assess the long term stability for each gantry angle, were also used to investigate the influence of gravity on gap motion in the same period of

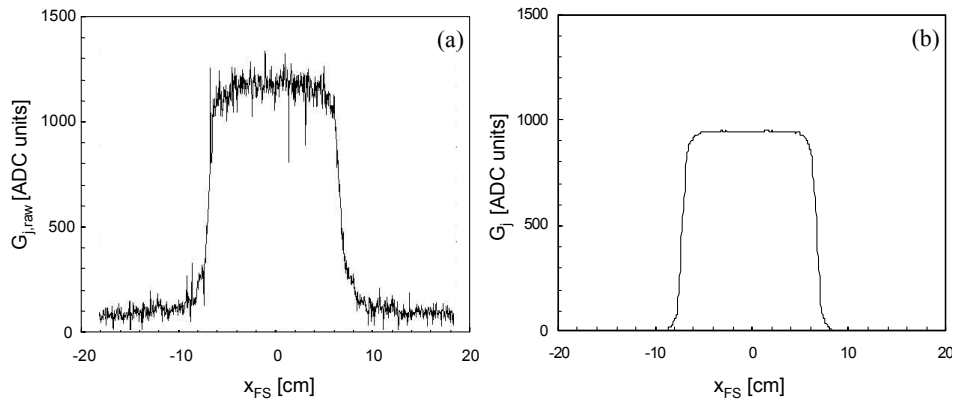


Figure 4-2 Grey scale profiles in the direction of leaf motion after summing individual EPID frames, (a) without and (b) after image processing.

time. The influence of gravity was derived by the percentage difference in $G_{j,c}$, between the images at 90° and 270° gantry angles, and the image at 0° gantry angle, averaged over all measurement days and all leaf pairs.

4.4 Results

4.4.1 Image processing

To show the effects of our image processing routine, two profiles in the direction of leaf motion are compared for one EPID measurement [Fig. 4-2]. In the left profile, [Fig. 4-2(a)], all individual EPID frames were summed and corrected for dark current but no extra noise reduction steps were performed, yielding $G_{j,raw}(x)$. This image would be obtained with the clinical version of our EPID software, after filtering isolated high and low pixel values. For the same measurement, frames were processed as described in Sec. II D. before summing them, [Fig. 4-2(b)]. While in Fig. 4-2(a) the noise exceeds the $\pm 5\%$ level, it could be reduced to about 1% by our image processing. Because in our QA measurements, EPID images are analyzed relative to a reference measurement, deviations of the order of 2% should be detectable. By comparing the profiles in Fig. 4-2(a) and 4-2(b), a difference in height is observed, which is mainly due to the subtraction of leaf transmission in the second step of the image processing.

4.4.2 Relation between leaf gap width and measured EPID signal

By performing the measurements for nominal leaf gap widths of 0.3, 0.4, 0.5, 0.6, 0.7, and 0.8 cm, a calibration curve could be made. As shown in Fig. 4-3, the EPID signal, $G_{j,c}$, changes linearly with the leaf gap width, w . Ac-

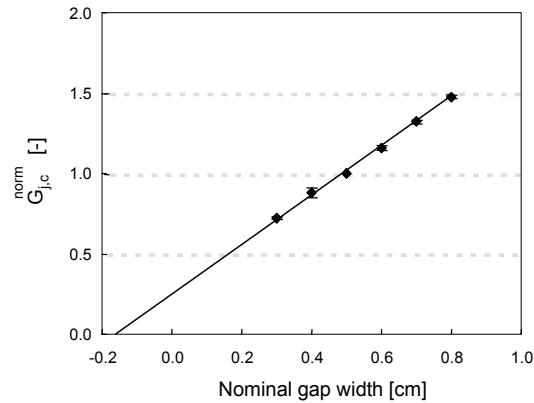


Figure 4-3 Averaged grey scale values in the uniform field, $G_{j,c}$, realized by different leaf gap widths, w , and normalized to the average value for the uniform field realized by a sweeping gap of 0.5 cm width, yielding $G_{j,c}^{norm}$.

cording to this calibration curve, a change in EPID signal of 3% corresponds to a change in gap width of 0.02 cm, when using a sweeping leaf gap of 0.5 cm as a reference. Due to the fact that the leaves of the Varian MLC have rounded edges, the *nominal* leaf gap width is smaller than the *effective* leaf gap. By performing regression analysis to the data in Fig. 4-3, a difference of 0.18 cm between both values was found, which is in agreement with results obtained by others.^{14,16}

4.4.3 Detection of leaf position errors

The relative differences between the measured grey scale value profiles, $G_j(x)$, with and without introduced nominal errors, Δw , are shown in Fig. 4-4, for two leaf pairs. In the center of the field, differences in signal of -9% and -3% were detected by the introduction of a 0.05 cm and 0.02 cm error in the 0.5 cm nominal leaf gap, respectively. The fact that an error in gap width of 0.02 cm can easily be detected, indicates that the accuracy of our method is 0.01-0.02 cm.

4.4.4 Reproducibility of QA

measurements

The short term reproducibility of the measured grey scale values was 0.3% (1σ), at gantry angles of 0° , 90° , and 270° . This value found is similar to the EPID short term reproducibility of 0.2% (1σ) already reported by others for gantry angle 0° using a static field.^{19,23}

No significant variation could be observed in the gap widths of the different leaf pairs. As shown in Fig. 4-5, the difference between the measured gap width for each leaf pair and the average width over all leaf pairs did not exceed

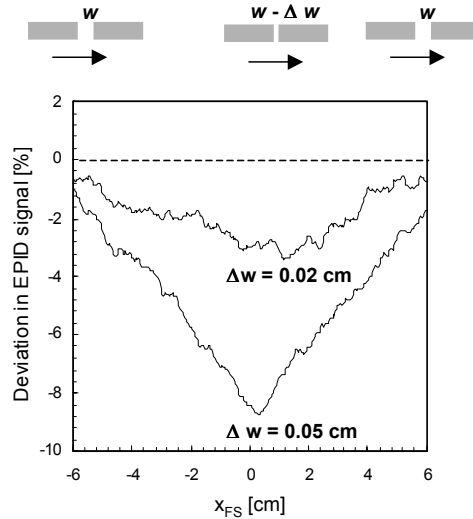


Figure 4-4 Relative differences between grey scale profiles with and without introduced errors, Δw , in the 0.5 cm leaf gap width, w . The introduced errors were 0.02 cm and 0.05 cm, respectively.

0.02 cm, being within the accuracy of our method.

The long-term stability of the measured leaf gap widths at gantry angle 0° is depicted in Fig. 4-6, for one leaf pair. For all leaf pairs, a variation of 0.01 cm (1σ) was detected, in the 50 days study period, for all gantry angles. At one day, a significantly higher deviation was observed, not only for the particular leaf pair shown in Fig. 4-6, but also for the other leaf pairs and for the

different gantry angles. A possible explanation for this deviation might be a calibration error of all leaves for that particular day, resulting in a deviation in gap width of 0.04 cm. It is unlikely that this deviation would be due to the performance of the EPID on that day, because no significant deviations were found between the static field acquired at the same day and the other days of measurement. Although this deviation is within the required tolerances for DMLC delivery,¹⁸ it indicates the importance of this QA check.

The mean gap width differences with respect to gantry angle 0° , over a period of 50 days, were -0.01 ± 0.02 cm (1σ) and 0.00 ± 0.01 cm (1σ) for the gantry angles 90° and 270° respectively, indicating that gravity has a negligible effect.

4.4.5 Gap width variations with high spatial frequencies

By closely examining the peaks in individual frames, signal variations may be observed [Fig. 4-7],

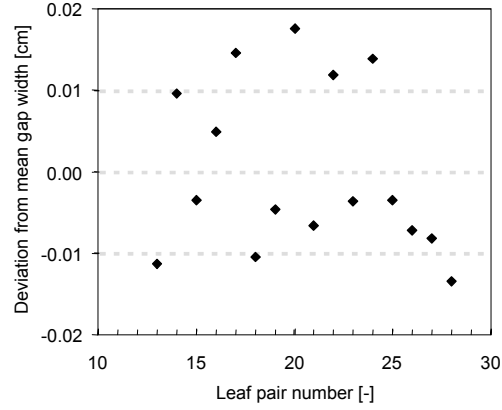


Figure 4-5 Gap width differences for different leaf pairs.

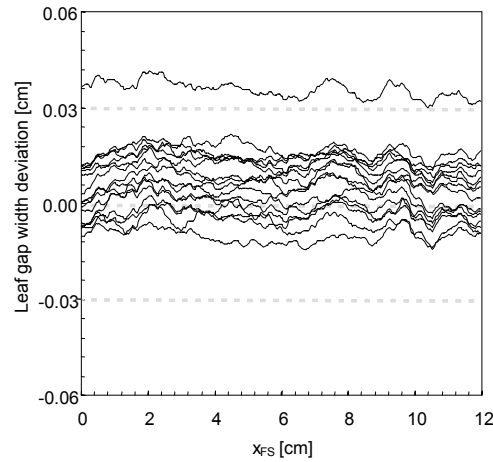
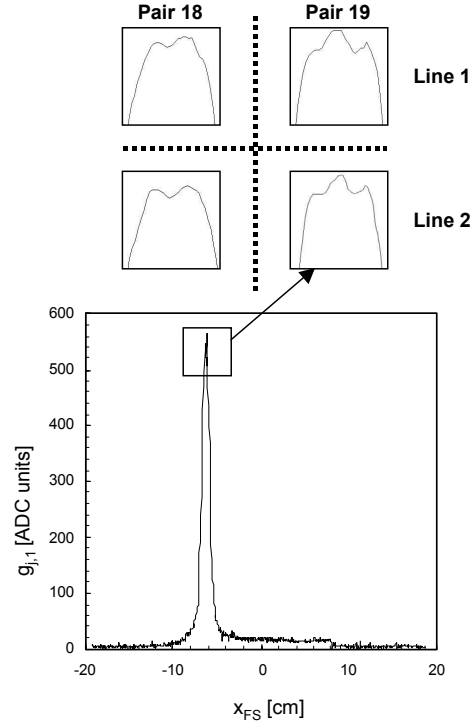


Figure 4-6 Each line of the graph represents the deviation in gap width with respect to the reference image at one day of measurement.

that can not be attributed to noise. For each leaf pair, there is a common signal pattern for the 13 central grey scale profiles, $g_{j,1}(x)$, which are averaged in step 2 of the image processing. In Fig.4-7, two of these lines are shown. Different leaf pairs have different patterns. Static EPID images acquired at the same day do not show these local signal variations. Probably, the signal variations arise from short and minor variations (less than 0.02 cm) in the leaf gap width, while the leaves are travelling across the field.



4.5 Discussion

The leaf verification method described in this article is being used for constancy checks, where deviations in leaf gaps are measured relative to a 0.5 cm *nominal* leaf gap width as selected for acquisition of the reference images (Sec. II G.). In order to allow absolute leaf gap width verification, a feeler gauge could be used to measure the actual leaf gap width when the reference images are acquired. Actually, these absolute measurements need to be performed for one leaf pair only, because the leaf calibration for different leaf pairs does not differ significantly, as seen from Fig. 4-5.

The proposed QA method has been tested for one particular MLC. Probably it can be implemented for multileaf collimators with other leaf widths as well. Some alterations in the image processing procedure should then be performed in order to achieve the same signal to noise ratio as stated in this paper. For instance, the number of the middle grey scale value profiles chosen for averaging, as performed in step two of the image processing (Sec. II D.), has to be determined for another multileaf collimator.

Figure 4-7 Variation in measured grey scale values, $g_{j,1}$, on the top of the peak in a single frame image. Four top peak profiles are shown in the direction of leaf motion: two, measured under the same leaf pair (line 1 and line 2), and two under different leaf pairs (pair 18 and pair 19).

This leaf verification method is used as a quick morning check of the calibration and the performance of the MLC, prior to the start of patient treatments. In addition to this daily check of the treatment unit, also patient specific dosimetric tests are performed with the EPID, both prior to the start of the fractionated treatment (pre-treatment verification),²² and weekly during the treatment. For pre-treatment verification, the treatment planning system is used to calculate for each IMRT field an absolute, two dimensional dose distribution in the plane of the EPID, based on the leaf sequences that will be used for treatment of the patient. Prior to the first treatment fraction, these dose distributions are measured with the EPID and compared with the prediction. Deviations may point at problems with the leaf sequencing algorithm or with data transfer between the treatment planning system and the treatment unit. The weekly dosimetrical measurements during the treatment are used to check constancy.

4.6 Conclusions

Our QA measurements using the EPID can detect differences in leaf gap width of 0.01-0.02 cm. In one single measurement, 2D information is obtained, verifying the reproducibility of the leaf gap width for all leaf pairs at the same time. In this method, constancy of the absolute measured grey scale values is required. This is in contrast, in one hand, with the use of EPIDs for patient set-up verification, where high contrast between anatomical structures is important, (i.e. high relative differences between the grey scale values); and, on the other hand, with dosimetric verification,^{22,24,25} where dosimetric calibration of the EPID is required. The method is fast, due to the fact that the EPID is already attached to the accelerator and no extra set-up time is required. By using the EPID, leaf verification can easily be performed for different gantry angles. Presently, this QA procedure is in daily use.

4.7 Acknowledgments

The authors would like to thank Jaco Barnhoorn for his contribution to the development of the research version of the EPID software. This work was supported by the 'Fundação para a Ciência e a Tecnologia' and by the Dutch Cancer Society (grant DDHK 98-1681).

4.8 References

- ¹S. B. Jiang and K. M. Ayyangar, "On compensator design for photon beam intensity-modulated conformal therapy," *Med. Phys.* **25**, 668-675 (1998).
- ²T. R. Mackie, T. Holmes, S. Swerdloff, P. Reckwerdt, J. O. Desay, J. Yang, B. Paliwal, and T. Kinsella, "Tomotherapy - a new concept for the delivery of dynamic conformal radiotherapy," *Med. Phys.* **20**, 1709-1719 (1993).
- ³J. M. Galvin, X. G. Chen, and R. M. Smith, "Combining multileaf fields to modulate fluence distributions," *Int. J. Rad. Oncol. Biol. Phys.* **27**, 697-705 (1993).
- ⁴T. R. Bortfeld, D. L. Kahler, T. J. Waldron, and A. L. Boyer, "X-ray field compensation with multileaf collimators," *Int. J. Rad. Oncol. Biol. Phys.* **28**, 723-730 (1994).
- ⁵D. J. Convery and M. E. Rosenbloom, "The generation of intensity-modulated fields for conformal radiotherapy by dynamic multileaf collimation," *Phys. Med. Biol.* **37**, 1359-1374 (1992).
- ⁶S. V. Spirou and C. S. Chui, "Generation of arbitrary intensity profiles by dynamic jaws or multileaf collimators," *Med. Phys.* **21**, 1031-1041 (1994).
- ⁷J. Stein, T. Bortfeld, B. Dörschel, and W. Schlegel, "Dynamic X-ray compensation for conformal radiotherapy by means of multi-leaf collimation," *Radiother. Oncol.* **32**, 163-173 (1994).
- ⁸R. Svensson, P. Källman, and A. Brahme, "An analytical solution for the dynamic control of multileaf collimators," *Phys. Med. Biol.* **39**, 37-61 (1994).
- ⁹J. P. C. van Santvoort and B. J. M. Heijmen, "Dynamic multileaf collimation without 'tongue-and-groove' underdosage effects," *Phys. Med. Biol.* **41**, 2091-2105 (1996).
- ¹⁰M. L. P. Dirkx, B. J. M. Heijmen, and J. P. C. van Santvoort, "Leaf trajectory calculation for dynamic multileaf collimation to realize optimised fluence profiles," *Phys. Med. Biol.* **43**, 1171-1184 (1998).
- ¹¹C. C. Ling, C. Burman, C. S. Chui, G. J. Kutcher, S. A. Leibel, T. LoSasso, R. Mohan, T. Bortfeld, L. Reinstein, S. Spirou, X. H. Wang, Q. Wu, M. Zelefsky, and Z. Fuks, "Conformal radiation treatment of prostate cancer using inversely-planned intensity-modulated photon beams produced with dynamic multileaf collimation," *Int. J. Rad. Oncol. Biol. Phys.* **35**, 721-730 (1996).
- ¹²E. B. van Dieren, P. J. C. M. Novak, O. B. Wijers, J. R. V. de Koste, H. van der Est, D. P. Binnekamp, B. J. M. Heijmen, and P. C. Levendag, "Beam intensity modulation using tissue compensators or dynamic multileaf collimation in three-dimensional conformal radiotherapy of primary cancers of the oropharynx and larynx, including the elective neck," *Int. J. Rad. Oncol. Biol. Phys.* **47**, 1299-1309 (2000).
- ¹³C. S. Chui, S. V. Spirou, and T. LoSasso, "Testing of dynamic multileaf collimation," *Med. Phys.* **23**, 635-641 (1996).
- ¹⁴T. LoSasso, C. S. Chui, and C. C. Ling, "Physical and dosimetric aspects of a multileaf collimation system used in dynamic mode for implementing intensity modulated radiotherapy," *Med. Phys.* **25**, 1919-1927 (1998).
- ¹⁵M. L. P. Dirkx and B. J. M. Heijmen, "Testing of the stability of intensity modulated beams generated with dynamic multileaf collimation, applied to the MM50 Racetrack Microton," *Med. Phys.* **27**, 2701-2707 (2000).

-
- ¹⁶M. Essers, M. de Langen, M. L. P. Dirkx, and B. J. M. Heijmen, "Commissioning of a commercially available system for intensity-modulated radiotherapy dose delivery with dynamic multileaf collimation," *Radiother. Oncol.* **60**, 215-224 (2001).
- ¹⁷M. Partridge, P. M. Evans, M. van Herk, L. S. Ploeger, G. J. Budgell, and H. V. James, "Leaf position verification during dynamic beam delivery: A comparison of three applications using electronic portal imaging," *Med. Phys.* **27**, 1601-1609 (2000).
- ¹⁸G. J. Budgell, J. H. L. Mott, P. C. Williams, and K. J. Brown, "Requirements for leaf position accuracy for dynamic multileaf collimation," *Phys. Med. Biol.* **45**, 1211-1227 (2000).
- ¹⁹M. L. P. Dirkx, M. Kroonwijk, J. C. J. de Boer, and B. J. M. Heijmen, "Daily dosimetric quality control of the MM50 racetrack microton using an electronic portal imaging device," *Radiother. Oncol.* **37**, 55-60 (1995).
- ²⁰K. L. Pasma, M. Kroonwijk, J. C. J. de Boer, A. G. Visser, and B. J. M. Heijmen, "Accurate portal dose measurement with a fluoroscopic electronic portal imaging device for open and wedged beams and dynamic multileaf collimation," *Phys. Med. Biol.* **43**, 2047-2060 (1998).
- ²¹K. L. Pasma, M. Kroonwijk, S. Quint, P. C. M. Koper, A. G. Visser, and B. J. M. Heijmen, "Transit dosimetry with an electronic portal imaging device for 115 prostate cancer patients," *Int. J. Rad. Oncol. Biol. Phys.* **45**, 1297-1303 (1999).
- ²²K. L. Pasma, M. L. P. Dirkx, M. Kroonwijk, A. G. Visser, and B. J. M. Heijmen, "Dosimetric verification of intensity modulated beams produced with dynamic multileaf collimation using an electronic portal imaging device," *Med. Phys.* **26**, 2373-2378 (1999).
- ²³J. C. J. de Boer, B. J. M. Heijmen, K. L. Pasma, and A. G. Visser, "Characterization of a high elbow, fluoroscopic electronic portal imaging device for portal dosimetry," *Phys. Med. Biol.* **45**, 197-216 (2000).
- ²⁴J. Chang, G. S. Mageras, C. S. Chui, C. C. Ling, and W. Lutz, "Relative profile and dose verification of intensity-modulated radiation therapy," *Int. J. Rad. Oncol. Biol. Phys.* **47**, 231-240 (2000).
- ²⁵A. van Esch, B. Vanstraelen, J. Verstraete, G. Kutcher, and D. Huyskens, "Pre-treatment dosimetric verification by means of a liquid-filled electronic portal imaging device during dynamic delivery of intensity modulated treatment fields," *Radiother. Oncol.* **60**, 181-190 (2001).

CHAPTER 5. FAST, DAILY LINAC VERIFICATION FOR SEGMENTED IMRT USING ELECTRONIC PORTAL IMAGING

S C Vieira, R A Bolt, M L P Dirksen, A G Visser, B J M Heijmen

Radiother. Oncol. *to be submitted*, 2005

5.1 Abstract

Intensity modulated radiotherapy (IMRT) requires dedicated quality assurance (QA). Recently, we have published a method for fast (1-2 minutes) and accurate linac quality control for dynamic multileaf collimation (DMLC), using a portal imaging device (EPID). This method is in routine use for daily leaf motion verification. The purpose of the present study was to develop an equivalent procedure for QA of IMRT with segmented (static) multileaf collimation (SMLC). It was based on measurements performed during 3-8 months periods at Elekta, Siemens and Varian accelerators. On each measurement day, images were acquired for a field consisting of five $3 \times 22 \text{ cm}^2$ segments. These 10 monitor unit (MU) segments were delivered in SMLC mode, moving the leaves from left to right. Deviations of realized leaf gap widths from the prescribed width were analyzed to study the leaf positioning accuracy. To assess hysteresis in leaf positioning, the sequential delivery of the SMLC segments was also inverted. A static $20 \times 20 \text{ cm}^2$ field was delivered with exposures between 1 and 50 MU, to study the beam output and beam profile at low exposures. Dedicated software was developed to improve the signal to noise ratio and to correct for image distortion. The observed long-term leaf gap reproducibility (1 standard deviation) was 0.09 mm, 0.22 mm, and 0.21 mm for the Varian, the Siemens, and the Elekta accelerators, respectively. In all cases the hysteresis was negligible. For exposures of 2 MU or higher, the beam output and beam profile were stable within 2% and 1%, respectively, for all accelerators. These findings led to a fast (3-4 minutes) procedure for accurate, daily linac quality control for SMLC.

5.2 Introduction

A prerequisite for accurate dose delivery during intensity modulated radiotherapy (IMRT) with segmented multileaf collimation (SMLC), is highly accurate leaf positioning. Even uncertainties in leaf position smaller than a millimeter can cause dose deviations of several percent.¹ In addition, SMLC fields may include several low exposure segments (< 10 monitor units (MU)). Therefore, dose delivery for small MU segments should be accurate and stable, both regarding absolute dose and beam profile.²⁻⁴

Several authors have developed methods to verify the performance of the multileaf collimator (MLC) for SMLC delivery.^{1,5-9} A method to calibrate the Varian MLC was presented by Graves *et al.*⁷ Quality assurance (QA) issues of this curved leaf-end MLC were covered as well. Using data acquired at a Siemens accelerator, Bayouth *et al.*⁵ developed a technique to measure the absolute position of each leaf based on dosimetric information, following MLC calibration. Low *et al.*¹ and Sastre-Padro *et al.*⁸ investigated the SMLC delivery accuracy for a Varian linac, and a leaf calibration method for the Elekta MLC, respectively, relying on the fact that errors in leaf positioning cause corresponding errors in the delivered dose in a field abutment region. All the above-mentioned QA tests were performed with ionization chamber and/or film. Ionization chamber measurements do not provide complete two-dimensional information. Although the use of film overcomes this drawback, the need to develop and scan the film in order to obtain an accuracy of tenths of a millimeter makes it less suited for a routine daily test.

Electronic portal imaging devices (EPIDs) provide high resolution 2-dimensional data, and require virtually no time for set-up or post-processing to obtain useful data. Recently, the use of an EPID to analyze leaf position accuracy was reported.^{10,11} Samant *et al.*¹⁰ presented a method for automated individual leaf position verification using an EPID at a Siemens accelerator. Yang *et al.*¹¹, reported on a method for fast and accurate measurement of MLC leaf positions using the integral signal in a small region of interest as a reliable indicator of the leaf displacement. Both publications focused exclusively on leaf position verification methods, and the studies did not include linacs from all three major vendors. Output and beam profile problems for low exposure fields were not addressed.

The radiotherapy institutes in Rotterdam and Nijmegen have a long tradition in development and clinical application of EPI-based quality assurance procedures, both for patient set-up verification¹²⁻¹⁶ and (*in vivo*) dosimetry.¹⁷⁻¹⁹ As part of our quality

assurance protocol for dynamic multileaf collimation (DMLC), a procedure for daily leaf motion verification with an EPID has been implemented in clinical practice.²⁰ The purpose of this study is to develop an equivalent, 2-dimensional QA procedure for fast, daily SMLC delivery verification, applicable to the three most commonly used linac types. In order to achieve this goal, measurements were performed at a Varian, a Siemens and an Elekta linac, in two institutes. The investigations were focused on verification of leaf positioning, and beam output and beam profile for low exposure fields.

5.3 Materials and methods

All measurements were performed using 6 MV X-ray beams at three different linear accelerators: a Siemens Mevatron Primus (Siemens Medical Systems, Concord, CA), a Clinac 600C (Varian Associates, Palo Alto, CA), and an Elekta Precise (Elekta Limited, Crawley, UK).

5.3.1 The MLCs

The Siemens MLC consists of 27 pairs of leaves with a projected width at isocenter of 1 cm, and 2 pairs of 6.5 cm wide outer leaves. The leaves are double focused and the leaf ends are straight. Each leaf is moved by an independent motor and can travel 10 cm across the beam central axis. The maximum leaf speed is 2 cm s^{-1} at isocenter level.

The Varian millennium MLC is equipped with 120 (2×60) leaves. The width of the central 40 leaves and of the remaining outer leaves is 0.5 cm and 1 cm, respectively. The leaves are mounted on a moving carriage, allowing for leaf movement across the central axis. The maximum over-travel across the beam axis is 16 cm, and the maximum distance from a leaf to the carriage is 14.5 cm. The leaves move along straight lines and have rounded edges. The maximum leaf speed is 3 cm s^{-1} at isocenter.

The Elekta MLC consists of 2×40 leaves with a width of 1 cm and rounded edges. The maximum over-travel is 12.5 cm. The position of each leaf with respect to the MLC frame is assessed by imaging the reflectors built in the upper surface of the leaf, using a CID-camera. The maximum leaf speed is 2 cm s^{-1} at isocenter.

In this paper, the x and y position coordinates are defined in the left-right (AB) direction and in the gun-target (GT) direction, respectively, for all MLC designs.

5.3.2 Leaf calibration

In this study, the MLC calibration for the Siemens linac was performed with the light field of the unit, and a sheet of paper with a 2-dimensional, 1 millimeter grid, placed on the treatment couch at isocenter level. The calibration positions were -10 , 0 , 10 and 20 cm, respectively. The MLC was calibrated by manually moving each individual leaf to these calibration positions, using the light field and the grid lines. Prior to this procedure, for the 20×20 cm² field, the light field - X-ray field coincidence was visually checked using film. The MLC calibration differs from the standard procedure performed by Siemens and is checked every month.

When the Varian linac is powered on, the leaves are automatically calibrated by successively positioning all leaves in front of an infra-red beam. The infra-red beam source is located inside the treatment unit head, generating a beam perpendicular to the direction of leaf motion. The calibration of each leaf can be performed because the distance between the leaf carriage and the infra-red beam is known. Once every month, this automatic leaf calibration was checked with film, and the infra-red beam was adjusted if necessary.

At the Elekta linac, a central leaf (nr.20) of each leaf bank is calibrated first, determining the major offset. In this calibration procedure, a profile under the middle leaf pair is measured in water or with film for collimator angles of 0° and 180° . The leaf pair is considered to be calibrated, if the profile is as flat as possible, i.e., if no significant peaks (caused by over- or underlap of the leaf pair positions) are observed in the sum of the measured profiles. In case the position of the leaf pair 20 needs to be corrected, all the other leaves from the corresponding leaf bank are adjusted by the same amount. Additionally, the calibration of the leaves is checked against the opposing block at the central axis by exposing a film. In this procedure, a very small gap is set between the block and the opposing leaf bank, and deviations in the width of this gap are corrected. This determines the minor offset. Another parameter relevant in the MLC calibration is the gain, common for the whole MLC and used to adjust the off-axis position of the leaf bank with respect to the central axis, and thus the field size. This calibration is performed using the field sizes 10×10 cm² and $30 \times$

30 cm². This MLC calibration differs from the MLC calibration procedure done by Elekta at installation and is performed every month.

5.3.3 The EPID

Fluoroscopic Theraview NT EPIDs (Cablon Medical-Theraview Technology, Leusden, The Netherlands) were used for portal imaging. These systems are equipped with a low noise, cooled CCD-camera. CCD-camera based EPIDs have three characteristics most relevant for QA of IMRT: (i) an excellent short and long term stability (within 0.2% (1SD) and 0.4% (1SD), respectively)²¹, (ii) the signal is integrated simultaneously in all 1024 × 1024 pixels, and (iii) the dead time in between acquisition of subsequent frames is only 0.2 ms.²¹

All measurements in this paper were performed with a frame integration time of 900 ms. The EPID detector plane was positioned at a distance of 150 cm from the focus. All image coordinates pertain to the isocenter plane.

5.3.4 Quality control measurements

5.3.4.1 Accuracy of leaf positioning

For each linac, a SMLC field consisting of five 3 × 22 cm², 10 MU segments was used to study the leaf positioning accuracy (Fig. 5-1). The segments were delivered sequentially, moving the leaves from left (-x) to right (+x). For the Siemens and Varian accelerators, the segments were centered on the positions -10, -5, 0, 5, and 10 cm at the x-axis (direction of leaf motion). For the Elekta accelerator, the positions -9, -5, 0, 5, and 9 cm were used. To investigate possible hysteresis in leaf positioning, the sequential delivery of the SMLC segments was also inverted (i.e., starting the SMLC delivery at 10 cm instead of -10 cm). EPID images were acquired for both SMLC fields. To analyze the long-term reproducibility of the realized leaf gap widths relative to the prescribed width (3 cm), EPID measurements were performed at least 20 times during an 8 months time period at the Siemens and the Varian accelerators, and during a 3 months time period at the Elekta accelerator. The short-term reproducibility of the leaf gap widths was assessed by repeated (5 times) delivery of the SMLC field and EPID image acquisition with interval times less than a minute. The applied methods to accurately derive leaf gap widths from the acquired images are described in section II.E.

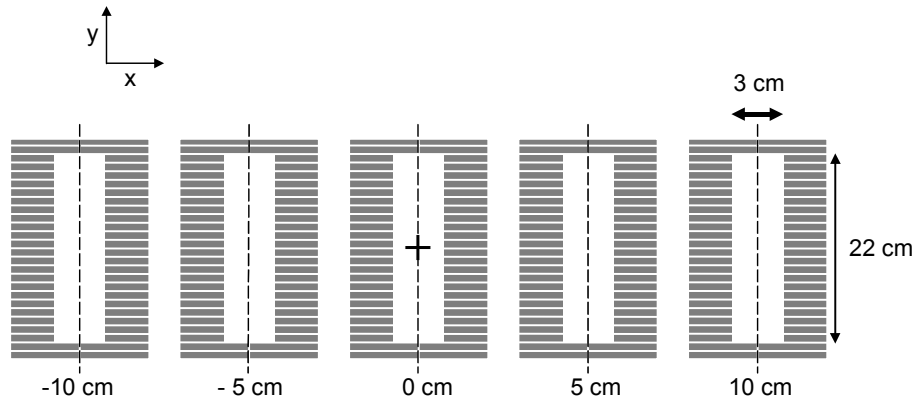


Figure 5-1 SMLC field containing five $3 \times 22 \text{ cm}^2$ segments, centered at positions -10 , -5 , 0 , 5 , 10 cm , respectively. The cross shown at the center of segment 0 cm indicates the isocenter position.

5.3.4.2 Beam output and flatness with small MU

In order to study the beam output and beam flatness for low exposures, a $20 \times 20 \text{ cm}^2$ field was delivered with exposures 1, 2, 6, 10, and 50 MU. EPID images were acquired for each exposure and corrected for dark current only. On-axis EPI values were then calculated as the average value in a central region of $1 \times 1 \text{ cm}^2$ around the beam axis. For beam output analyses, all on-axis pixel values were normalized to the value for the 50 MU field, which represents the accelerator output under stable conditions. To assess beam profile variations, each image was normalized to its corresponding on-axis value.

To measure the short-term reproducibility of the beam output and profile for low exposures, the EPID measurements were repeated 5 times in rapid succession; the long-term reproducibility was derived from repeated measurements over a period of 8 months at the Siemens and Varian accelerator, and 3 months at the Elekta accelerator.

5.3.5 Leaf gap widths in the SMLC field segments

During SMLC field delivery (Fig. 5-1), image frames were continuously acquired and stored separately. In order to reduce the noise level, a few image processing steps were performed. First, the filled frames (beam on) were distinguished from the empty frames (beam off) by calculating the standard deviation over the whole image frames.

A filled frame was considered as such if more than 10% standard deviation was measured. Secondly, for each of the five SMLC segments, only the filled frame showing the highest standard deviation was selected and used for further analyses. Each of the remaining five images was then corrected for dark current, and a median filter was applied to remove isolated high and low pixel values. In the next step, all images were corrected for barrel distortion (see below). Then, for each leaf pair in a beam segment, corresponding grey scale profiles in the x -direction were averaged, resulting in one profile per leaf pair for each beam segment.

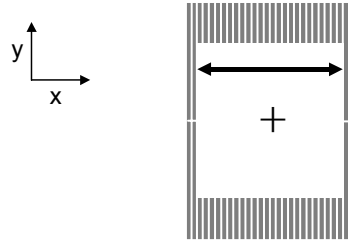


Figure 5-2 Top view of a $24 \times 24 \text{ cm}^2$ MLC field (back-up collimators retracted). Relative to the set-up in Fig. 5-1 there is a collimator rotation of 90° . The arrow indicates the field width as defined by the sides of two leaf pairs.

Only central profiles were chosen for averaging, to avoid the influence of leaf leakage between adjacent leaves. Finally, the gap widths were determined using the 50% grey scale level of each of the profiles and the determined pixel size (see below).

5.3.5.1 Barrel distortion

The barrel image distortion was corrected using ²² :

$$R_{\text{corr}} = R_{\text{ncorr}} (1 + \alpha R_{\text{ncorr}}^2) \quad 5-1$$

where R_{corr} and R_{ncorr} are radial distances (in pixels) in the corrected and in the distorted images, respectively; α is the barrel effect distortion parameter. In this study, the α parameter was derived by acquiring an EPID image of a phantom with inserted markers at known positions in a diagonal. The center for the barrel distortion was determined in an iterative way by applying equation [5-1] to an image for a $24 \times 24 \text{ cm}^2$ static field, fully defined by the MLC (block collimators retracted), for a set of origins. The origin yielding the most constant distance between opposing corrected

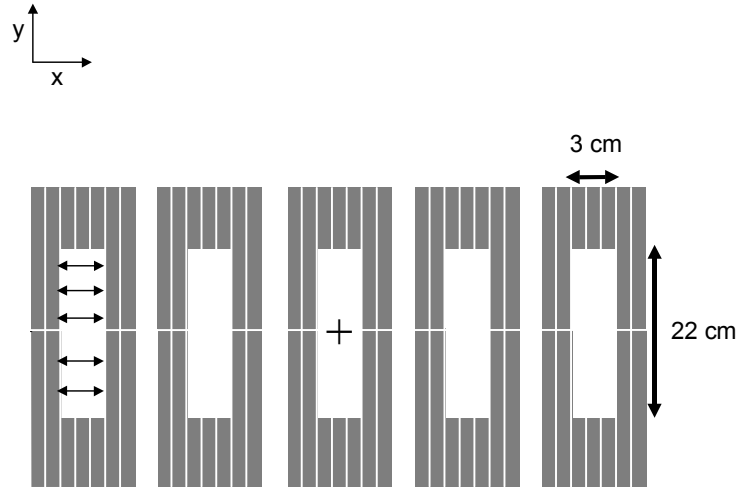


Figure 5-3 SMLC field used to assess the overall accuracy of the method for leaf gap measurement. As in Fig. 5-2, there is a collimator rotation of 90° . The small arrows indicate field widths as determined for several positions along the y -direction.

field edges, defined by the *flat side* of a leaf pair (Fig. 5-2), was selected as the center to be used for the barrel distortion in further analysis. Using the flat side of a leaf pair only makes the procedure independent of leaf positioning inaccuracies. Both the center for the barrel distortion and the α parameter need to be determined once for a specific EPID. Depending on the EPID, barrel distortion corrections of up to 2 mm had to be applied.

5.3.5.2 The pixel size

The pixel size in the x -direction (direction of leaf motion for the SMLC field) was determined using a static $24 \times 24 \text{ cm}^2$ MLC field (block collimators retracted), with a collimator rotation of 90° (Fig. 5-2). In this way the field size in the x -direction was fully defined by the reproducible and accurately known distance between the flat sides of two leaf pairs. After correction for barrel distortion (see above), the 50% grey scale value was used to establish the number of pixels in a distance of 24 cm. For each of the three linacs, the pixel size used for the analysis of all acquired fractions was the average value measured over 10 different days. This was possible because of its high reproducibility of 0.1% (1 SD).

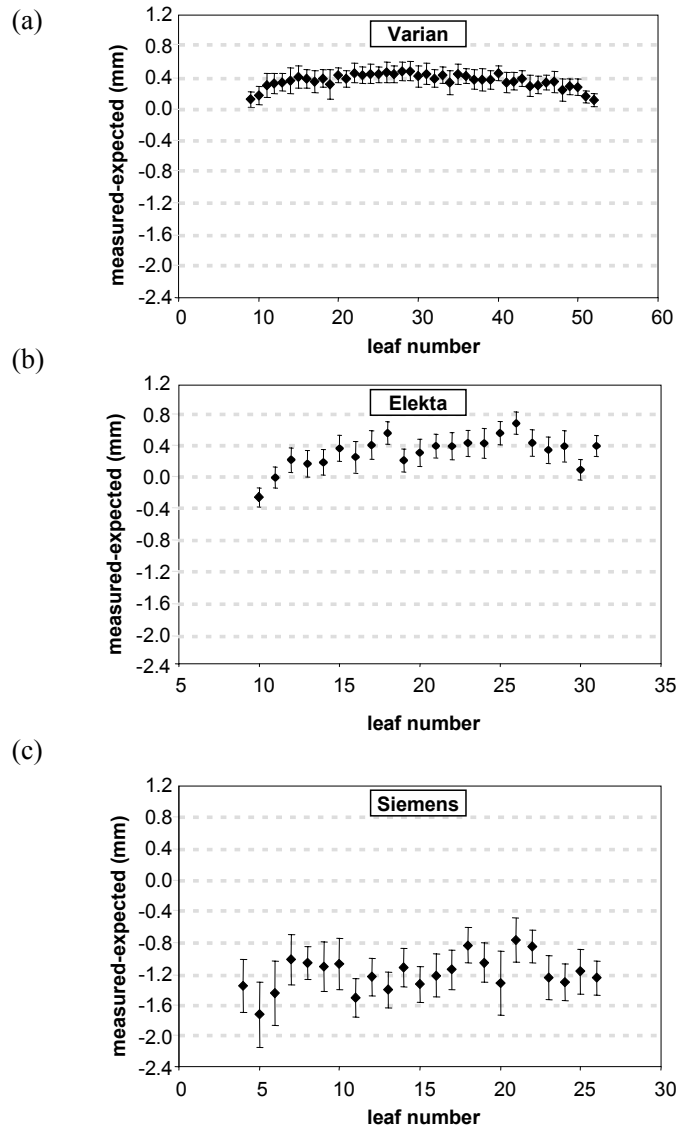


Figure 5-4 Deviations between measured leaf gap widths and the prescribed width of 3 cm. (a), (b) and (c) show the results for the Varian, the Elekta and the Siemens accelerators for beam segments centered at -10 cm, -9 cm, and -10 cm, respectively. The error bars represent the long-term reproducibility in leaf gap widths over the period of the measurements, 8 months for the Varian and the Siemens accelerators, and 3 months for the Elekta accelerator, respectively.

5.4 Results

5.4.1 Accuracy of the method for leaf gap measurement

For the EPID with the largest barrel distortion, the overall accuracy of the algorithm used to determine leaf gap widths was assessed with the five segment MLC field depicted in Fig. 5-3. Relative to the set-up in Fig. 1, the collimator was rotated by 90°. For each of the segments, the gap is fully determined by the (precisely known) reproducible distance between the flat sides of two leaf pairs. Using the procedures described in section II.E, the width of each segment was measured at several y positions (see arrows in Fig. 5-3). The standard deviation describing the observed deviations from the actual width of 3 cm was 0.12 mm. The maximum deviation was 0.23 mm.

5.4.2 Accuracy of leaf positioning

Fig. 5-4 shows for each leaf pair the mean deviation between the measured and prescribed gap width for the Varian, Siemens and Elekta accelerators. The error bars indicate standard deviations for the observations in the period of measurements. The results are shown for one segment center position (-10 cm for the Varian and the Siemens, and -9 cm for the Elekta accelerator). Similar results were found for the other segments. For the Varian and the Siemens accelerators, the observed deviations in leaf gap widths from the prescribed value (3 cm) were 0.36 ± 0.09 mm (1 SD) and -1.21 ± 0.22 mm (1 SD), respectively, over a period of 8 months. For the Elekta accelerator, the deviations in leaf gap were 0.34 ± 0.21 mm (1 SD), over a period of 3 months. These results were averaged over all SMLC field segments. The short-term reproducibility in leaf gap width was 0.04 mm (1 SD), 0.17 mm (1 SD), and 0.12 mm (1 SD), respectively, for the Varian, Elekta, and Siemens accelerators. The time behaviour for individual leaf pairs is shown in Fig. 5-5. For each linac, the data was obtained from the beam segment centered on the isocenter. For all linacs, the hysteresis effects in leaf positioning were smaller than 0.2 mm. An example is given in Fig. 5-6, for the Siemens accelerator.

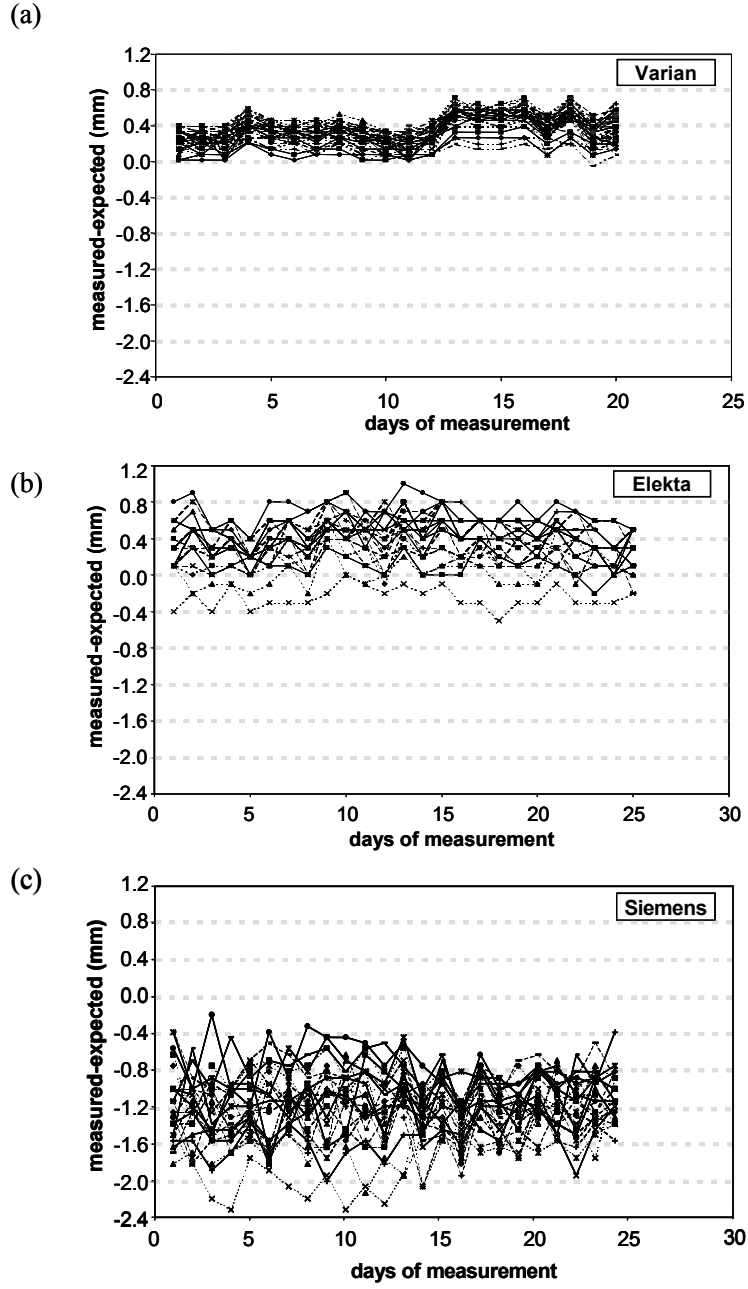


Figure 5-5 Differences between measured leaf gap widths and the prescribed width of 3 cm over the period of measurements (3-8 months). Each line represents an individual leaf pair. The data shown are for the beam segment centered at -10 cm for the Varian linac (a), -9 cm for the Elekta linac (b), and -10 cm for the Siemens linac.

5.4.3 Beam output and flatness with small MU

The beam output at low exposures is shown in Fig. 5-7. The error bars (1 standard deviation) represent the reproducibility over the period of the measurements (i.e., 8 months for the Varian and Siemens accelerators, and 3 months for the Elekta accelerator). For the Elekta and the Siemens linacs (see Fig. 5-7(b) and 5-7(c), respectively), the average beam output was within 4% with respect to the 50 MU exposure. For the Varian accelerator (Fig. 5-7(a)), a larger alinearity of the beam output with low exposures was observed (within 8%). Ionization chamber measurements were performed simultaneously with the EPID measurements for comparison, and showed good agreement (within 2%). Therefore the observed alinearity for low exposures, in particular for the Varian accelerator, is mainly due to the accelerator and not related to the detector used. For exposures of 2 MU and higher, the long-term reproducibility in beam output and beam profile were within 1% (1 SD) for all accelerators. The short-term reproducibility of the measurements was within 1% (1 SD). The 1 MU measurement was clearly less stable than the other exposures with a long-term reproducibility within 4% (1 SD), for the Siemens accelerator, and within 2% (1 SD) for the Varian and Elekta accelerators, respectively. The short-term reproducibility for this exposure was 2% (1 SD), for all accelerators.

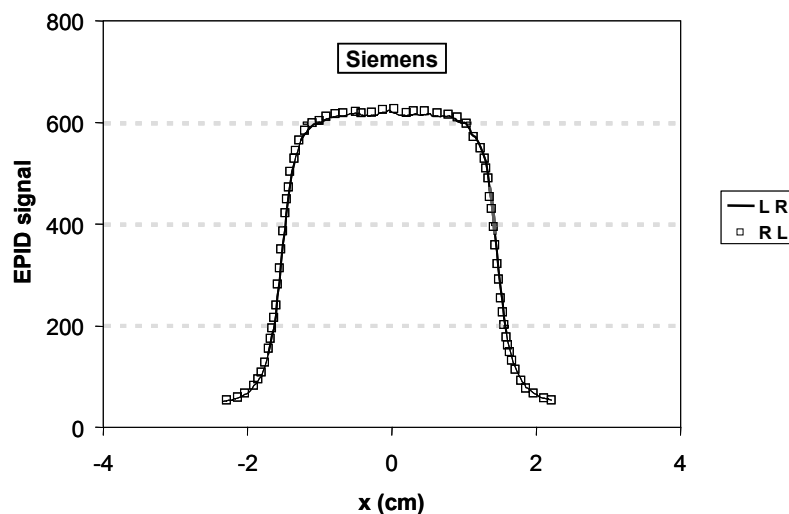


Figure 5-6 Comparison of EPID profiles measured at the Siemens accelerator for a SMLC delivery from left to right (line) and right to left (squares). The SMLC segment shown was centered at 0 cm.

5.5 Discussion

Dedicated tools are needed for fast and effective linac QA for SMLC. Quality control tests have to include leaf positioning verification and stability in beam output and beam profile for low exposure fields. Causes of deviations in leaf positioning relative to prescription may be dependent on the MLC configuration, and on the applied calibration methods. For the Elekta MLC, deviations may arise due to thermal effects in a radiation damaged camera used to calibrate the leaves, changes in the optical system, and stability of the mirror and lens components.^{23,24} For the Varian MLC, changes in leaf position can be attributed to the infra-red laser stability and the leaf motors. The latter also holds for the Siemens MLC.

The measurements in Fig. 5-4 show very small long-term variations in leaf gap widths for all accelerators (0.09-0.22 mm, 1 SD). For the Varian linac there is a strong correlation between the observed day-to-day variations in the measured gap widths for the various leaf pairs (Fig 5-5a). This is probably related to the applied optical system that is used for daily calibration of all leaves (section II.B). The systematic deviations in leaf gap widths measured in this study varied from -1.21 mm to 0.36 mm. The relatively large mean deviation for the Siemens linac (-1.21 mm) may be related to the applied leaf calibration procedure using the light field (section II.B). Prior to the calibration at the latter accelerator, a film was irradiated to check the light field-X-ray field coincidence, but a visual inspection was performed only and differences up to ± 1 mm are considered within linac specifications. In this study, the leaf gap width was determined using the EPID, and reflect the leaf gap width as derived with the X-ray field. Therefore, the systematic difference in leaf gap width mentioned above may be due to the non-coincidence of the light and the X-ray field.

The results from our study showed a linearity of beam output for low exposures within 4%, for the Siemens and the Elekta accelerator (see Fig.5-7(b) and 5-7(c)). Similar findings were previously reported.²⁻⁴ The alinearity of beam output with low exposures was larger for the Varian accelerator (see Fig. 5-7(a)). This is due to the fact that,

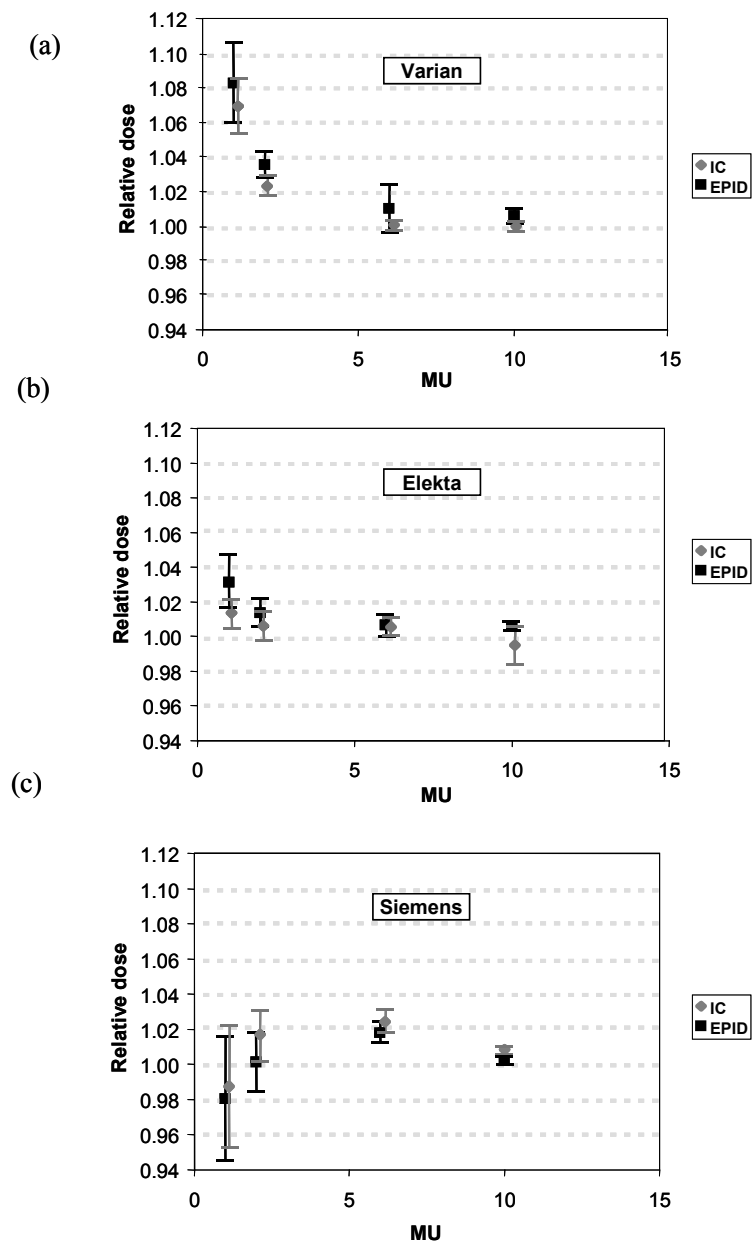


Figure 5-7 Ratios of on-axis pixel values measured with the EPID and the corresponding exposures (MU) delivered by the linac (squares). The ratio is normalized to 1 for a 50 MU exposure. The diamonds represent ionization chamber (IC) measurements.

in contrast to the Elekta or the Siemens accelerators, the linearity of the beam output can not be tuned for the Varian accelerators.

Based on the results of our study, we have decided on a SMLC QA test for daily routine use (Fig. 5-8). This test has two main components: (1) a low exposure at about 5 MU, and a 50 MU $20 \times 20 \text{ cm}^2$ MLC field (Fig. 5-8a), and (2), a SMLC field with five $3 \times 22 \text{ cm}^2$ segments, centered around several x positions, and delivered with an exposure of 10 MU each (Fig. 5-8b).

The two $20 \times 20 \text{ cm}^2$ MLC fields in component (1) are used to analyze the beam output and profile at low exposures, to assess the pixel size, and to daily verify the isocenter

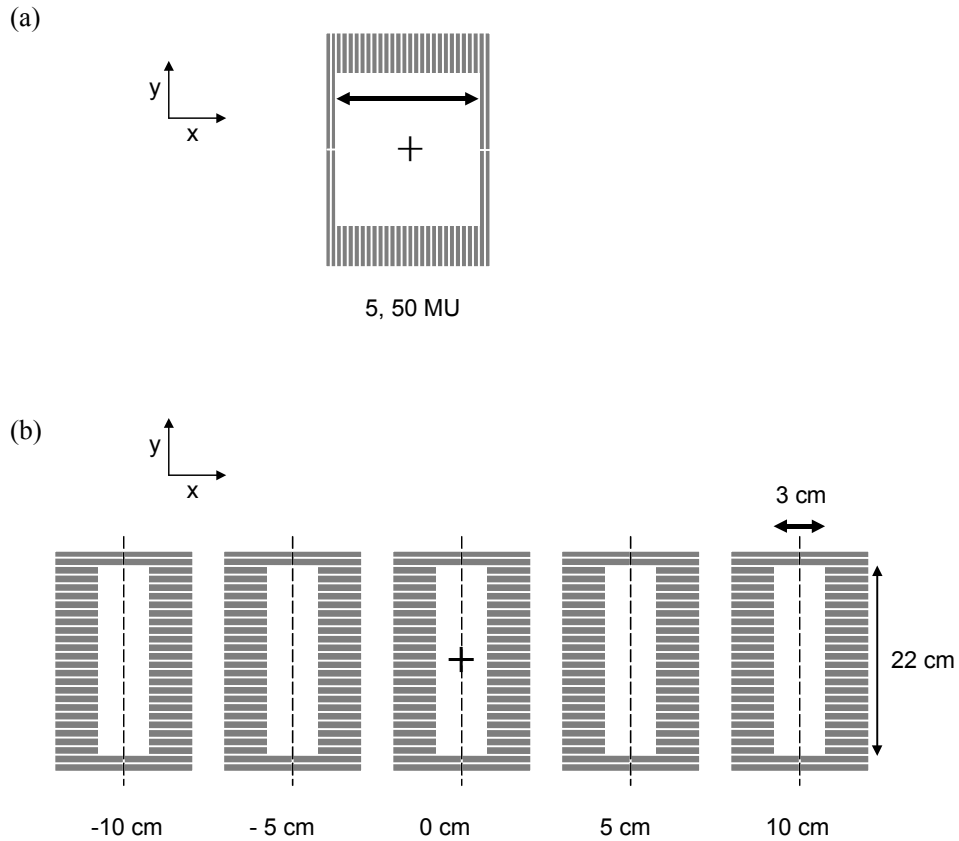


Figure 5-8 QA test for SMLC: (a) a $20 \times 20 \text{ cm}^2$ MLC field, rotated by 90° , and irradiated with a low MU exposure and with 50 MU. (b) SMLC field with five $3 \times 22 \text{ cm}^2$ segments centered at positions -10, 5, 0, 5, 10 cm.

position. Although this study included exposures as low as 1 MU (section II.D), there is often a constraint on the minimum allowed MU for each segment in clinical practice (e.g., 4-5 MU). For this reason, a 5 MU exposure is nowadays used in our daily QA test. To accurately determine the isocenter in the EPID images, and the pixel size in the direction of leaf motion, the $20 \times 20 \text{ cm}^2$ fields in step (1) are delivered with a collimator angle of 90° (Fig 5-8a). In the x-direction, the fields are then defined by the known positions of the sides of two leaf pairs, as illustrated by the arrow in Fig. 5-8(a)). Using a previously determined ratio between the pixel sizes in the x- and y-directions, it is then possible to also derive the pixel size in the y direction. Knowing both the isocenter and the pixel size, the absolute position of the leaves can be calculated with respect to the isocenter position.

The measurement of component (2) is aimed at checking the leaf position stability under SMLC delivery. As hysteresis effects in leaf positioning were practically absent in this study, our daily QA test does not check for hysteresis. Such checks may be done on a monthly basis using the methods described in section II.

In a SMLC treatment, the block collimators for the y-direction are generally used to define the lengths of beam segments. Therefore, the QA procedure for SMLC will be extended with a SMLC field consisting of five $22 \times 3 \text{ cm}^2$ segments, centered at different positions along the y-direction.

The time required to perform QA tests for SMLC delivery is rarely stated in the literature. Hounsell *et al.*²³ concluded that 30 min of QA time was needed per month for the Elekta MLC. To provide the position of each leaf for 11 different locations, Bayouth *et al.*⁵ needed 5 minutes for data acquisition using an auto-field sequencing and approximately 30 minutes for film analysis. The test reported in this paper is performed in about 3-4 minutes (including the acquisition and the automated analysis of the EPID images), and is therefore suited for daily routine QA.

5.6 Conclusions

A procedure for daily, fast and accurate QA of SMLC dose delivery has been developed and evaluated for Elekta, Siemens and Varian linacs at two institutions. The method is nowadays in routine clinical use.

5.7 Acknowledgments

The authors would like to thank Carmen Panneman for her contribution to the measurements, Martijn Laarhoven, Hans Groen, and Peter de Graaff for their explanation of the MLC calibration procedure, and Hans de Boer for the fruitful discussion. This work was supported by the ‘Fundação para a Ciência e a Tecnologia’.

5.8 References

- ¹D. A. Low, J. W. Sohn, E. E. Klein, J. Markman, S. Mutic, and J. F. Dempsey, "Characterization of a commercial multileaf collimator used for intensity modulated radiation therapy," *Med. Phys.* **28**, 752-6 (2001).
- ²C. W. Cheng and I. J. Das, "Comparison of beam characteristics in intensity modulated radiation therapy (IMRT) and those under normal treatment condition," *Med. Phys.* **29**, 226-30 (2002).
- ³V. N. Hansen, P. M. Evans, G. J. Budgell, J. H. Mott, P. C. Williams, M. J. Brugmans, F. W. Wittkamper, B. J. Mijnheer, and K. Brown, "Quality assurance of the dose delivered by small radiation segments," *Phys. Med. Biol.* **43**, 2665-75 (1998).
- ⁴M. B. Sharpe, B. M. Miller, D. Yan, and J. W. Wong, "Monitor unit settings for intensity modulated beams delivered using a step-and-shoot approach," *Med. Phys.* **27**, 2719-25 (2000).
- ⁵J. E. Bayouth, D. Wendt, and S. M. Morrill, "MLC quality assurance techniques for IMRT applications," *Med. Phys.* **30**, 743-50 (2003).
- ⁶G. A. Ezzell, J. M. Galvin, D. A. Low, J. R. Palta, I. Rosen, M. B. Sharpe, P. Xia, Y. Xiao, L. Xing, and C. X. Yu, "IMRT subcommittee; AAPM Radiation Therapy committee. Guidance document on delivery, treatment planning, and clinical implementation of IMRT: report of the IMRT Subcommittee of the AAPM Radiation Therapy Committee," *Med. Phys.* **30**, 2089-115 (2003).
- ⁷M. N. Graves, A. V. Thompson, M. K. Martel, D. L. McShan, and B. A. Fraass, "Calibration and quality assurance for rounded leaf-end MLC systems," *Med. Phys.* **28**, 2227-33 (2001).
- ⁸M. Sastre-Padro, U. A. van der Heide, and H. Welleweerd, "An accurate calibration method of the multileaf collimator valid for conformal and intensity modulated radiation treatments," *Phys. Med. Biol.* **49**, 2631-43 (2004).
- ⁹C. B. Saw, K. M. Ayyangar, W. Zhen, R. B. Thompson, and C. A. Enke, "Commissioning and quality assurance for MLC-based IMRT," *Med. Dosim.* **26**, 125-33 (2001).
- ¹⁰S. S. Samant, W. Zheng, N. A. Parra, J. Chandler, A. Gopal, J. Wu, J. Jain, Y. Zhu, and M. Sontag, "Verification of multileaf collimator leaf positions using an electronic portal imaging device," *Med. Phys.* **29**, 2900-12 (2002).
- ¹¹Y. Yang, and L. Xing, "Quantitative measurement of MLC leaf displacements using an electronic portal image device," *Phys. Med. Biol.* **49**, 1521-33 (2004).
- ¹²H. C. de Boer and B. J. M. Heijmen, "A protocol for the reduction of systematic patient set-up errors with minimal portal imaging workload," *Int. J. Rad. Oncol. Biol. Phys.* **50**, 1350-65 (2001).
- ¹³H. C. de Boer, J. R. van Sornsens de Koste, S. Senan, A. G. Visser, and B. J. M. Heijmen, "Analysis and reduction of 3D systematic and random set-up errors during the simulation and treatment of

- lung cancer patients with CT-based external beam radiotherapy dose planning," *Int. J. Rad. Oncol. Biol. Phys.* **49**, 857-68 (2001).
- ¹⁴H. C. de Boer, J. R. van Sornsens de Koste, C. L. Creutzberg, A. G. Visser, P. C. Levendag, B. J. M. Heijmen, "Electronic portal image assisted reduction of systematic set-up errors in head and neck irradiation," *Radiother. Oncol.* **61**, 299-308 (2001).
- ¹⁵E. N. van Lin, L. van der Vicht, H. Huizenga, J. H. Kaanders, and A. G. Visser, "Set-up improvement in head and neck radiotherapy using a 3D off-line EPID-based correction protocol and a customised head and neck support," *Radiother. Oncol.* **68**, 137-48 (2003).
- ¹⁶J. C. Stroom, M. Kroonwijk, K. L. Pasma, P. C. M. Koper, E. B. Dieren, and B. J. M. Heijmen, "Detection of internal organ movement in prostate cancer patients using portal images," *Med. Phys.* **27**, 452-61 (2000).
- ¹⁷M. Kroonwijk, K. L. Pasma, S. Quint, P. C. M. Koper, A. G. Visser, and B. J. M. Heijmen, "In vivo dosimetry for prostate cancer patients using an electronic portal imaging device (EPID): detection of internal organ motion," *Radiother. Oncol.* **49**, 125-32 (1998).
- ¹⁸K. L. Pasma, M. L. P. Dirkx, M. Kroonwijk, A. G. Visser, and B. J. M. Heijmen, "Dosimetric verification of intensity modulated beams produced with dynamic multileaf collimation using an electronic portal imaging device," *Med. Phys.* **26**, 2373-78 (1999).
- ¹⁹K. L. Pasma, M. Kroonwijk, S. Quint, A. G. Visser, and B. J. M. Heijmen, "Transit dosimetry with an electronic portal imaging device (EPID) for 115 prostate cancer patient," *Int. J. Rad. Oncol. Biol. Phys.* **45**, 1297-03 (1999).
- ²⁰S. C. Vieira, M. L. P. Dirkx, K. L. Pasma, and B. J. M. Heijmen, "Fast and accurate leaf verification for dynamic multileaf collimation using an electronic portal imaging device," *Med. Phys.* **29**, 2034-40 (2002).
- ²¹E. M. Franken, J. C. J. de Boer, J. C. Barnhoorn, and B. J. M. Heijmen, "Characteristics relevant to portal dosimetry of a cooled CCD camera-based EPID," *Med. Phys.* **31**, 2549-51 (2004).
- ²²L. W. Casperson, P. Spiegler, and J. H. Grollman, Jr., "Characterization of aberrations in image-intensified fluoroscopy," *Med. Phys.* **3**, 103-6 (1976).
- ²³A. R. Hounsell and T. J. Jordan, "Quality control aspects of the Elekta multileaf collimator," *Radiother Oncol.* **45**, 225-33 (1997).
- ²⁴T. J. Jordan and P. C. Williams, "Quality control aspects of the Elekta multileaf collimator," *Phys. Med. Biol.* **39**, 231-51 (1994).

CHAPTER 6. TWO-DIMENSIONAL MEASUREMENT OF PHOTON BEAM ATTENUATION BY THE TREATMENT COUCH AND IMMOBILIZATION DEVICES USING AN ELECTRONIC PORTAL IMAGING DEVICE

S C Vieira, R S J P Kaatee, M L P Dirkx, B J M Heijmen

Med. Phys. **30**, 2981-2987, 2003

6.1 Abstract

In our institution, an individualised dosimetric quality assurance protocol for intensity modulated radiotherapy (IMRT) is being implemented. This protocol includes dosimetric measurements with a fluoroscopic electronic portal imaging device (EPID) for all IMRT fields while the patient is being irradiated. For some of the first patients enrolled in this protocol, significant beam attenuation by (carbon fiber) components of the treatment couch was observed. To study this beam attenuation in 2D, EPID images were also acquired in absence of the patient, both with and without treatment couch and immobilization devices, as positioned during treatment. For treatments of head and neck cancer patients with a 6 MV photon beam, attenuation of up to 15% was detected. These findings led to the development of new tools and procedures for planning and treatment delivery to avoid underdosages in the tumor.

6.2 Introduction

An adequate dosimetric quality assurance (QA) program is indispensable for safe dose delivery in radiotherapy, especially for more complex techniques like intensity modulated radiotherapy (IMRT). The ultimate goal of such a program is to ensure for each individual patient that the 3-dimensional (3D) dose distribution, as approved by the physician, is indeed delivered to the patient. A fundamental practical problem is that one cannot directly measure the delivered 3D dose distribution inside the patient. Therefore, indirect means have to be used to confirm appropriate dose delivery. In our institution, we try to do this by answering three groups of questions: *I*. Are the results

of the treatment planning process reliable?, *II*. Are the linac related parameters (gantry angles, leaf trajectories for IMRT, cGy/MU of the linac in reference conditions, etc.) as established and used in the treatment planning system (TPS) indeed realized during execution?, and *III*. Are the patient related parameters during treatment execution in agreement with the parameters as assumed for treatment planning? This last question can be separated into two parts: 1.) Is the set-up of the patient at the linear accelerator relative to the linac isocenter identical to the one in the TPS? 2.) Does the (internal) patient anatomy during treatment agree with the planning CT-scan?

Based on our own experiences and on those reported by others,¹⁻⁴ we are developing and implementing a quality assurance program to answer the questions *I-III*, for each IMRT patient. To answer question *I*, (fully automated) procedures are currently being implemented to perform for each patient a fully independent 3D forward dose calculation, using a second (commercial) TPS with the plan parameters established with the first system as input. This procedure should become the 3D equivalent of the widely applied independent MU check for static beams. Dosimetric measurements with our electronic portal imaging devices (EPID) are used to verify correct realization by the linac of the planned IMRT fields⁵⁻⁷ (question *II* above). The latter procedure includes *pre-treatment* measurements, i.e., prior to the first treatment fraction in absence of the patient.⁶ In addition to the verification of the linac performance, EPID-images acquired during treatment delivery are also used to verify and correct the patient set-up relative to the linac isocenter⁸⁻¹² (question *III.1*), and to verify the (internal) patient anatomy^{7,13} (*III.2*). Apart from the procedures mentioned above, no other individualised verification, e.g., based on phantom measurements with film or ionization chamber, or “in-vivo” measurements with diodes, is performed. The described individualised dosimetric procedures are complemented with a fast, daily verification of the linac performance for dynamic multileaf collimation, which is not tailored to the profiles of individual patients.¹⁴

For some of the first patients enrolled in the dosimetric QA protocol, significant beam attenuation by (carbon fiber) components of the treatment couch was observed in EPID images acquired during treatment, which prevented accurate dosimetric verification of these treatment beams. For the posterior beams, the beam attenuation affects the dose delivery to the patient, yielding lower doses than expected. Because in IMRT posterior oblique angles of incidence are frequently used, this might be a serious problem. To be able to quantify the beam attenuation by the treatment couch and the immobilization devices in 2D for clinical configurations, additional EPID measurements have been performed in the absence of the patient. In this paper, results

of these measurements are shown as well as some examples of beam attenuation during the treatment of IMRT head and neck cancer patients and of lung cancer patients treated with static (i.e., non-IMRT) fields in a study protocol. Validation of the EPID measurements using an ionization chamber is reported. Measures to avoid beam attenuation, yielding underdosages in the patients, are proposed.

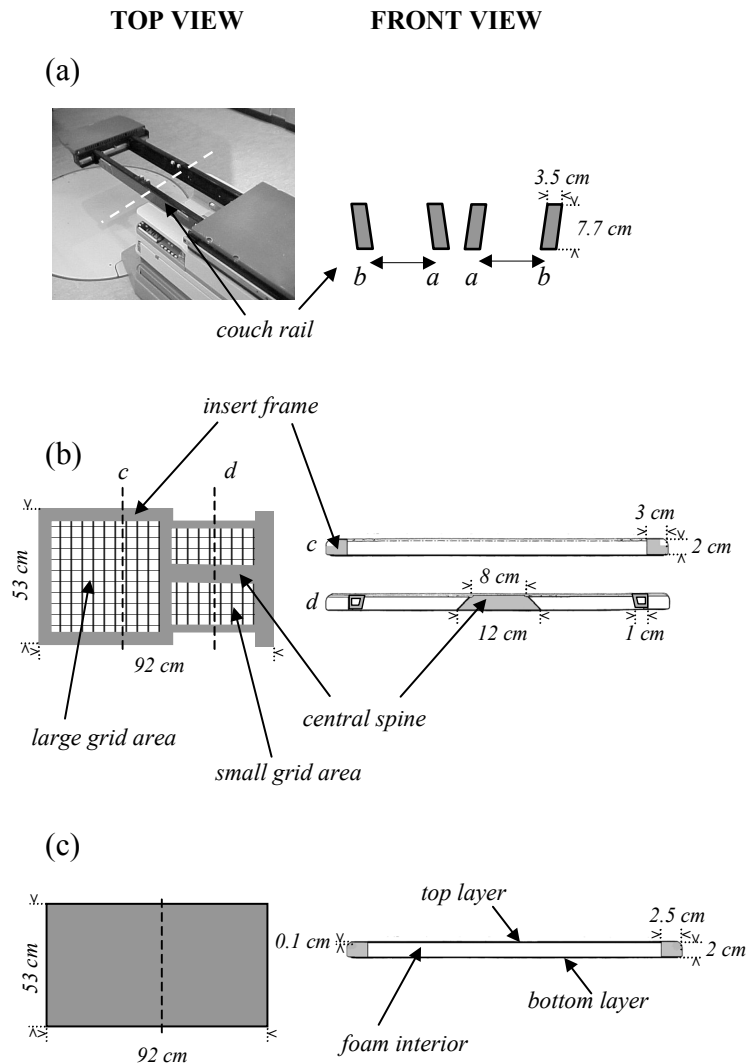


Figure 6-1 Top and front view of the treatment couch. (a) The couch rails, which can move from a to b, the most central and outermost positions, respectively. (b) The grid couch insert with two cross-sections c and d, and (c) the solid couch insert.

6.3 Materials and Methods

6.3.1 Treatment couch and immobilization devices

All measurements have been performed at a Clinac 2300 C/D accelerator (Varian Oncology Systems, USA), connected to the Multi-ACCESS (IMPAC Medical Systems, USA) record and verify system. The treatment unit is equipped with an *Exact* treatment couch (Varian Oncology Systems, USA), having two translatable rails and a couch insert, all made from carbon fiber [Fig. 6-1(a)]. Each couch rail may be placed at any position in between the center and the outmost side position in order to avoid intersection with the treatment beam. The standard carbon fiber couch insert lies on top of the treatment couch and has a large grid area on one side,

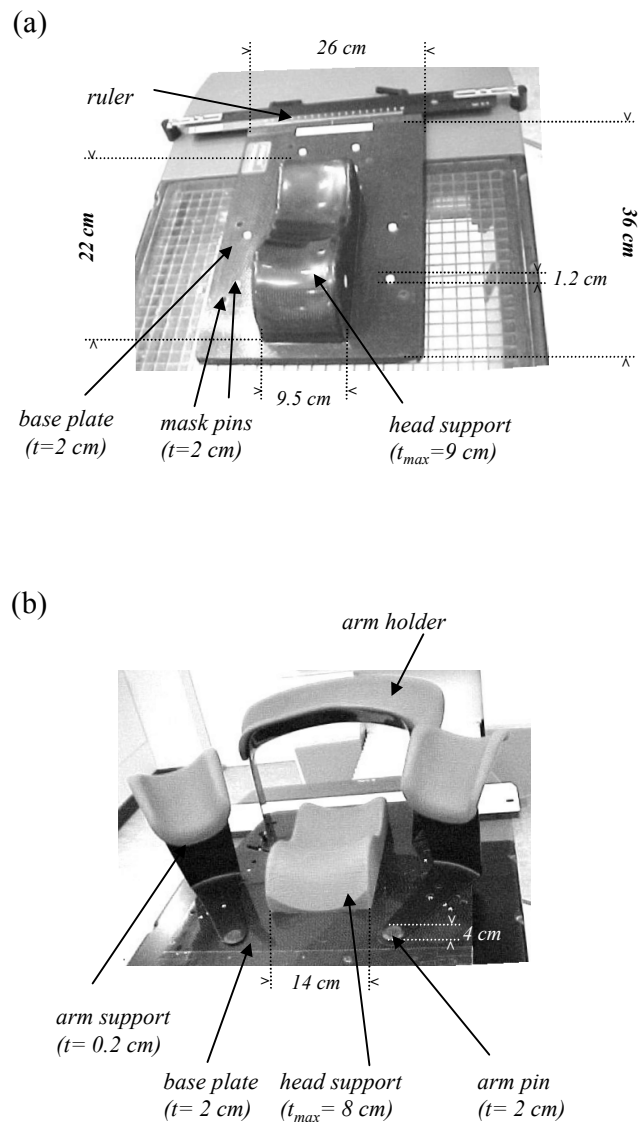


Figure 6-2 Immobilization devices used for fixation of (a) head and neck cancer patients and (b) lung cancer patients. The physical dimensions of the devices are also mentioned. t and t_{\max} indicate the thickness and the maximal thickness, respectively.

and a *central spine* with two smaller grid areas on the other [Fig. 6-1(b)]. The insert frame is solid on the side of the larger grid area and hollow on the central spine side (see cross-section *c* and *d* in Fig. 6-1(b)). A 0.4 mm thick mylar sheet covers the couch insert for patient comfort. Depending on the tumor site and the beam orientations used for the treatment, two positions of the couch insert can be used: one with the large grid area to the gantry side, and the other 180° rotated. Instead of the above mentioned “grid” couch insert, also a solid one (MED-TEC, Orange City, USA) can be used [Fig. 6-1(c)] to reduce sagging.¹⁵ This couch insert is made from two layers of carbon fiber (2 mm thick) with a foam material in between.

The immobilization devices (Sinmed BV, Reewijk, The Netherlands) used for the head and neck and the lung cancer treatments are illustrated in Figs. 6-2a and 6-2b, respectively. The head and neck cancer patients lay on a carbon fiber head support, which is placed in the center of a carbon fiber base plate (*Posifix-4*). The mask of the patient is attached to the base plate using plastic pins. The base plate may be displaced laterally relative to the center of the treatment couch using a ruler as reference. The most extreme points of the ruler are fixed to the treatment couch. Lung patients rest on a lung board (*Posirest-2*). The board consists of a carbon fiber base plate with a polyurethane foam head support. The patient arms are positioned cranially using an arm holder

	Electron density (g cm ⁻³)
Grid insert:	
central spine	1.1
frame (central spine side)	1.1
frame (large grid area side)	1.2
Solid insert:	
top layer	0.4
foam interior	0.2
bottom layer	0.6
Head and neck device:	
head support	0.1
mask pins	1.1
base plate (foam interior)	0.1
base plate (0.1 cm outer layer)	0.4
Lung device:	
head support	0.1
arm pin	1.2
base plate (foam interior)	0.1
base plate (0.1 cm outer layer)	0.4
arm support	1.5

Table 6-1 Electron density of the components of the treatment couch and immobilization devices.

combined with two upper arm supports. Each arm support, as well as the arm holder, may be adjusted to several positions.

The electron density of both the treatment couch components and the immobilization devices, as derived after scanning at a PQ5000 CT-scanner (Marconi, USA), are shown in Table 6-1.

6.3.2 The EPID

A fluoroscopic Theraview NT EPID (Cablon Medical, Leusden, The Netherlands), low elbow type, has been used for portal imaging. This CCD-camera based system has 3 characteristics most relevant for dosimetric applications, and for dynamic multileaf collimation (DMLC) in particular: (i) an excellent short and long term stability, (ii) the signal is integrated simultaneously in all 1024×1024 pixels (frame integration time of 800 ms), and (iii) the dead time in between acquisition of subsequent frames is only 2 ms.¹⁶

Calibration of the EPID is based on 2D ionization chamber measurements performed at 1 cm depth in a polystyrene mini-phantom with a transversal cross section of 7×7 cm² and a thickness of 5 cm.⁵ The center of the ionization chamber is positioned at a distance of 170 cm from the focus, which is equal to the focus-to-fluorescent screen distance of our EPID. At 1 cm depth, minimal variations in the on-axis response of the EPID relative to the ionization chamber readings are observed beneath flat polystyrene phantoms, positioned on the treatment couch, with thicknesses ranging from 0 up to 35 cm, for field sizes ranging from 3×3 cm² to 22×22 cm². For these measurements a 60 cm air gap is used between the phantoms and the mini-phantom or the EPID. From the measurements, performed only once, corrections for the non linearity of the EPID response, for the optical scatter (also called “crosstalk”) inside the EPID structure, and for variations in the relative EPID sensitivity are derived, as explained in detail elsewhere.^{5,16}

Prior to further analysis, each image acquired during this study was first converted into a portal dose image (PDI), i.e., a dose distribution in the plane of the fluorescent screen, by applying the corrections described above.⁵ The resulting PDIs are proportional to dose.

6.3.3 EPID measurements during patient treatment

All 17 patients in this study were treated with 6 MV photon beams. EPID images were acquired during each patient treatment fraction with the EPID placed at a source-to-detector-distance of 170 cm. The corresponding images obtained during the different fractions were mutually compared.

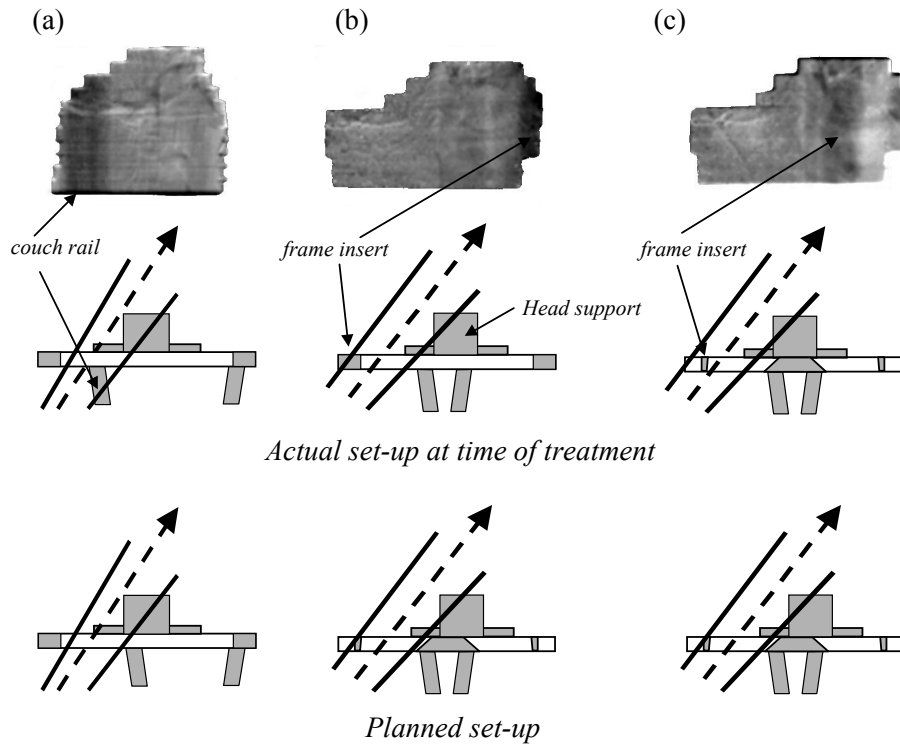


Figure 6-3 Upper panel: ratio between EPID images acquired during some IMRT treatment fractions and the corresponding image obtained in the first fraction for two head and neck cancer patients. (b) and (c) relate to a particular beam of the same patient during two different treatment fractions. Middle panel: actual set-ups of the treatment couch and head and neck immobilization device at the time of treatment execution. Lower panel: intended set-ups of the treatment couch and head and neck immobilization device.

6.3.4 Assessment of the attenuation by the treatment couch and immobilization devices

Triggered by observed day-to-day variations in the “in-vivo” dosimetry measurements (Sec. II C.), beam attenuation (i.e., reduction of the primary fluence) by the couch and immobilization devices was investigated in more detail for the applied posterior (oblique) beams at the same source-to-detector-distance (170 cm). For this purpose, EPID images of the clinical beams were acquired, *in absence* of the patient, both with and without immobilization devices and treatment couch, as positioned during treatment. 2D transmission images were derived as the ratio of both images. In order to explain some deviations observed in the EPID images acquired during patient treatment, additional measurements, with treatment couch positions deviating from the intended setting were made.

6.3.5 Validation of the EPID measurements

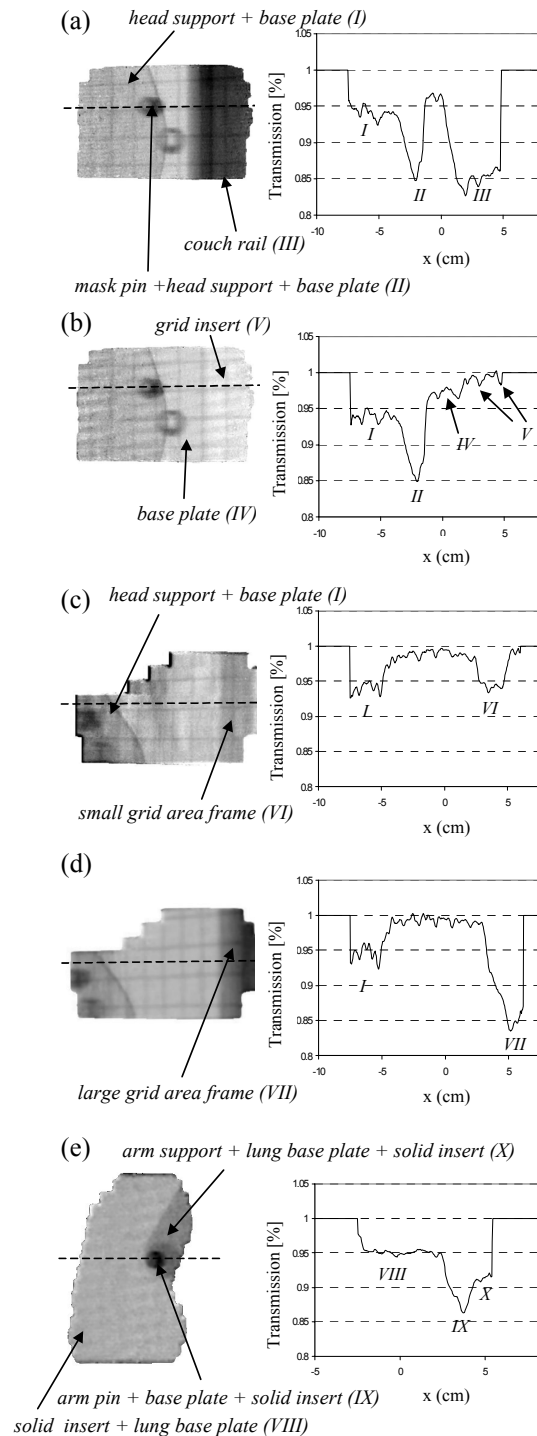
Ionization chamber measurements were performed to confirm the EPID beam attenuation measurements. A NE 2571 ionization chamber was placed in a $30 \times 30 \times 10 \text{ cm}^2$ polystyrene phantom at a depth of 1 cm, which is the equivalent depth of this EPID.⁵ The ionization chamber was positioned at the same distance from the focus as the EPID (170 cm). Attenuation of a 6 MV beam by the head and neck immobilization device base plate [Fig. 6-2(a)], the solid couch insert [Fig. 6-1(c)], and a stack of polystyrene plates, all placed at the isocenter level, was measured using the EPID and the ionization chamber. Each $30 \times 30 \text{ cm}^2$ polystyrene plate was 1 cm thick. The total thickness of the polystyrene stack ranged from 1 cm to 4 cm and was chosen in order to achieve similar beam attenuation as observed from the treatment couch and the immobilization devices. The head and neck immobilization device and the polystyrene plates were supported by the couch rails only (i.e., the couch insert was removed and the couch rails were positioned outside the treatment field). These measurements were performed at the beam axis of a $6 \times 6 \text{ cm}^2$ field for normal incidence. The EPID values were calculated as the average over a central region of $0.8 \times 0.8 \text{ cm}^2$, in order to minimize the effects of noise. A $6 \times 6 \text{ cm}^2$ field was selected to minimize the amount of scattered radiation.

6.4 Results

6.4.1 EPID measurements during patient treatment

For a number of patients, the ratio between the measured portal dose image and the corresponding image obtained in the first treatment fraction exhibited regular “stripes” in some treatment fractions [Fig. 6-3]. These variations in pixel value could neither be attributed to a change in anatomical structures because of its too regular shape, nor to variations in the fluence profiles

Figure 6-4 Beam attenuation by the treatment couch and the head and neck immobilization device ((a)-(d)), and the immobilization device for lung cancer patients (e). (a) and (b), transmission image of the IMRT field with and without couch rail in the beam. (c) and (d), transmission image of the IMRT field for both orientations of the couch insert. (e), transmission image of the solid couch insert and the immobilization device used for the lung cancer patients. The presented 2D images are the ratio of an EPID image acquired with and without treatment couch and immobilization device in the beam.



delivered by the treatment unit. Further investigations based on EPID measurements without the patient in the beam (as explained in detail in the next section) allowed interpreting these stripes as occasional couch configuration errors related to the couch rail or the couch insert. In Fig. 6-3(a), a vertical dark stripe is observed, due to the fact that the couch rail was not completely moved to its inmost central position, causing an occasional beam attenuation of about 15%. In Fig. 6-3(b), the couch insert was placed in the reverse orientation as the one planned, leading to a beam attenuation of about 10% caused by the insert frame. For this particular treatment beam, intersection with the couch insert frame was unavoidable, even if the couch insert would have been used as planned, resulting in a systematic attenuation of about 5% (see next section). As is clear from the planned set-up for Fig. 6-3(c) (lower panel), there was an intersection of the treatment beam with the couch at the field border. On one day, due to an incorrect position of the patient relative to the couch (but correct position regarding to the isocenter, compare middle and lower panels), the couch intersection moved towards the central part of the field, leading to a dark and light stripe (5%).

If attenuation by the treatment couch rails or insert was detected with the EPID, the right position of these components was indicated explicitly in the patient chart. As a result, couch position errors did not occur more than twice for each patient along the whole treatment (typically 25 fractions). Although an occasional couch configuration error is a “random” error, which happens seldom during the course of the treatment, in reality it always leads to underdosages in the patient for posterior

	Beam attenuation (%)	
	EPID	Ion. chamber
Head and neck device:		
base plate (below head support)	0.3	0.4
base plate (lateral area)	1.1	0.8
Solid couch insert	3.2	3.0
Thickness of the polystyrene stack:		
1 cm	6.0	4.8
2 cm	9.9	9.8
3 cm	15.3	14.5
4 cm	21.0	18.7

Table 6-2 Comparison of the beam attenuation for several materials derived from ionization chamber and EPID measurements.

fields, i.e., this “random” error has actually a “systematic” impact on the dose distribution.

6.4.2 Assessment of the attenuation by the treatment couch and immobilization devices

For one particular IMRT treatment field (gantry angle 215°), transmission images, defined as the ratio between PDIs derived from EPID images acquired with and without treatment couch and immobilization devices in the beam, are shown in Figs. 6-4(a) and 6-4(b), for two positions of the left couch rail. The darker areas in the images indicate regions where beam absorption by the treatment couch and immobilization devices occurs. With the couch rail at the most lateral position, the beam attenuation is about 15% [Fig. 6-4(a)]. For the head and neck immobilization device, the carbon fiber base plate, the carbon fiber head support, and the pin used to attach the mask (illustrated in Fig. 6-2(a)) attenuate the beam by about 3%, 3% and 10% respectively [Figs. 6-4(a)-6-4(d)]. These numbers demonstrate that in clinical situations the attenuation of the immobilization devices may be significantly larger than the typical values supplied by the manufacturer ($< 1\%$), which are apparently provided through the thin section of the devices and for normal incidence only.

For another clinical treatment field (gantry angle 230°), transmission images were derived for the two possible orientations of the couch insert [Fig. 6-1(b)]. In both situations beam attenuation by the couch insert frame is observed. In case the large grid area is oriented towards the gantry, the attenuation by the insert frame is about 15% [Fig. 6-4(d)]. If the couch insert is rotated 180° , the beam attenuation is reduced to 5% [Fig. 6-4(c)] because this part of the insert is hollow (see Fig. 6-1(b)).

Fig. 6-4(e) shows the transmission image for the treatment field of a particular lung cancer patient (gantry angle 210°). For the lung immobilization device, attenuation of almost 5% and 10% was observed for the arm support and for the pin used to attach the arm support to the base plate, respectively. For this patient, the solid carbon fiber couch insert [Fig 6-1(c)] was used, which, together with the lung base plate, attenuates the beam by about 5%.

The results in this section show that, in addition to the occasional errors observed in the “in-vivo” dosimetry measurements, systematic errors may be present due to the beam attenuation of the treatment couch and immobilization devices. Mutual com-

parison of EPID images, as described in the previous section, does not allow detection of these systematic errors.

6.4.3 Validation of the EPID measurements

In table 6-2, the beam attenuation by the head and neck base plate, the solid couch insert, and the polystyrene plates as derived from EPID and ionization chamber measurements is shown. The similarity of these results show the usefulness of the EPID to assess beam attenuation. As opposed to the point measurements performed with an ionization chamber, the attenuation is simultaneously measured in 2D and can easily be evaluated for any beam orientation.

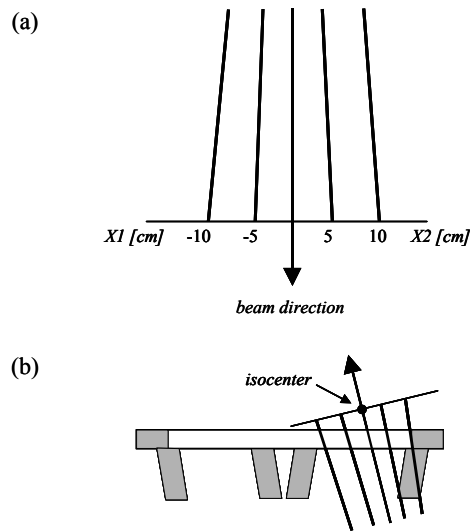


Figure 6-5 Graphical tool to visualize possible intersection of a treatment beam with the treatment couch. A transparent sheet containing a range of field sizes $X1$ and $X2$ (a), is placed on top of a paper sheet showing the treatment couch configuration, using the isocenter and the beam direction (165° , in this case) as defined during treatment planning (b). For the example shown in (b), the movable couch rail at the right should be placed at the innermost position to avoid couch intersection.

6.5 Discussion

In IMRT, posterior (oblique) angles of incidence are frequently used, leading more often to intersections of the beam with the treatment couch and/or the immobilization devices. Findings in “in-vivo” EPID measurements obtained during IMRT treatments led to the awareness of substantial treatment couch attenuation and to the beginning of this investigation. The effects of beam attenuation have hardly been described in the literature. Certainly for clinical beam arrangements, this phenomena has been little studied, except by Krithivas *et al.*¹⁷ Most publications concern beam-couch intersection algorithms,¹⁸⁻²⁰ and the loss of skin sparing effect caused by the couch insert and/or immobilization devices.²¹⁻²⁴ Higgins *et al.*²⁵ studied the attenuation of their couch insert and considered it to be minimal. De Ost *et al.*²⁶ encountered an

attenuation of 1% for some couch inserts investigated, using ^{60}Co and 6 MV beams. Krithivas *et al.*¹⁷ found an attenuation of about 10% for the metallic central bar of their treatment couch for a 60° rotation delivery, by measuring with a 0.1 cc PTW ionization chamber in a cylindrical phantom. The present study is performed with an EPID, as opposed to point measurements, which allowed conducting a 2D-study of the beam attenuation by the treatment couch and immobilization devices for clinical individualised set-up configurations. Both the treatment couch and the immobilization devices are composed of several components, which attenuate the beam differently. Beam attenuation by each component also varies with the angle of incidence of the beam. These components have different sizes and shapes, making the positioning of an ionization chamber for beam attenuation measurements not straightforward. Only 2D measurements allow complete evaluation of the beam attenuation for each of these components.

The beam attenuation observed in this study showed the need to account for the immobilization devices during treatment planning. Inclusion of the treatment couch, and especially the moving couch rails, is not straightforward, because the designs of the couch at the treatment unit and at the CT scanner are different. Based on the results obtained in this paper, this inclusion is now being investigated to establish the effect of beam attenuation on the calculated 3D dose distribution for individual patients. Results on this study will be reported in a separate paper. In the meantime, a simple graphical tool was developed to visualize during treatment planning if a treatment field (with a certain field size, gantry angle and isocenter position) intersects absorbing couch parts [Fig. 6-5]. Beam orientations may then be chosen to avoid treatment couch absorption or, if the latter is not possible, the treatment couch configuration can be changed relative to the patient. For instance, for a certain IMRT patient, both couch rails were moved to the center, and the center of the treatment couch was shifted 2 cm to the left relative to the isocenter of the patient to ensure that no absorbing couch parts would be in the beam (see planned position in Fig. 6-3(c)). Additionally, the couch grid insert was used in the reversed position, because for this orientation, the couch insert frame is hollow and therefore less absorbing [Fig. 6-1(b)]. The implementation of this tool pointed at the need for fixation to the couch of the immobilization devices used for the lung cancer patients to ensure identical patient set-up relative to the treatment couch during daily treatment delivery. Fixation of the head support to the treatment couch was already performed for head and neck cancer patients before starting this study.

In addition to the use of the already mentioned graphical tool, posterior oblique beams that might intersect absorbing treatment couch parts are presently simulated at the treatment unit, before or during the first patient fraction, using the light field. If couch absorption is unavoidable for a particular gantry angle, this absorption is then quantified by acquiring EPID images with the treatment couch in the beam, using exactly the same couch coordinates as will be used during treatment delivery. This procedure is now possible because the patient immobilization devices are fixed to the treatment couch, as mentioned above. Based on the measured beam attenuation and the number of treatment fields involved, the physician together with the clinical physicist decide whether the treatment can proceed or if a new plan should be made. Although static fields can be easily visualized using the light field, for IMRT with DMLC this is not straightforward. For the sliding window mode, leaves are closed at the beginning of the treatment, thus inhibiting the visualization of the light field. In these cases, the jaws are set tangent to the most extreme leaf pair positions of the DMLC fields and the leaves are retracted. The light field is then used to show the limits of the treatment field. As an alternative to the use of the light field for IMRT patients, the standard pre-treatment check performed with the EPID (Sec. I.) could also be performed with the treatment couch and the immobilization devices in the beam for posterior oblique beam orientations.

For critical cases, it is essential that for each fraction the set-up of the treatment couch and immobilization device are the same as planned, or established by the verification measurements (pre-treatment or during the first treatment fraction, see above). To minimize the number of occasional set-up errors for critical beams, our patient set-up chart now standard includes a clear illustration or indication of the set-up of the immobilization devices, the position of the couch rails, and the orientation of the couch insert. In our record and verify system, the tolerance levels for the couch position are set as tight as possible, making it patient specific. In order to reduce the risk on incidental errors even further, a readout on the couch rails and insert should be provided at the machine to enable verification of their position and orientation, respectively.

6.6 Conclusions

EPID images can be used to quantify beam attenuation of the different components of the treatment couch and immobilization devices in 2D, for clinical beam configurations. Large attenuation (up to 15%) by the treatment couch and immobilization

devices has been detected in clinical treatments. These findings led to the development of new tools and procedures for planning and treatment delivery to avoid underdosages in the patient.

6.7 Acknowledgments

The authors would like to thank the technicians of the treatment unit for the daily acquisition of the EPID images, and in particular Nadine Post for her efforts on implementing the QA protocol in clinical practice. This work was supported by the 'Fundação para a Ciência e a Tecnologia' and by the Dutch Cancer Society (grant DDHK 98-1681).

6.8 References

- ¹B. Fraass, K. Doppke, M. Hunt, G. Kutcher, G. Starkschall, R. Stern, and J. van Dyke, "American Association of Physicists in Medicine Radiation Therapy Committee Task Group 53: quality assurance for clinical radiotherapy treatment planning," *Med. Phys.* **25**, 1773-1829 (1998).
- ²G. J. Kutcher, L. Coia, M. Gillin, W. F. Hanson, S. Leibel, R. J. Morton, J. R. Palta, J. A. Purdy, L. E. Reinstein, and G. K. Svensson, "Comprehensive QA for radiation oncology: report of AAPM Radiation Therapy Committee Task Group 40," *Med. Phys.* **21**, 581-618 (1994).
- ³T. LoSasso, C. S. Chui, and C. C. Ling, "Comprehensive quality assurance for the delivery of intensity modulated radiotherapy with a multileaf collimator used in the dynamic mode," *Med. Phys.* **28**, 2209-2219 (2001).
- ⁴D. A. Low, "Quality assurance of intensity-modulated radiotherapy," *Semin. Rad. Oncol.* **12**, 219-228 (2002).
- ⁵K. L. Pasma, M. Kroonwijk, J. C. J. de Boer, A. G. Visser, and B. J. M. Heijmen, "Accurate portal dose measurement with a fluoroscopic electronic portal imaging device for open and wedged beams and dynamic multileaf collimation," *Phys. Med. Biol.* **43**, 2047-2060 (1998).
- ⁶K. L. Pasma, M. L. P. Dirkx, M. Kroonwijk, A. G. Visser, and B. J. M. Heijmen, "Dosimetric verification of intensity modulated beams produced with dynamic multileaf collimation using an electronic portal imaging device," *Med. Phys.* **26**, 2373-2378 (1999).
- ⁷M. Kroonwijk, K. L. Pasma, S. Quint, P. C. M. Koper, A. G. Visser, and B. J. M. Heijmen, "In vivo dosimetry for prostate cancer patients using an electronic portal imaging device: demonstration of internal organ motion," *Radiother. Oncol.* **49**, 125-132 (1998).
- ⁸H. C. de Boer and B. J. M. Heijmen, "A protocol for the reduction of systematic patient set-up errors with minimal portal imaging workload," *Int. J. Rad. Oncol. Biol. Phys.* **50**, 1350-1365 (2001).
- ⁹H. C. de Boer, J. R. van Sornsens de Koste, S. Senan, A. G. Visser, and B. J. M. Heijmen, "Analysis and reduction of 3D systematic and random set-up errors during the simulation and treatment of lung cancer patients with CT-based external beam radiotherapy dose planning," *Int. J. Rad. Oncol. Biol. Phys.* **49**, 857-868 (2001).

-
- ¹⁰H. C. de Boer, J. R. van Sornsens de Koste, C. L. Creutzberg, A. G. Visser, P. C. Levendag, B. J. M. Heijmen, "Electronic portal image assisted reduction of systematic set-up errors in head and neck irradiation," *Radiother. Oncol.* **61**, 299-308 (2001).
- ¹¹S. Quint, H. C. de Boer, J. R. van Sornsens de Koste, B. J. M. Heijmen, and M. J. Olofsen-van Acht, "Set-up verification of cervix cancer patients treated with long treatment fields; implications of a non-rigid bony anatomy," *Radiother. Oncol.* **60**, 25-29 (2001).
- ¹²J. C. Stroom, M. J. Olofsen-van Acht, S. Quint, M. Seven, M. de Hoog, C. L. Creutzberg, H. C. de Boer, and A. G. Visser, "On-line set-up corrections during radiotherapy of patients with gynecologic tumors," *Int. J. Rad. Oncol. Biol. Phys.* **46**, 499-506 (2000).
- ¹³J. C. Stroom, M. Kroonwijk, K. L. Pasma, , P. C. M. Koper, E. B. Dieren, and B. J. M. Heijmen, "Detection of internal organ movement in prostate cancer patients using portal images," *Med. Phys.* **27**, 452-461 (2000).
- ¹⁴S. C. Vieira, M. L. P. Dirkx, K. L. Pasma, and B. J. M. Heijmen, "Fast and accurate leaf verification for dynamic multileaf collimation using an electronic portal imaging device," *Med. Phys.* **29**, 2034-2040 (2002).
- ¹⁵G. Quinn, "An investigation into radiotherapy treatment couch sag," *Radiother. Today* **59**, 9-12 (1993).
- ¹⁶J. C. J. de Boer, B. J. M. Heijmen, K. L. Pasma, and A. G. Visser, "Characterization of a high elbow, fluoroscopic electronic portal imaging device for portal dosimetry," *Phys. Med. Biol.* **45**, 197-216 (2000).
- ¹⁷G. Krithivas and S. N. Rao, "Arc therapy dose perturbation due to the center bar in a Clinac 4/100 couch assembly," *Med. Dosim.* **13**, 15-18 (1988).
- ¹⁸J. Meyer, J. A. Mills, O. C. Haas, K. J. Burnham, and E. M. Parvin, "Accommodation of couch constraints for coplanar intensity modulated radiation therapy," *Radiother. Oncol.* **61**, 23-32 (2001).
- ¹⁹M. S. Muthuswamy, "A method of beam-couch intersection detection," *Med. Phys.* **26**, 229-235 (1999).
- ²⁰E. D. Yorke, "The geometry of avoiding beam intersections and blocking tray collisions," *Med. Phys.* **16**, 288-291 (1989).
- ²¹M. J. Butson, P. K. Yu, and P. E. Metcalfe, "Measurement of off-axis and peripheral skin dose using radiochromic film," *Phys. Med. Biol.* **43**, 2647-2650 (1998).
- ²²J. Carl and A. Vestergaard, "Skin damage probabilities using fixation materials in high-energy photon beams," *Radiother Oncol* **55**, 191-198 (2000).
- ²³D. P. Fontenla, J. J. Napoli, M. Hunt, D. Fass, B. McCormick, and G. J. Kutcher, "Effects of beam modifiers and immobilization devices on the dose in the build-up region," *Int. J. Rad. Oncol. Biol. Phys.* **30**, 211-219 (1994).
- ²⁴D. E. Mellenberg, "Dose behind various immobilization and beam-modifying devices," *Int. J. Rad. Oncol. Biol. Phys.* **32**, 1193-1197 (1995).
- ²⁵D. M. Higgins, P. J. Whitehurst, and A. M. Morgan, "The effect of carbon fiber couch inserts on surface dose with beam size variation," *Med. Dosim.* **26**, 251-254 (2001).
- ²⁶B. de Ost, J. Vanregemorter, B. Schaeken, and D. van den Weyngaert, "The effect of carbon fiber inserts on the build-up and attenuation of high energy photon beams," *Radiother. Oncol.* **45**, 275-277 (1997).

CHAPTER 7. SIFT: A METHOD TO VERIFY THE IMRT FLUENCE DELIVERED DURING PATIENT TREATMENT USING AN ELECTRONIC PORTAL IMAGING DEVICE

S C Vieira, M L P Dirkx, B J M Heijmen, H C J de Boer

Int. J. Radiat. Oncol. Biol. Phys. **60**, 981-993, 2004

7.1 Abstract

Radiotherapy patients are increasingly treated with intensity modulated radiotherapy (IMRT) and high tumor doses. As part of our quality control program to ensure accurate dose delivery, a new method was investigated which enables the verification of the IMRT fluence delivered during patient treatment using an electronic portal imaging device (EPID), irrespective of changes in patient geometry.

Each IMRT treatment field is split into a static field and a modulated field, which are delivered in sequence. Images are acquired for both fields using an EPID. The portal dose image (PDI) obtained for the static field is used to determine changes in the patient geometry between the planning CT-scan and the time of treatment delivery. Knowing these changes, the delivered IMRT fluence can be verified using the PDI of the modulated field. This method, called Split IMRT Field Technique (SIFT), was first validated for several phantom geometries, followed by clinical implementation for a number of patients treated with IMRT.

SIFT allows for an accurate verification of the delivered IMRT fluence (generally within 1% (SD)), even if large inter-fraction changes in patient geometry occur. For inter-fraction radiological path length changes of 10 cm, deliberately introduced errors in the delivered fluence could still be detected to within 1% accuracy. Application of SIFT requires only a minor increase in treatment time relative to the standard IMRT delivery.

A new technique to verify the delivered IMRT fluence from EPID images, which is independent of changes in the patient geometry, has been developed. SIFT has been clinically implemented for daily verification of IMRT treatment delivery.

7.2 Introduction

The strong increase in the application of intensity modulated radiotherapy (IMRT), often combined with delivery of high tumor doses, requires the development of tools for adequate quality assurance (QA) of the treatment delivery.¹⁻⁴ Daily verification of the dose delivery during patient treatment rarely occurs. Instead, the dose distribution delivered by IMRT treatment fields is generally validated before starting patient treatment by performing measurements with an ionization chamber, film, or thermoluminescence dosimeters (TLDs) in a phantom.⁵⁻¹⁰ Some of these measurements are rather time consuming, do not provide complete two-dimensional (2D) information, and their accuracy is highly dependent on the exact placement of the dosimeters inside the field, due to the dose gradients present in IMRT. Consequently, electronic portal imaging devices (EPIDs) offer an attractive option for IMRT verification.¹¹⁻¹⁷ EPIDs provide 2D portal dose maps, while no time is required to set-up these devices. Moreover, EPID measurements can be performed during treatment without introducing a time delay.

In our department, we are currently implementing an individualised dosimetric quality assurance protocol, which relies solely on EPIDs to verify the dose distribution delivered to the patient.¹⁸ This protocol is used for all our IMRT patients treated with dynamic multileaf collimation (DMLC). Before the first treatment fraction, electronic portal images (EPIs) are acquired for each IMRT field in absence of the patient. These images are converted into portal dose images (PDIs),¹² and compared with the corresponding PDIs predicted by the treatment planning system (TPS).¹⁹ This pre-treatment check is used to verify that the treatment parameters established during treatment planning (e.g., the beam energy, monitor units (MU), and optimized leaf trajectories) are indeed generating the expected IMRT fluence.¹⁴ Each treatment day, prior to the start of the first IMRT treatment, the EPID is used to check if the multileaf collimator is functioning properly by acquiring images of a 5 mm sliding gap.²⁰ During patient treatment, EPIs of all treatment fields are acquired to verify the dose delivery according to methods described in previous work.^{21, 22} Additional images are collected using small exposure, static orthogonal fields, to establish the position of the patient at the time of treatment.²³⁻²⁶

When comparing PDIs measured during patient treatment with the corresponding PDIs calculated by the TPS, large portal dose differences may be found, which can be either related to deviations in the delivered fluence or due to changes in the patient

geometry between the planning computed tomography (CT) and treatment delivery (e.g., differences in patient positioning, internal organ motion).^{21, 22, 27, 28} Till now, this was a fundamental limitation for any transmission dose measurement. In this paper, a new technique for EPID-based verification of the delivered fluence during IMRT treatment, which overcomes this shortcoming, is described. The Split IMRT Field Technique (SIFT) is based on splitting the prescribed IMRT field into a static (non-modulated) field and a residual modulated field. In this paper, the efficacy of SIFT is demonstrated using phantom measurements and results of its implementation in clinical practice.

7.3 Materials and Methods

7.3.1 The EPID

All measurements were performed at a Clinac 2300C/D (Varian Associates, Palo Alto, CA) equipped with a camera-based EPID (Cablon Medical-Theraview Technology, Leusden, The Netherlands). The EPID is a low elbow type system with a fluorescent screen, a mirror, and a cooled CCD camera.²⁹ This device has three characteristics specifically relevant to dosimetric applications,³⁰ and for DMLC in particular: (i) an excellent short and long term stability, (ii) the signal is integrated simultaneously in all 1024×1024 pixels, and (iii) the dead time in between acquisition of subsequent frames is only 0.1 ms. EPIs are acquired using the Theraview NT software (Cablon Medical-Theraview Technology, Leusden, The Netherlands). For the results presented in this paper, the EPID detector plane was positioned at a distance of 170 cm from the focus, the standard position in our routine clinical practice. This distance yields a maximum radiation field of view of $23 \times 23 \text{ cm}^2$ at the isocenter plane. Conversion of EPIs into PDIs is performed in three steps.¹² First, a correction is applied for minor non-linearity of the EPID response and a median filter is used to reduce the image high frequency noise. Second, the image is deconvolved with a point spread function to correct for the “optical cross-talk” (also referred as “optical glare”)³¹ originated in the EPID structure. Finally, the resulting image is divided by a sensitivity array to correct for the non-uniform spatial EPID response. This sensitivity array is derived from EPIs and corresponding ionization chamber measurements both performed for a set of square fields at a focus-detector distance of 170 cm.

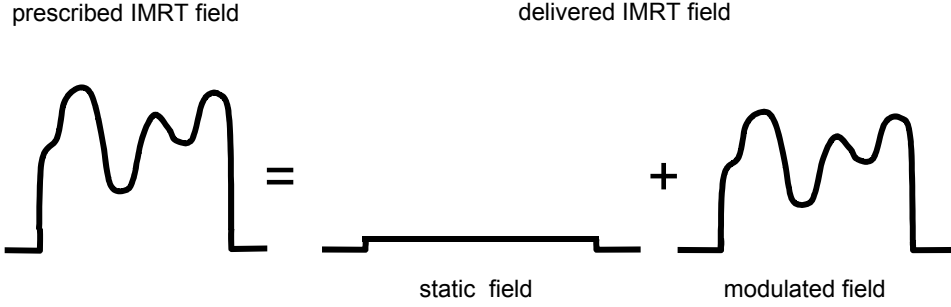


Figure 7-1 Principle of SIFT: a prescribed IMRT field is split into a static, low exposure field and a residual modulated field.

All image coordinates referenced in this paper pertain to the isocentre plane. The x and y position coordinates are defined in the direction of leaf motion, and perpendicular to this direction, respectively. All presented PDI values shown were normalized to the on-axis PDI value measured for a static $10 \times 10 \text{ cm}^2$ field delivered with 100 MU.

7.3.2 Splitting an IMRT field

SIFT is based on splitting the IMRT field into a static (non-modulated) field and a residual modulated field (Fig.7-1), which are delivered sequentially. Splitting of the field can be performed automatically with our treatment planning system (Cadplan, version 6.3.5, Varian Associates, Palo Alto, CA). The static field is delivered with a small number of MU (typically 6-10 MU) and with the same field aperture as the modulated field. During patient treatment, the time between the delivery of both fields should be minimal to avoid intra-fraction changes in the patient geometry. For both fields, PDIs are obtained, yielding $\text{PDI}^{\text{static}}$ and PDI^{mod} , respectively.

The dose measured in the EPID detector plane, with absorber (phantom or patient) of equivalent thickness t in the radiation field, $\text{PDI}(x,y)$, can be expressed as the sum of a primary and a scatter component:

$$\text{PDI}(x, y) = T_p(x, y) \text{PDI}_{t=0}(x, y) + S(x, y) \quad 7-1$$

where $PDI_{t=0}$ is the portal dose that would be measured in absence of the absorber, $T_p(x,y)$ is the contribution of the primary irradiation after transmission through the absorber, and $S(x,y)$ is the scatter contribution to the portal dose.¹⁹ $PDI_{t=0}$ equals the fluence convolved with a dose deposition kernel for the fluorescent screen of the EPID.³² Hence, $PDI_{t=0}$ directly reflects the fluence delivered by the treatment unit. While $T_p(x,y)$ is only dependent on the radiological equivalent path length through the absorber, the scatter component, $S(x,y)$, is also affected by the fluence map of the incoming beam, particularly if the distance between the patient and the EPID is small.¹⁹

In the approximation that the scatter contribution to the PDI is negligible relative to the primary contribution, the ratio between the PDI obtained for the modulated and the static field, PDI_{ratio} , can be expressed as:

$$PDI_{ratio}(x, y) = \frac{PDI^{mod}(x, y)}{PDI^{static}(x, y)} \cong \frac{PDI_{t=0}^{mod}(x, y)}{PDI_{t=0}^{static}(x, y)} \quad 7-2$$

provided that the patient anatomy does not change during delivery of the two SIFT fields. Because the two fields are delivered in rapid succession, the change in anatomy transmission will be generally negligible. Previous work¹⁹ has shown that the approximation of Eq. (7-2) is valid for large air gaps (≥ 50 cm) between patient and EPID and small field sizes ($< 10 \times 10$ cm²). In that case, the PDI_{ratio} becomes the ratio of fluences of the modulated and the static fields, *irrespective of the patient anatomy*. Although this approximation will no longer be accurate for small air gaps and large field sizes due to the increasing contribution of patient scatter, one still expects the PDI_{ratio} to be primarily a measure of interfraction changes in the fluence of the modulated field, provided that the fluence of the static field is constant. In particular, because the scatter contribution changes very slowly with anatomy changes,¹⁹ it is expected that the difference in the PDI_{ratio} for fractions f_1 and f_2 ,

$$\Delta PDI_{ratio}(x, y) = PDI_{ratio, f_2}(x, y) - PDI_{ratio, f_1}(x, y) \quad 7-3$$

is a measure of the interfraction changes in the modulated fluence of the split IMRT field, even if interfraction changes in patient anatomy occur. In the results section, this assertion will be made plausible.

7.3.3 The accuracy of IMRT delivery with SIFT

The accuracy of IMRT delivery with SIFT was tested by acquiring EPIs of both the static and the modulated parts of the split IMRT field. The sum of these resulting PDIs was then compared with the PDI of the corresponding non-split IMRT field. All these measurements were performed in the absence of a patient.

In addition, it was verified for a number of IMRT plans used in our clinic for head and neck and prostate cancer patients, whether SIFT implied any detrimental consequences for the dose delivery to these patients as predicted by the TPS. This can occur if the modulated fluence values are lower than the fluence of the low MU static field used in SIFT. For this purpose, the dose distribution for the IMRT plans with split and non-split fields was compared in individual CT slices, and dose volume histograms (DVH) for both the tumor and sensitive structures were evaluated.

7.3.4 Accuracy of output and flatness of the low MU static field

As mentioned in the previous section, the static field in SIFT is delivered with a few MU (typically 6-10 MU). Therefore, EPID measurements were performed to establish the linearity and the reproducibility of the beam output, and the stability of the beam flatness at low exposures. The output of the accelerator was determined for a 20×20 cm² static field, using 2, 4, 6, 10 and 100 MU. To study the impact of beam attenuation (i.e., EPI signal height) as encountered in clinical practice, measurements were performed with homogeneous polystyrene phantoms (density=1.06 g cm⁻³) of 5, 10, 20 and 30 cm thickness. The distance between the phantom and the EPID was kept fixed at 60 cm, a typical value in our clinical set-up. To analyze the short term reproducibility of the beam output for low exposures, the measurements were repeated 5 times in rapid succession; the long term reproducibility was derived from repeated measurements over a period of 20 weeks. On-axis EPI values were calculated as the average value in a central region of 0.8×0.8 cm², in order to minimize the effects of noise. The beam profile of the static field was analyzed from the same images, after normalization to the on-axis value.

7.3.5 Validation of SIFT using phantom measurements

To validate SIFT, phantom measurements were first performed for a number of test fluence maps. In this paper, results for the fluence map illustrated in Fig. 7-2 will be presented. To assess the impact of changes in patient thickness, homogeneous polystyrene slab phantoms of 5 up to 30 cm thickness were used. To simulate the presence of small and large gas pockets, air gaps of $4 \times 4 \text{ cm}^2$ and 2 cm thick, and of $9 \times 9 \text{ cm}^2$ and 6 cm thick were introduced in the center of a phantom of 30 cm thickness. Changes in patient set-up were simulated with an Alderson phantom by moving the couch 1 cm in the longitudinal direction with respect to the intended isocenter position. In addition, the couch was rotated by 3 degrees. Finally, to determine the sensitivity of SIFT to changes in the delivered IMRT fluence, errors were introduced deliberately in the IMRT fluence delivered to a polystyrene phantom of 10 cm thick, and in absence of any absorber.

For all tests, the phantom was sequentially irradiated with the static field and the corresponding modulated field, and EPIDs were acquired for both fields. Next, a change was introduced either in the phantom set-up and/or in the delivered fluence (depending on the test), and the EPID measurements for the static and the modulated field were repeated. If the delivered fluence is reproducible, the $\text{PDI}_{\text{ratio}}$ will be constant for all situations, except for the tests in which the fluence was deliberately changed. The default distance between the exit surface of the phantom and the detector (L) was 60 cm. For some cases, measurements were also performed for L equal to 15 or 30 cm, to analyze the impact on the results obtained with SIFT in case of a relatively large contribution of scatter from the phantom to the detector.

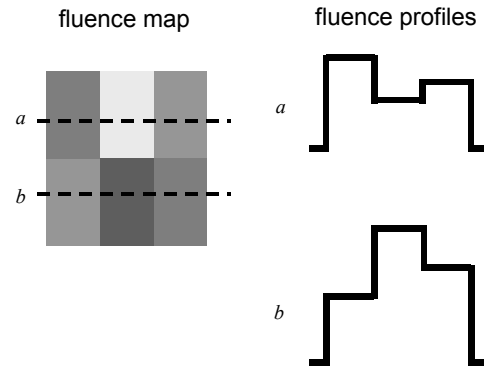


Figure 7-2 Fluence map used for the phantom measurements. At right, fluence profiles at the levels *a* and *b* are displayed.

7.3.6 Application of SIFT in clinical practice

The application of SIFT to verify the IMRT fluence, delivered with DMLC, was tested clinically for head and neck cancer patients and prostate cancer patients. For each treatment field, EPIDs were acquired for the static field and the modulated field in every treatment fraction. The two fields were delivered with a few seconds interval. Results for one prostate cancer patient and two head and neck cancer patients are reported in this paper.

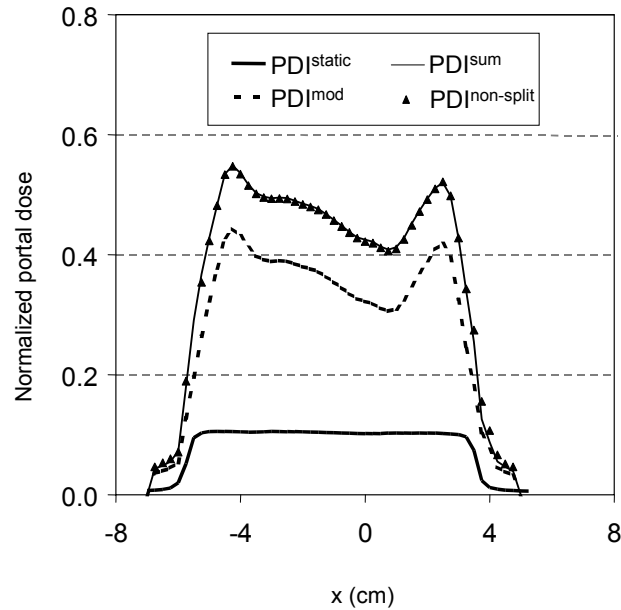


Figure 7-3 Comparison of a normalized portal dose profile measured with the EPID for a non-split IMRT field (triangles) and a split IMRT field (solid line). The latter is the sum of the PDI measured for a static field (thick solid line) and the PDI obtained for the residual modulated field (dashed line).

7.4 Results

7.4.1 The accuracy of IMRT delivery with SIFT

In Fig. 7-3, the sum of the PDIs obtained for the static field and the modulated field of a split IMRT field are compared with the PDI obtained for the non-split IMRT field. An agreement of $-0.3 \pm 0.2\%$ (1SD) was observed inside the field boundaries, and within 0.02 cm in the penumbra region. This result shows that SIFT can be executed very accurately without compromising the accuracy of IMRT dose delivery. When comparing the dose distributions calculated by our TPS for IMRT plans with split and non-split fields, negligible differences were found in the target region for our prostate and head and neck treatments. For the organs at risk, a dose increase of less than 0.3 Gy (i.e., 0.5% of the dose prescribed to the tumor) was generally observed when delivering the static fields with 10 MU. For some patients, static fields of 3-6 MU were required to render this small dose increase. As mentioned in the next section,

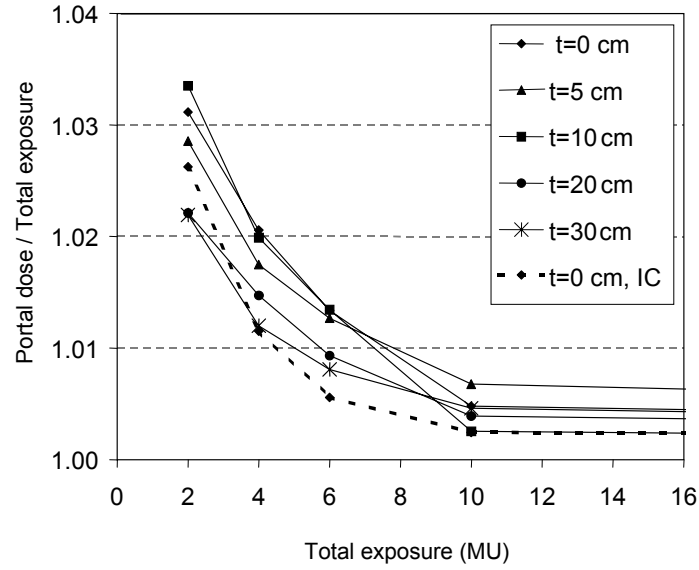


Figure 7-4 Ratio of the on-axis portal dose measured with the EPID and the total exposure delivered by the linac for several phantom thicknesses (solid lines). The ratio is normalized to 1 for a 100 MU exposure. The dashed line represents the ratio derived from ionization chamber (IC) measurements in the absence of an absorber.

even exposures as low as 2 MU can be reliably used, indicating that SIFT is broadly applicable without compromising the dose distribution.

7.4.2 Accuracy of output and flatness of the low MU static field

The linearity of the accelerator output for low MU is shown in Fig.7-4 for several phantom thicknesses. The short term reproducibility of these results over the entire range of the depicted MU values was within 0.5% (1SD), whereas the long term reproducibility was within 0.7% (1SD). It is clear that the beam output is not linear with MU over this range of MUs. The largest deviation (about 3%) was observed at 2 MU. The non-linearity of the output is independent of the phantom thickness and is reproduced, within the accuracy of the measurements, when performing ionization chamber measurements at the same focus to detector distance as used for the EPID measurements (see dashed line in Fig. 7-4). Therefore, the non-linearity of the portal dose with MU is related to the output of the linac and is not caused by the EPID measurements.

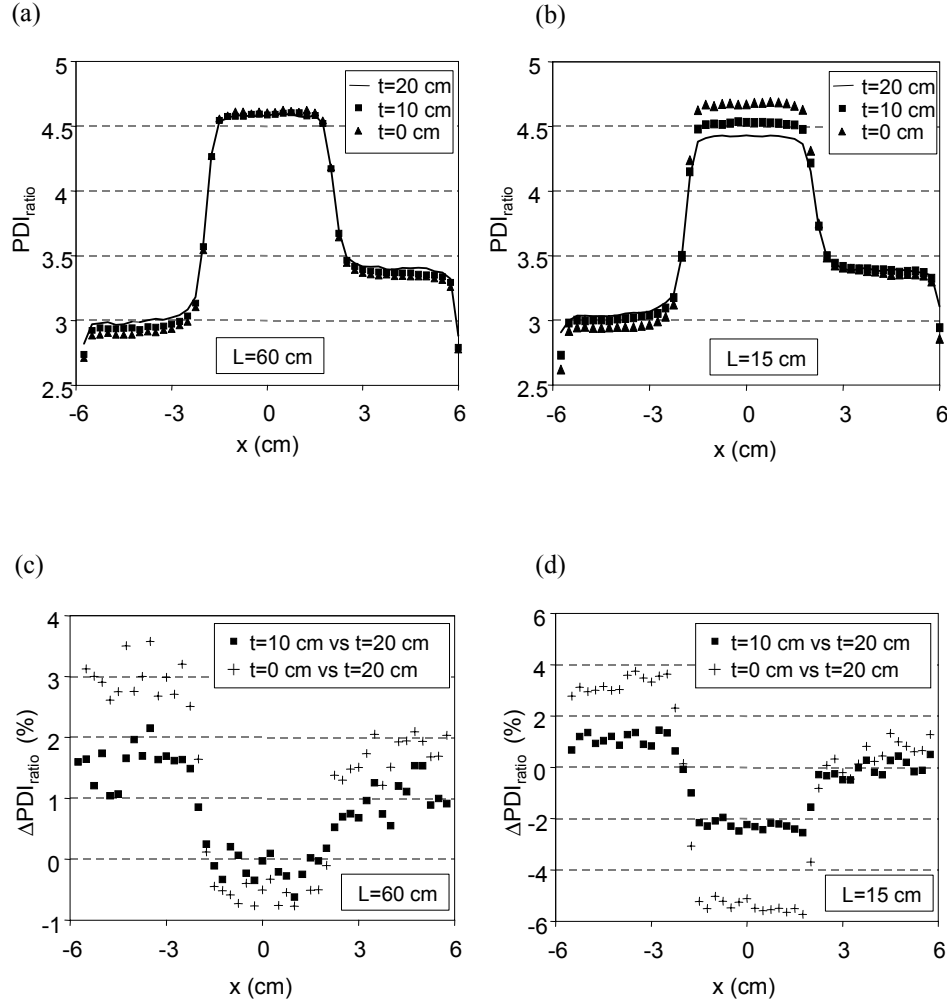


Figure 7-5 (a) and (b) Profile of the PDI_{ratio} obtained for profile b in Fig. 7-2 in absence of an absorber ($t=0$ cm) and behind homogenous phantoms of 10 and 20 cm thickness placed at the distances 60 cm and 15 cm from the EPID detector plane, respectively. (c) and (d) Difference between the PDI_{ratio} profiles shown in (a) and (b). For a distance to the EPID plane of 60 cm, ΔPDI_{ratio} between $t=10$ cm and $t=20$ cm (squares) was equal to $0.6 \pm 1.0\%$ (1SD), and between $t=0$ cm and $t=20$ cm (cross) was equal to $1.3 \pm 1.6\%$ (1SD). For a distance of 15 cm, these differences were equal to $-0.4 \pm 1.4\%$ (1SD) and $-0.7 \pm 3.5\%$ (1SD), respectively.

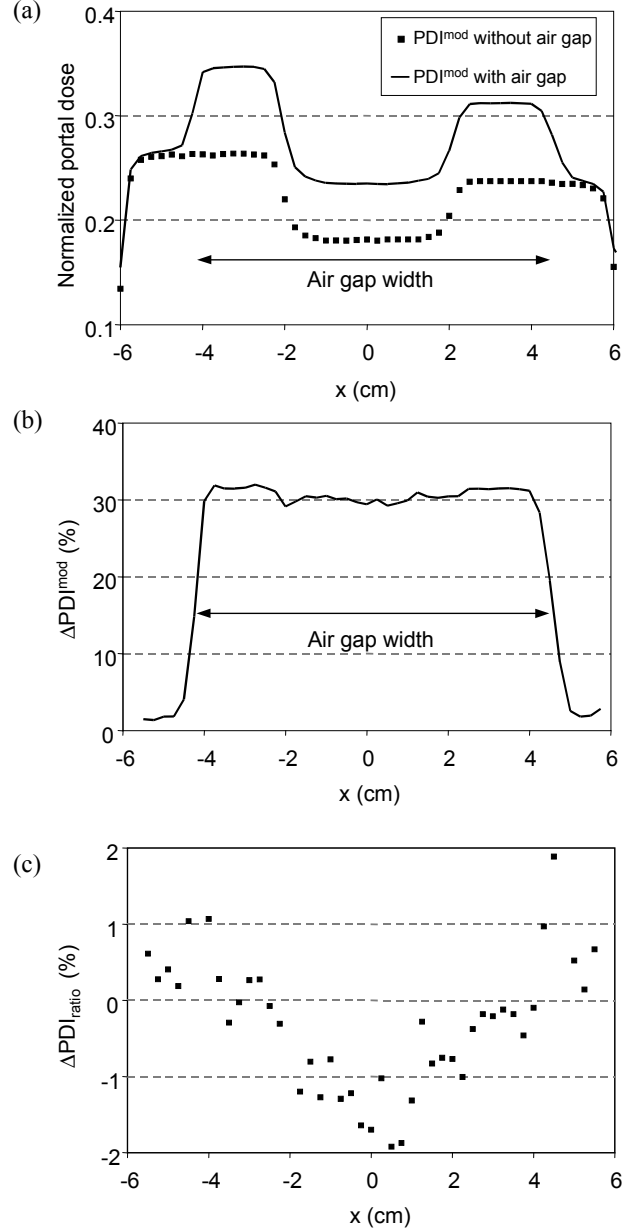
Due to the reproducibility of the output measurements with phantom thickness and in time, the output non-linearity does not influence the accuracy of SIFT in establishing interfraction reproducibility through ΔPDI_{ratio} (Eq. 7-3). If the PDI_{ratio} is used for ab-

solute fluence reconstruction, the non-linearity at very low exposures can easily be accounted for by applying a scaling factor to PDI_{static} , which only depends on the number of MU for the static field. Regarding the reproducibility of the beam profile for the static fields, deviations within 0.5% (1SD) were observed over the entire range of monitor units investigated, independent of phantom thickness.

7.4.3 Validation of SIFT using phantom measurements

First, the interpretation of the PDI_{ratio} as a reliable measure of the delivered fluence, irrespective of changes in patient geometry, will be addressed. In Fig.7-

Figure 7-6 (a) Profile of PDI^{mod} with and without a $9 \times 9 \text{ cm}^2$ and 6 cm thick air gap in the center of a 30 cm thick polystyrene for profile b in Fig. 7-2. In (b) and (c), the differences in PDI^{mod} and in PDI_{ratio} are shown, respectively. While differences of up to 30% are observed in PDI^{mod} , the average value of the difference in PDI_{ratio} is $-0.2 \pm 1.1\%$ (1SD), demonstrating that the presence of the large air gap had a negligible impact on the PDI_{ratio} .



5a, the PDI_{ratio} derived from EPID measurements for homogenous phantoms of $t=0$, 10 and 20 cm thickness is shown.

Note that the profile for $t = 0$ cm is the actual dose profile generated by the fluence map of Fig. 7-2b. Given the fact that the PDI of the modulated field is divided by the PDI of the flat static field, the shape of the delivered modulated profile also reappears in the PDI_{ratio} profile for phantom thickness 10 and 20 cm. For instance, when increasing the thickness from 10 to 20 cm, both PDI^{mod} and PDI^{static} were reduced by 18% on average and these differences canceled out in the PDI_{ratio} . The effect of scatter, although small, is visible in the PDI_{ratio} profiles of Fig. 7-5a. As the phantom thickness increases from 0 to 20 cm, both peaks and valleys in the fluence distribution slightly flatten. This is an expected behaviour as the scatter contribution can be described by convolution of the primary fluence with a long range kernel.¹⁹ Nevertheless, the effect of this scatter contribution is small, particularly when considering the changes in the PDI_{ratio} between $t = 10$ cm and $t = 20$ cm (Fig. 7-5c). For this case, ΔPDI_{ratio} was $0.6 \pm 1.0\%$ (1SD). Hence, the PDI_{ratio} accurately reflects the delivered fluence profile, even in the presence of (interfraction) patient thickness changes as large as 10 cm. The above results were obtained for $L = 60$ cm. In Fig. 7-5b, the PDI_{ratio} for the same phantom thicknesses, but obtained for a small air gap between phantom and EPID of $L = 15$ cm is depicted. As expected, the impact of scatter is now larger, but follows the same trend with thickness as for $L = 60$ cm (Fig. 7-5a). Between $t=10$ cm and $t=20$ cm phantom thickness, ΔPDI_{ratio} is equal to $-0.4 \pm 1.4\%$ (1SD) (Fig. 5d), indicating that the delivered fluence can still be verified accurately. Even for a large thickness change of 20 cm and very small air gaps, the PDI_{ratio} primarily represents the delivered fluence of the modulated field.

Changes in the PDI_{ratio} are also examined for inhomogeneous phantoms. After introducing a large air gap of 9×9 cm² and 6 cm thick in the polystyrene phantom, differences of about 30% occurred in the PDIs obtained for both the static and the modulated field relative to the measurements without air gap (see Fig. 7-6a and 7-6b). Nevertheless, the PDI_{ratio} was insensitive to the presence of the introduced air gap, as observed from Fig. 7-6c. The ΔPDI_{ratio} was equal to $-0.2 \pm 1.1\%$ (1SD). Similar results were achieved for a small air gap of 15 cm.

In Fig. 7-7a, a two dimensional percentage difference map between the PDI of the modulated field acquired before and after translation of the Alderson phantom by 1 cm in the longitudinal directional is shown. Deviations of up to 14% are observed near the vertebra due to misalignment of the phantom (see Fig. 7-7c). In Fig. 7-7b, the

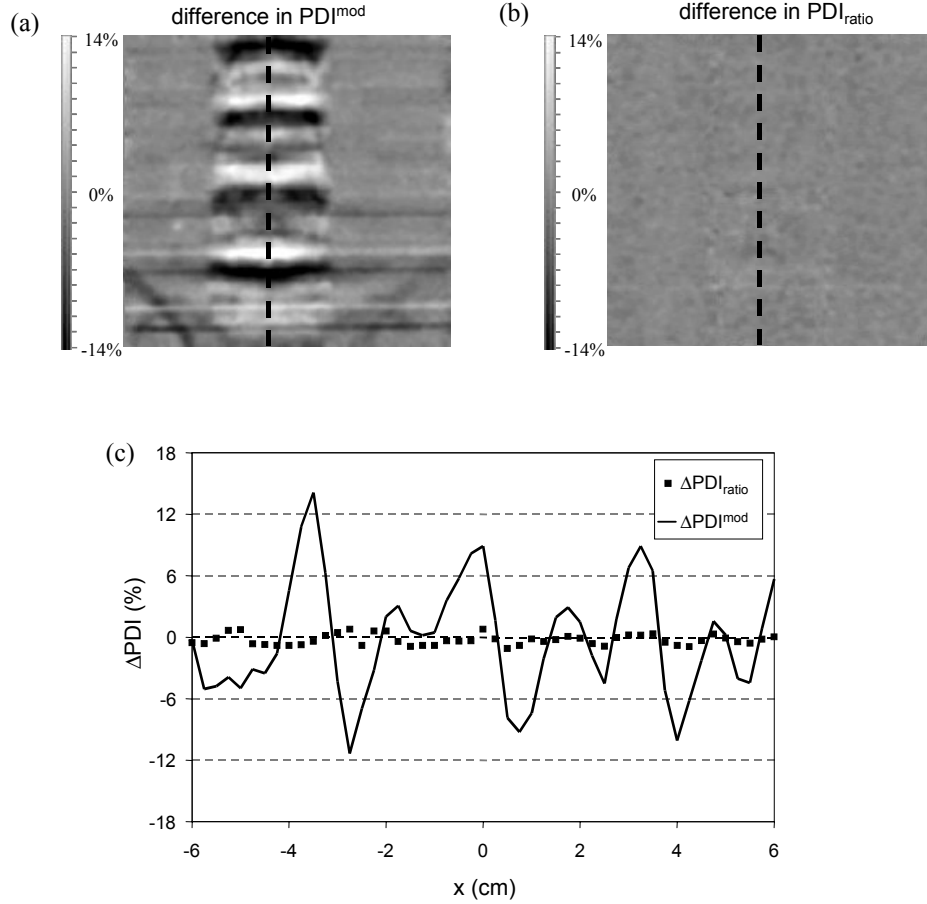


Figure 7-7 Percentage difference in PDI^{mod} (a) and in PDI_{ratio} (b) after translating the Alderson phantom 1 cm in the longitudinal direction. In (c), the differences in PDI^{mod} and in PDI_{ratio} along the dashed line in (a) and (b), respectively, are shown. While differences up to 14% occurred in PDI^{mod} near the vertebra due to the 1 cm set-up change, the PDI_{ratio} was insensitive to this change in phantom position. The difference in PDI_{ratio} was equal to $0.3 \pm 0.5\%$ (1SD).

difference in the corresponding PDI_{ratio} images is presented, showing no deviations related to the change in phantom position. The reproducibility of the PDI_{ratio} was $0.3 \pm 0.5\%$ (1SD). After rotating the phantom by 3 degrees, the PDI_{ratio} was again highly reproducible to within $0.3 \pm 0.6\%$ (1SD).

Next, the sensitivity of the PDI_{ratio} to fluence delivery errors is analysed. In addition to the changes in phantom geometry described above, errors were deliberately intro-

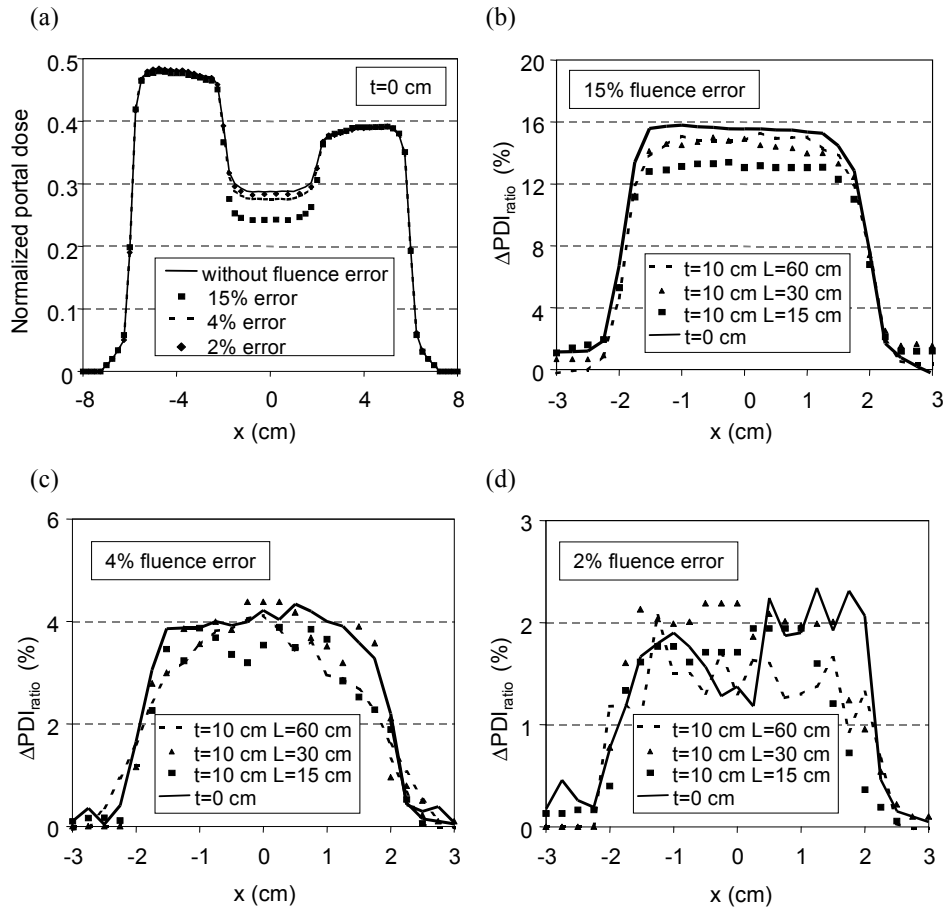


Figure 7-8 (a) Portal dose profile measured in absence of an absorber during delivery of a fluence map without error (solid line), and with a fluence error of 15% (squares), 4% (dashed line), and 2% (diamonds), introduced in the central part of the profile. (b) Difference in the PDI_{ratio} obtained with and without the error in the delivered fluence of 15%, shown in (a). The measurements were performed in absence of an absorber (line) and with a phantom of 10 cm thickness placed at the distance of 60 cm (dashed line), 30 cm (triangles), and 15 cm (squares) from the EPID detector plane, respectively. (c) and (d), the same as (b) but for introduced errors of 4% and 2% in the delivered fluence, respectively.

duced in the delivered fluence (see Fig. 7-8). The largest fluence error introduced (15%) translated in a ΔPDI_{ratio} of about 15.5% in absence of an absorber (Fig. 7-8a). In Fig. 7-8b, this value is compared with the ΔPDI_{ratio} measured for a phantom of 10 cm thick, positioned at distances of $L = 15, 30$ and 60 cm from the EPID plane. For distances of 30 and 60 cm, the ΔPDI_{ratio} accurately reflects the introduced error to

within 1%, either with or without the phantom in the field. This result indicates that errors in the delivered fluence can be detected accurately through $\Delta\text{PDI}_{\text{ratio}}$, irrespective of patient geometry. For the phantom to detector distance of 15 cm, $\Delta\text{PDI}_{\text{ratio}}$ is about 2% smaller (Fig. 7-8b). This decrease in $\Delta\text{PDI}_{\text{ratio}}$ can be expected from the increased contribution from patient scatter at $L = 15$ cm. Such a small distance from the patient to the detector is rarely encountered in our clinical set-up because of collision risks and reduced portal image quality. Nevertheless, the detection of the fluence error (about 13% instead of 15%) is still unambiguous.

In Fig. 7-8c, the $\Delta\text{PDI}_{\text{ratio}}$ measured for much smaller, deliberately introduced fluence errors of 2 and 4% are shown, for the same set-ups. In all cases, these errors were accurately detected.

7.4.4 Application of SIFT in clinical practice

Fig. 7-9, 7-10 and 7-11 show examples of the application of SIFT for fluence verification during IMRT treatments of a prostate cancer patient and two head and neck cancer patients. The static field of each IMRT field was delivered with 10 MU for the prostate cancer patient and with 6 MU for the head and neck patients. Large deviations of up to 12% and 20% were observed between the PDIs of the modulated field measured in two treatment fractions for the prostate cancer patient (Fig. 7-9b) and for both head and neck cancer patients (Fig. 7-10b and 7-11b), respectively. In contrast, the $\text{PDI}_{\text{ratio}}$ for the two fractions of each patient are identical to within 1% (1SD). Hence, the observed deviations can be attributed to changes in the patient geometry, whereas the delivered fluence reproduced accurately. When analyzing the PDIs obtained for the static field in each fraction, it was concluded that the measured deviations for the prostate cancer patient were due to a gas pocket present in one of the treatment fractions (see circle in Fig. 7-9d). Changes in rectal filling and the presence of gas pockets during treatment of prostate cancer patients has been reported in previous studies.^{21, 33} Therefore, the example illustrated in Fig. 7-9 is a representative case of anatomy changes during treatment. For one of the head and neck cancer patients, the observed deviations could be explained in part by differences in the shoulder position (see inferior arrow in Fig. 7-10e). Other deviations were located near the trachea (see superior arrow in Fig. 7-10e). For the second head and neck patient, the observed deviations were mainly related to inter-fraction changes in the position of the body contour and of the patient teeth (indicated by the arrow and the circle in Fig. 7-11e, respectively).

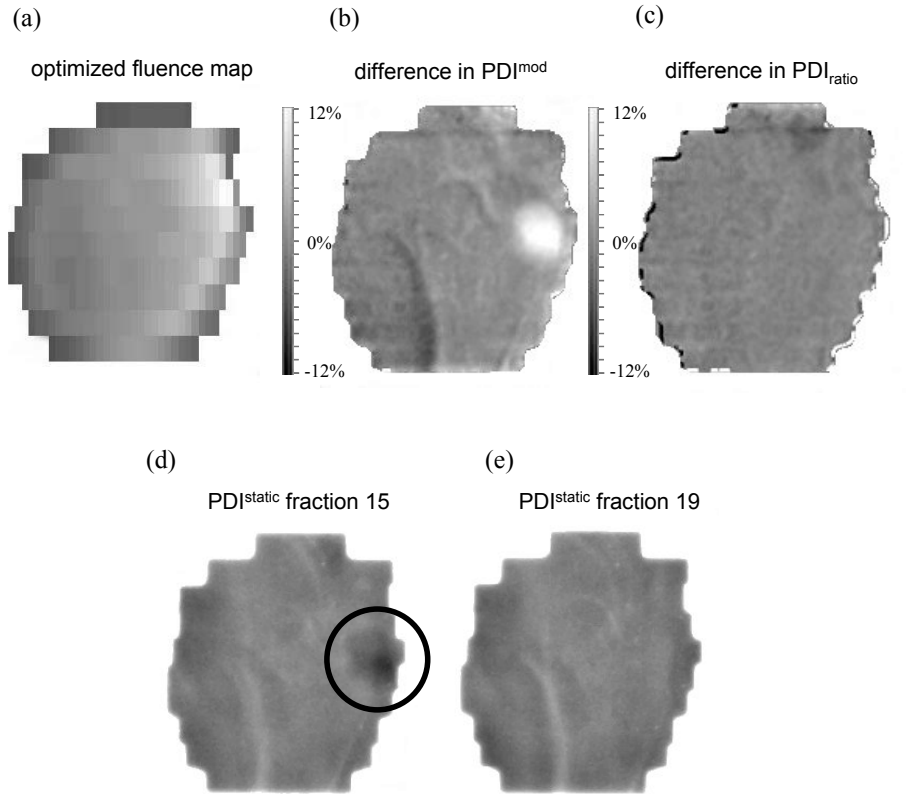


Figure 7-9 Fluence verification for the right lateral beam of a prostate cancer patient treated with the fluence map displayed in (a). Between treatment fractions 15 and 19, portal dose differences of up to 12% were observed in PDI^{mod} (b), while the PDI_{ratio} (c) was reproducible within $0.1 \pm 0.8\%$ (1SD). The differences in PDI^{mod} were due to the presence of a gas pocket in fraction 15 (indicated by a circle in (d)), which was absent in fraction 19 (e).

Our initial clinical results (15 patients) indicated that the largest deviations in measured PDIs occurred for head and neck cancer patients. This is mainly due to the fact that the treatment fields for these patients often include several air cavities and may also include the shoulder of the patient at the exit side of the beam. Moreover, for this tumor site, the radiological path length may change rapidly with position in the field. Therefore, a small change in alignment of the patient may already result in large deviations in the measured PDIs. Hence, the results shown in Fig. 7-10 and 7-11 are also representative clinical cases. Despite these changes, the IMRT fluence delivered by the treatment unit could be verified to within 1% using SIFT.

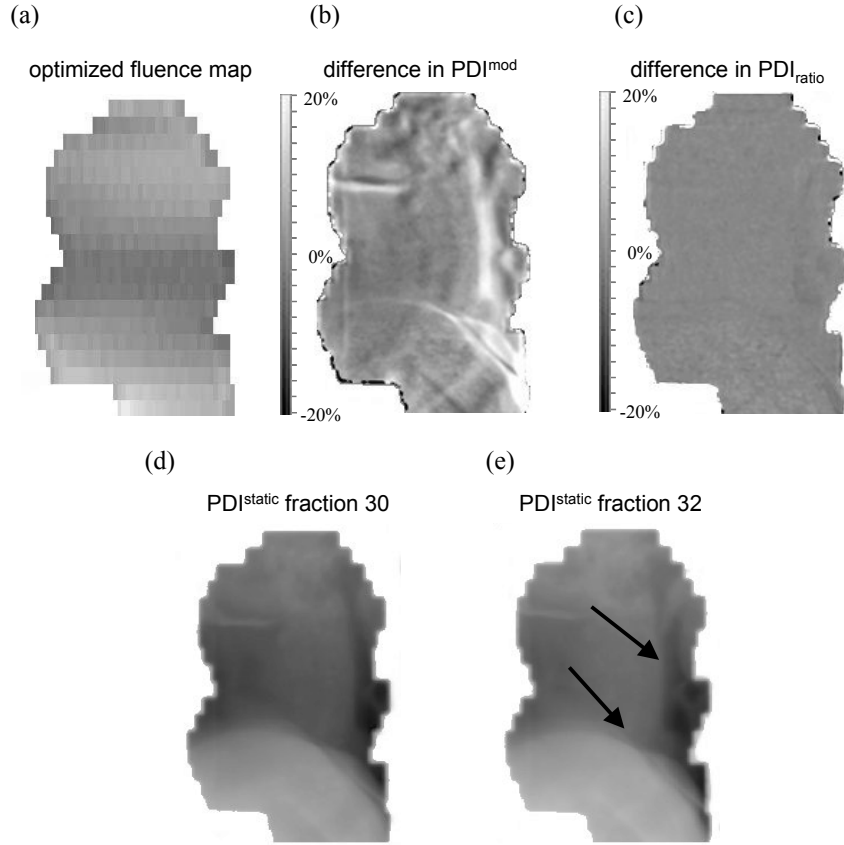


Figure 7-10 Fluence verification for the right lateral beam of a head and neck cancer patient. Between treatment fractions 30 and 32, portal dose differences of up to 20% were observed in PDI^{mod} (b), while the PDI_{ratio} (c) was reproducible within $0.6 \pm 0.9\%$ (1SD). Differences in PDI^{mod} could (in part) be explained by changes in the shoulder and trachea position, as visible when comparing the PDI^{static} of fraction 30 (d) and fraction 32 (e) (see arrows).

7.5 Discussion

It has been shown in a number of studies that electronic portal images are well suited for accurate transmission dose measurements during patient treatment.^{21, 22, 27, 28, 34, 35}

However, the measured PDIs are dependent on the delivered fluence and on the patient transmission. Unless the planning CT data is still valid during treatment delivery (i.e., the patient anatomy is completely static and no set-up errors occur), no

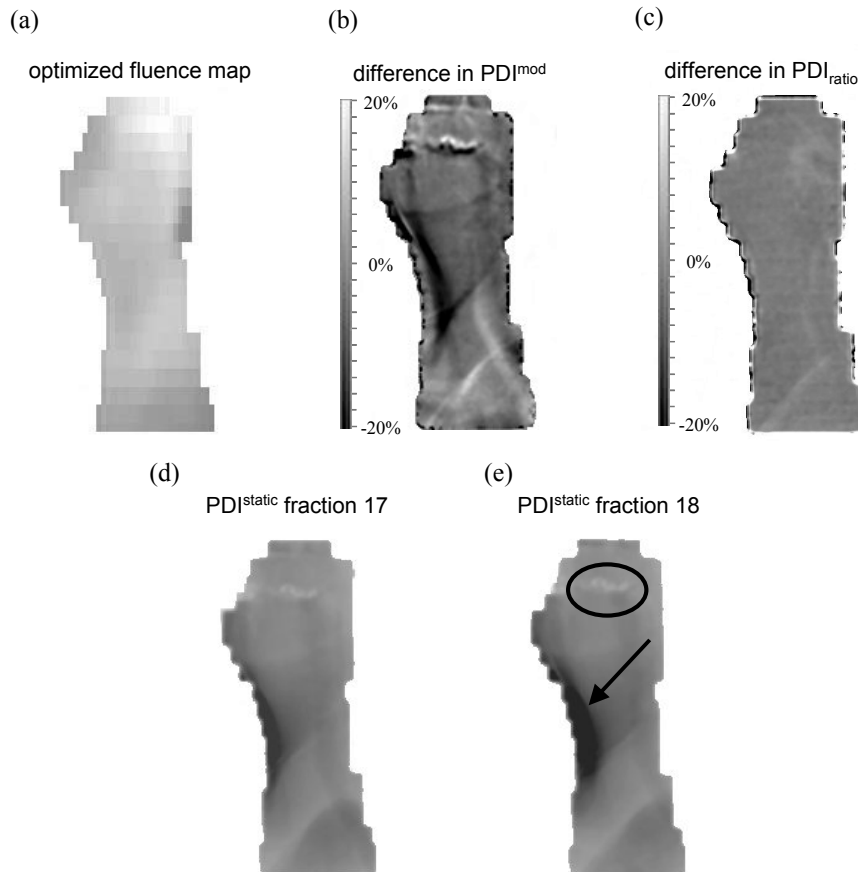


Figure 7-11 Fluence verification for the left lateral beam of a head and neck cancer patient. Between treatment fractions 17 and 18, portal dose differences of up to 20% were observed in PDI^{mod} (b), while the PDI_{ratio} (c) was reproducible within $-0.4 \pm 1.0\%$ (1SD). Differences in PDI^{mod} were (in part) attributed to changes in the position of the body contour and the patient teeth (indicated in (e) by an arrow and a circle, respectively), apparent when comparing the PDI^{static} of fraction 17 (d) and fraction 18 (e).

clear separation into fluence and patient geometry dependent effects is possible in a single image obtained during IMRT delivery.³⁶ In this paper, we have shown that SIFT can disentangle errors in the fluence delivery and patient geometry in a straightforward manner. To a high accuracy, the fluence of the modulated field can be derived by taking the ratio of the PDI of the modulated field and the PDI of the corresponding low exposure static field. Examples of phantom and patient measurements presented

in this paper show that using SIFT, the fluence can generally be verified within 1% (1SD). Only at small phantom to detector distances (<30 cm), the accuracy can be slightly reduced due to the increased scatter contribution. To achieve an even higher level of accuracy of fluence verification for small air gaps, the contribution of the scattered radiation to the EPID signal should be accounted for explicitly. This could be performed by using the portal dose prediction algorithm described elsewhere¹⁹ with the modulated incoming fluence. In this algorithm, the CT data of the patient (or the phantom) is converted into an equivalent homogenous phantom (EHP), which is then used to derive both the primary and the scatter contribution.

SIFT requires a high reproducibility of the EPID response over a wide range of signal heights. It was shown that our CCD-based EPID is meeting these requirements. The acquisition of the EPIs and the comparison of the acquired images can be performed using standard tools within our EPID software. In our present version of this software, the parameters and sequencing of the fields to be imaged can be completely configured, so that acquisition, processing and storing of both static and modulated field images for a large number of fields are performed automatically.

Using SIFT, the delivered IMRT fluence distribution can be reconstructed from the measured PDIs of the static and modulated field of the split IMRT field. If only the reproducibility of the delivered fluence needs to be checked, it is also possible to use EPIs instead of PDIs, which means that the applied dose calibration of the EPID^{12, 30} may not be required for SIFT. This is illustrated in Fig. 7-12 for introduced errors of 2%, 4%, and 15% in the delivered fluence, showing an agreement between the PDI_{ratio} and the EPI_{ratio} (the ratio of EPIs acquired for the modulated field and the static field) within 0.5%. Therefore, SIFT can be applied for fluence verification by any EPID user, as long as (i) the requirements for reproducibility of the EPID response, discussed in this paper, are met, and (ii) the EPID build-up plate renders this response insensitive to the changes in photon spectrum.^{12, 30}

Routine verification of the delivered fluence is an important first step in the QA of complex treatment delivery techniques, but the ultimate goal is to be able to accurately reconstruct the actual 3D dose distribution delivered to a patient. In case the internal organ motion is negligible, this dose reconstruction should be possible by using the fluence distribution derived with SIFT and the planning CT data corrected for the set-up errors derived from the low MU static fields. In order to derive these set-up errors, the use of an automated grey scale value match method between the low MU static field image and the predicted portal dose image is currently being investigated.

To assess the impact of this set-up error on the delivered dose to the patient, the 3D set-up error found is applied as a shift of the iso-center of the treatment plan. In this way, the actual delivered 3D dose distribution can be recalculated for each fraction. However, if internal organ motion is important (as shown by the example in Fig. 7-9), the deliv-

ered fluence derived using SIFT may, for instance, be combined with CT data acquired at the accelerator just before (or after) treatment³⁷⁻⁴⁰ to allow accurate dose reconstruction. Even then, changes in patient geometry may occur in the time interval between CT acquisition and the actual treatment, given the time required for the CT data acquisition and reconstruction. In these cases, SIFT offers an attractive and fast option to verify if these changes occurred, by comparing the measured PDI of the static field with the corresponding predicted PDI based on the CT data acquired at the treatment unit.

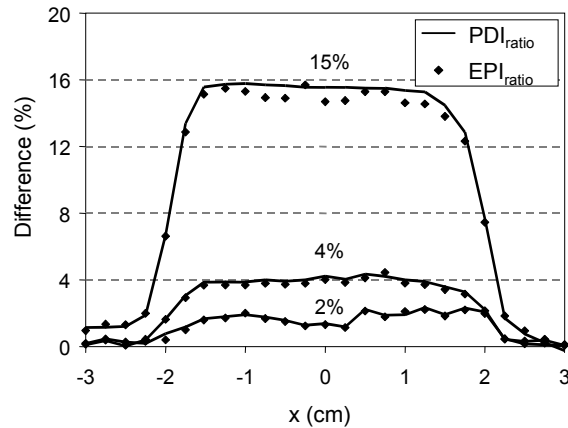


Figure 7-12 Difference in the PDI_{ratio} images (dashed line) and in the EPI_{ratio} images (diamonds) obtained with and without the errors of 2%, 4%, and 15% in the delivered fluence depicted in Fig. 7-8, in the absence of an absorber.

7.6 Conclusions

A technique for verification of the fluence delivered during patient treatment based on EPID measurements has been developed. Using SIFT, the delivered fluence can be verified within 1% accuracy, independent of (large) deviations in patient geometry. In fact, SIFT is capable of detecting fluence delivery errors smaller than 2%, even when the radiological path lengths change by 10 cm. In our department, SIFT is now used routinely in clinical practice for IMRT fluence verification without requiring a significant increase in treatment time.

7.7 Acknowledgments

The authors would like to thank Bert van Wijk for his efforts on implementing this verification method in clinical practice and Jaco Barnhoorn for developing software tools to analyze the EPID images. Financial support by 'Fundação para a Ciência e a Tecnologia' (project nº 21372 / 99) and by 'KWF kankerbestrijding' (project nº 2004–3107).

7.8 References

- ¹T. LoSasso, C. S. Chui, and C. C. Ling, "Comprehensive quality assurance for the delivery of intensity modulated radiotherapy with a multileaf collimator used in the dynamic mode," *Med. Phys.* **28**, 2209-2219 (2001).
- ²Intensity Modulated Radiation Therapy Collaborative Working Group (IMRTCWG), "Intensity modulated radiotherapy: current status and issues of interest," *Int. J. Radiat. Oncol. Biol. Phys.* **51**, 880-914 (2001).
- ³D. A. Low, "Quality assurance of intensity-modulated radiotherapy," *Semin. Rad. Oncol.* **12**, 219-228 (2002).
- ⁴G. A. Ezzell, J. M. Galvin, D. Low, et al., "Guidance document on delivery, treatment planning, and clinical implementation of IMRT: report of the IMRT Subcommittee of the AAPM Radiation Therapy Committee," *Med. Phys.* **30**, 2089-115 (2003).
- ⁵X. Wang, S. Spirou, T. LoSasso, et al., "Dosimetric verification of intensity-modulated fields," *Med. Phys.* **23**, 317-27 (1996).
- ⁶C. Burman, C. S. Chui, G. Kutcher, et al., "Planning, delivery, and quality assurance of intensity-modulated radiotherapy using dynamic multileaf collimator: a strategy for large-scale implementation for the treatment of carcinoma of the prostate," *Int. J. Radiat. Oncol. Biol. Phys.* **39**, 863-73 (1997).
- ⁷J. S. Tsai, D. E. Wazer, M. N. Ling, et al., "Dosimetric verification of the dynamic intensity-modulated radiation therapy of 92 patients," *Int. J. Radiat. Oncol. Biol. Phys.* **40**, 1213-30 (1998).
- ⁸D. A. Low, R. L. Gerber, S. Mutic, et al., "Phantoms for IMRT dose distribution measurement and treatment verification," *Int. J. Radiat. Oncol. Biol. Phys.* **40**, 1231-5 (1998).
- ⁹A. Van Esch, J. Bohsung, P. Sorvari, et al., "Acceptance tests and quality control (QC) procedures for the clinical implementation of intensity modulated radiotherapy (IMRT) using inverse planning and the sliding window technique: experience from five radiotherapy departments," *Radiother. Oncol.* **65**, 53-70 (2002).
- ¹⁰C. M. Ma, S. B. Jiang, T. Pawlicki, et al., "A quality assurance phantom for IMRT dose verification," *Phys. Med. Biol.* **48**, 561-72 (2003).
- ¹¹M. Partridge, P. M. Evans, A. Mosleh-Shirazi, et al., "Independent verification using portal imaging of intensity-modulated beam delivery by the dynamic MLC technique," *Med. Phys.* **25**, 1872-9 (1998).

-
- ¹²K. L. Pasma, M. Kroonwijk, J. C. J. de Boer, et al., "Accurate portal dose measurement with a fluoroscopic electronic portal imaging device for open and wedged beams and dynamic multileaf collimation," *Phys. Med. Biol.* **43**, 2047-2060 (1998).
- ¹³A. J. Curtin-Savard, and E. B. Podgorsak, "Verification of segmented beam delivery using a commercial electronic portal imaging device," *Med. Phys.* **26**, 737-42 (1999).
- ¹⁴K. L. Pasma, M. L. P. Dirkx, M. Kroonwijk, A. G. Visser, B. J. M. Heijmen, "Dosimetric verification of intensity modulated beams produced with dynamic multileaf collimation using an electronic portal imaging device," *Med. Phys.* **26**, 2373-8 (1999).
- ¹⁵H. V. James, S. Atherton, G. J. Budgell, et al., "Verification of dynamic multileaf collimation using an electronic portal imaging device," *Phys. Med. Biol.* **45**, 495-509 (2000).
- ¹⁶A. Van Esch, B. Vanstraelen, J. Verstraete, et al., "Pre-treatment dosimetric verification by means of a liquid-filled electronic portal imaging device during dynamic delivery of intensity modulated treatment fields," *Radiother. Oncol.* **60**, 181-90 (2001).
- ¹⁷J. Chang, G. S. Mageras, C. C. Ling, "Evaluation of rapid dose map acquisition of a scanning liquid-filled ionization chamber electronic portal imaging device," *Int. J. Radiat. Oncol. Biol. Phys.* **55**, 1432-45 (2003).
- ¹⁸S. C. Vieira, R. S. J. P. Kaatee, M. L. P. Dirkx, et al., "Two-dimensional measurement of photon beam attenuation by the treatment couch and immobilization devices using an electronic portal imaging device," *Med. Phys.* **30**, 2981-2987 (2003).
- ¹⁹K. L. Pasma, B. J. M. Heijmen, M. Kroonwijk, et al., "Portal dose image (PDI) prediction for dosimetric treatment verification in radiotherapy. An algorithm for open beams," *Med. Phys.* **25**, 830-840 (1998).
- ²⁰S. C. Vieira, M. L. P. Dirkx, K. L. Pasma, et al., "Fast and accurate leaf verification for dynamic multileaf collimation using an electronic portal imaging device," *Med. Phys.* **29**, 2034-2040 (2002).
- ²¹M. Kroonwijk, K. L. Pasma, S. Quint, et al., "In vivo dosimetry for prostate cancer patients using an electronic portal imaging device: demonstration of internal organ motion," *Radiother. Oncol.* **49**, 125-132 (1998).
- ²²K. L. Pasma, M. Kroonwijk, S. Quint, et al., "Transit dosimetry with an electronic portal imaging device (EPID) for 115 prostate cancer patients," *Int. J. Radiat. Oncol. Biol. Phys.* **45**, 1297-303 (1999).
- ²³J. C. Stroom, M. J. Olofsen-van Acht, S. Quint, et al., "On-line set-up corrections during radiotherapy of patients with gynecologic tumors," *Int. J. Radiat. Oncol. Biol. Phys.* **46**, 499-506 (2000).
- ²⁴H. C. de Boer and B. J. M. Heijmen, "A protocol for the reduction of systematic patient set-up errors with minimal portal imaging workload," *Int. J. Radiat. Oncol. Biol. Phys.* **50**, 1350-1365 (2001).
- ²⁵H. C. de Boer, J. R. van Sornsens de Koste, S. Senan, et al., "Analysis and reduction of 3D systematic and random set-up errors during the simulation and treatment of lung cancer patients with CT-based external beam radiotherapy dose planning," *Int. J. Radiat. Oncol. Biol. Phys.* **49**, 857-868 (2001).
- ²⁶H. C. de Boer, J. R. van Sornsens de Koste, C. L. Creutzberg, et al., "Electronic portal image assisted reduction of systematic set-up errors in head and neck irradiation," *Radiother. Oncol.* **61**, 299-308 (2001).
- ²⁷M. Essers, J. H. Lanson, G. Leunens, et al., "The accuracy of CT-based inhomogeneity corrections and in vivo dosimetry for the treatment of lung cancer," *Radiother. Oncol.* **37**, 199-208 (1995).

- ²⁸R. Boellaard, M. van Herk, H. Uiterwaal, et al., "First clinical tests using a liquid-filled electronic portal imaging device and a convolution model for the verification of the midplane dose," *Radiother. Oncol.* **47**, 303-12 (1998).
- ²⁹J. C. J. de Boer, J. C. Barnhoorn, B. J. M. Heijmen, "The CCD-camera based electronic portal imaging device (EPID) revisited; can a-Si flat panel EPIDs do better? (Abstr.)," *Radiother. Oncol.* **64**(2 Suppl):S12 (2002).
- ³⁰J. C. J. de Boer, B. J. M. Heijmen, K. L. Pasma, et al., "Characterization of a high elbow, fluoroscopic electronic portal imaging device for portal dosimetry," *Phys. Med. Biol.* **45**, 197-216 (2000).
- ³¹P. Munro and D. C. Bouius, "X-ray quantum limited portal imaging using amorphous silicon flat-panel arrays," *Med. Phys.* **25**, 689-702 (1998).
- ³²S. C. Vieira, M. L. P. Dirkx, K. L. Pasma, et al., "Dosimetric verification of x-ray fields with steep dose gradients using an electronic portal imaging device," *Phys. Med. Biol.* **48**, 157-166 (2003).
- ³³J. C. Stroom, P. C. M. Koper, G. A. Korevaar, et al., "Internal organ motion in prostate cancer patients treated in prone and supine treatment position," *Radiother. Oncol.* **51**, 237-248 (1999).
- ³⁴J. W. Wong, E. D. Slessinger, R. E. Hermes, et al., "Portal dose images. I: Quantitative treatment plan verification," *Int. J. Radiat. Oncol. Biol. Phys.* **18**, 1455-63 (1990).
- ³⁵M. C. Kirby and P. C. Williams, "The use of an electronic portal imaging device for exit dosimetry and quality control measurements," *Int. J. Radiat. Oncol. Biol. Phys.* **31**, 593-6 (1995).
- ³⁶V. N. Hansen, P. M. Evans, W. Swindell, "The application of transit dosimetry to precision radiotherapy," *Med. Phys.* **23**, 713-721 (1996).
- ³⁷K. Nakagawa, Y. Aoki, M. Tago, et al., "Megavoltage CT-assisted stereotactic radiosurgery for thoracic tumors: original research in the treatment of thoracic neoplasms," *Int. J. Radiat. Oncol. Biol. Phys.* **48**, 449-457 (2000).
- ³⁸J. M. Kapatoes, G. H. Olivera, K. J. Ruchala, et al., "A feasible method for clinical delivery verification and dose reconstruction in tomotherapy," *Med. Phys.* **28**, 528-542 (2001).
- ³⁹D. A. Jaffray, J. H. Siewerdsen, J. W. Wong, et al., "Flat-panel cone-beam computed tomography for image-guided radiation therapy," *Int. J. Radiat. Oncol. Biol. Phys.* **53**, 1337-1349 (2002).
- ⁴⁰M. Partridge, M. Ebert, and B. M. Hesse, "IMRT verification by three-dimensional dose reconstruction from portal beam measurements," *Med. Phys.* **29**, 1847-1858 (2002).

CHAPTER 8. GENERAL DISCUSSION

8.1 Introduction

In the last decade, radiotherapy has seen many advances. MRI and positron emission tomography (PET) have been introduced to improve tumour delineation, while new delivery techniques such as intensity modulated radiotherapy (IMRT), Tomotherapy, robotic radiosurgery (Cyberknife), and intensity modulated arc therapy (IMAT) allow delivery of highly conformal dose distributions.¹⁻⁵ Progress has also been made in the area of image guided delivery of the daily treatment fractions (IGRT) for reduction of geometrical errors. Image quality of electronic portal imaging devices (EPID) has greatly improved and very efficient protocols for patient set-up correction are now in clinical use.^{6,7} The standards for quality control did not always accompany these developments; the first extensive reports on quality assurance for IMRT appeared in 2000,^{8,9} five years after the introduction of IMRT in clinical practice. The published IMRT quality assurance protocols usually rely on dosimetric measurements with film, TLD, diode or ionisation chamber;⁸⁻¹⁷ an EPID is seldom mentioned in these QA protocols. Our aim was to develop and clinically implement a quality assurance protocol for IMRT with a faster and more robust approach to what other protocols proposed so far. Furthermore, we wanted to use solely a CCD-camera based EPID for the measurements.

8.2 Dosimetry with a CCD-camera based EPID

Compared to conventional methods for dosimetric QA of IMRT, EPIDs have several advantages. Because there is virtually no set-up time, and the EPIDs are fast in collecting information, these devices are quite suitable for daily routine QA and for patient measurements. If the EPID is already used for patient positioning verification, no extra equipment is needed. Point measurements are not suited for a full dosimetric verification of an intensity modulated field. In contrast to point detectors (such as diodes, TLDs, MOSFETs, and ionisation chambers), EPID dosimetry generates immediate, 2-dimensional (2D) digital information. Film dosimetry delivers a 2D dosimetric dataset. However, to obtain digital data for analyses, the film first has to be processed and scanned. Also, with TLD, the detector material needs processing to

obtain dosimetrical data. Hence, both for film and TLD there is no immediate access to the data. Apart from the labour involved in processing/scanning, the delay in availability of the data may also be a disadvantage for in-vivo dosimetry. An EPID naturally facilitates 2D dosimetry at any gantry angle. Film dosimetry at arbitrary gantry angles has the practical, non-trivial problem of accurately positioning the film. 2D information can only be challenged by the complete 3D information available when using gel dosimetry. However, it is not realistic to employ the latter for every patient because it is very expensive and time consuming. Gel dosimetry has also difficulties with low density media which are currently being investigated.¹⁸ Moreover, it cannot be used for in-vivo measurements and the applied phantoms do generally not resemble the exact anatomy of the individual patient.

Diodes and TLDs are known absolute dosimeters, especially used when the patient is involved, i.e., as *in vivo* detectors.^{10,14,17,19} Generally, point detectors such as TLD and diodes are used for patient entrance measurements. The interpretation of measured exit doses may be troublesome: the exit detector may be shielded by the entrance detector, the position of the exit detector relative to the patient anatomy is not well defined, and the (internal) patient anatomy may have changed relative to the planning CT-scan. In order to overcome some of these problems, Essers *et al.*⁵⁴ have used the EPID to visualise the position of the diodes.

The impact of a changed patient anatomy on measured transmission doses is illustrated in Fig. 8-1 for a prostate patient irradiated with 3DCRT.²⁵ The graph shows differences

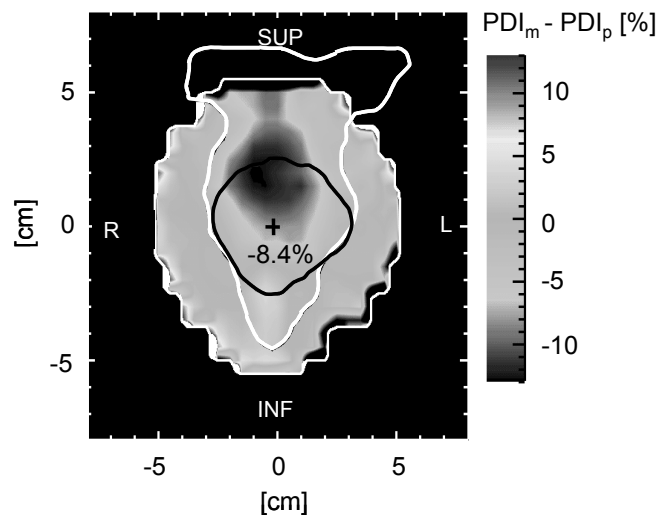


Figure 8-1 2D difference map between the measured PDI (PDI_m) and the predicted PDI (PDI_p) of a rectum cancer patient. The cross indicates the diode measurement performed for the same patient. The white and the black contour represent the rectum and the gross tumour volume, respectively, as delineated in the planning CT scan.

between absolute portal doses measured with our EPID and portal doses predicted using the planning CT-scan of the patient. Dose was delivered with a static, open field. For the largest part of the field, the difference between measurement and prediction is negligible. However, there is an area with differences of more than 10%; the on-axis value is -8.4% . Due to availability of the 2D data presented in Fig. 8-1, we could conclude that the large dose differences were caused by rectal filling at the time of treatment that was absent during acquisition of the planning CT-scan. The large zero-difference area proves that the dose delivery by the linac was as prescribed. A transmission measurement with only an on-axis point detector (no EPID present) would not have allowed to discriminate between linac errors and patient anatomy changes.

Over the last decade, significant advances in the development of EPIDs took place,²² and CCD camera-based EPIDs are no exception. Cooling of the CCD now prevents fast degradation of image quality due to radiation damage, and therefore allows for sparse camera replacement and dosimetric recalibration of the EPID. The oldest system in our institute with a cooled camera is in use for over three years on a dual energy machine (6 and 23 MV) without any sign of image degradation due to radiation damage. The short-term dosimetric response stability of cooled CCD-camera systems is 0.2% (1 SD) and the long term stability (130 day period) is 0.4% (1 SD).²³ The systems are linear with respect to delivered MU, and independent of dose rate. The available algorithm for conversion of measured pixel values into absolute portal doses has an accuracy typically better than 2-3%. Our current CCD-camera based EPID is effectively an array of 1280×1240 simultaneously integrating dosimeters and has a dead time in between acquired frames of only 0.1 ms. The latter allows for almost complete acquisition of the EPID signal, which is particularly important for dosimetry. This renders the detector suited for verification of intensity modulated fields delivered with dynamic multi-leaf collimation.^{20,50} Larger deviations may occur in small off-axis fields, related to the use of an invariant kernel to describe optical cross talk.^{26,53} A new algorithm for conversion of pixel values into portal doses is now being developed at our institute, based on the measurement of cross talk kernels in each point of the image. The first results regarding dosimetric accuracy are very promising.²⁴ Regarding dosimetric precision and recalibration, the CCD camera based EPID compares favourably with more conventional dosimetric tools.^{12,17,21}

EPIDs can of course not be used to measure directly in the phantom measurements. In Rotterdam it was decided to use a fully redundant 3D Monte Carlo dose calculation algorithm to check the dose calculations by the TPS (as mentioned in section 8.4.3).

EPIDs are only used to verify correct execution of the planned treatment parameters, such as fluences, collimator angles and patient isocenter. The redundant dose calculation avoids measurement in a phantom that does not resemble the patient anatomy, and also avoids the development of a back-projection algorithm, and some disadvantages related to back-projection (see below).

8.3 Current status of dosimetry with commercial flat-panel systems

The main alternative for CCD camera-based EPIDs are the flat panel EPID detectors, which are available commercially since 2000. The aim of these new developed detectors was to offer a better image quality, high optical transfer efficiency, large imaging area, and resistance to radiation with respect to the existing EPIDs.^{22,27} Since then studies have been performed to assess the characteristics of the flat panel EPID as a tool for patient position and dosimetric verification.^{22,27-37} In this chapter, solely the aspects relevant for dosimetry are discussed.

High reproducibility of the dosimetric response is a major prerequisite for an EPID to be used for dosimetric IMRT verification. Recently, Louwe *et al.*³⁵ reported a long-term reproducibility of 0.5% (1 SD) over a 23 months period for several beam energies using a flat panel imager Elekta iViewGT (Elekta Oncology Systems Ltd., Crawley, United Kingdom). Other authors found a reproducibility of about 1% (1 SD), using the flat panel EPID from another manufacturer in a 6 MV beam.^{29,31,36} Additionally, Menon *et al.*³⁶ reported a reproducibility of 4% over the same period for the 15 MV beam using a flat panel detector aS500 (Varian Associates, Palo Alto, CA), concluding that more frequent verification of the EPID calibration for this energy was needed. The long-term reproducibility of the cooled CCD camera-based EPID used in this thesis (0.4% (1 SD))²³ is comparable to the stability reported by Louwe *et al.*³⁵ for the flat panel system. For flat panel detectors, radiation damage seems to be a serious issue.³⁵ Regular replacement of the flat panel imagers is required because of instability in the individual image segments and overall degradation in image quality.

Flat panel EPIDs are reported to be linear with dose rate.²⁸⁻³¹ Linearity with dose varies with energy and with field size;^{28,29,31} the latter can be in the order of 5-6% relative to the ionisation chamber measurements for field sizes ranging from about 4×4 to 24×24 cm².^{28,29} This dependence has to be included in the calibration of the flat panel and may be significantly dependent on the type of imager used, or even between

imagers with similar design.³² Additionally, the presence of optical scatter within the flat panel layer, also known as "glare", has been detected.^{30,34} This scatter is also present in other types of EPIDs (including the CCD camera-based used in this thesis), although in the case of the flat panels is much smaller.²² Nevertheless, it needs to be considered in the calibration for accurate dosimetry.

Another reported aspect relative to the flat panels, and not observed in other EPID types, is the long-term image persistence (or "ghosting").^{32,33} Siewerdsen *et al.*³³ found that the image of their prototype persisted more than 30 minutes, depending upon the exposure and frame time. Using a commercially available flat panel (Elekta iViewGT), McDermott *et al.*³² found that, when using IMRT fields for beams prescribed with 5 to 50 MU, the EPID response could vary by 3% if no corrections for ghosting effects were applied. Results also indicated that ghosting in the signal after irradiation might depend on beam time and not dose or dose-rate. Other authors did not find evidence of relevant ghosting in clinical situations,^{31,37} although measurement of the ghosting effect was recommended because it could vary with panel design.³⁷

The dead time in between acquisition of subsequent frames is also reported to cause errors, when using a flat panel detector aS500 for verification of IMRT.²⁹ As a result of this dead time, the observed error in the flat panel detector signal was over 20% for a 1 cm leaf gap moving at 1.0 cm s⁻¹. This may pose a problem for the use of DMLC IMRT. However, Sonke *et al.*³⁷ have used the flat panel Elekta iViewGT to verify leaf trajectories during dynamic IMRT, when using an image acquisition procedure developed in their institute.

During the signal integration or readouts, saturation may occur.³¹ This saturation occurs more predominantly when the flat panel is positioned closely to the isocenter (SDD=105 cm), combined with high dose rates (600 MU/min). Introduced errors in the flat panel signal can be up to 25%.

Flat panels have been used for pre-treatment verification in clinical practice using SMLC and DMLC IMRT using different evaluation criteria and flat panel designs.^{31,34} For SMLC, the flat panel shows good agreement with film, with a mean dose difference between three IMRT treatments (24 fields) of $0.2 \pm 1.0\%$.³⁴ For DMLC, gamma evaluations of the predicted versus measured portal dose distribution were within the pre-defined acceptance criteria for all clinical IMRT fields, i.e. allowing a dose difference of 3% of the local field dose in combination with a distance to agreement of 3 mm.³¹

8.4 Dosimetric quality assurance protocols for IMRT

In this paragraph protocols proposed for dosimetric QA of IMRT are discussed. An aspect common to most protocols is the routine check of the accelerator, aimed mainly at MLC performance. These (monthly) checks are generally performed using film and ionisation chamber; off-axis positions are normally performed annually using similar procedures.^{12,13,17} In Rotterdam, we have developed a fast procedure for *daily* linac QA (chapter 5). This procedure to verify the linac output and leaf motion is performed each morning by the technicians of the treatment unit, prior to treatment of the first patient. The involved acquisition of EPID images and (automatic) image analysis takes less than 2 minutes. The applied software has been integrated in the commercially available Theraview NT package. Measured errors smaller than 0.5 mm are accepted. For deviations between 0.2 mm and 0.5 mm, the particular leaf pair is automatically labelled with the word “warning” in the log file. If the deviation persists in subsequent checks, the physicist informs the accelerator maintenance engineers. Preventive cleaning or replacement of components may then be performed to avoid MLC problems occurring during future treatments.

For one of the accelerators, during a period of 15 months (since January 2004), the log files from the accelerator maintenance were compared with the log files provided by this linac QA procedure. Despite the monthly checks by the service engineer, a total of 3 errors/warnings was found leading to a leaf recalibration and/or replacement of leaf components. One systematic error in all leaves of 0.3 mm was found by this MLC check after the leaves had been calibrated during accelerator maintenance. Another error was detected by the MLC check caused by the malfunctioning of the motor of one leaf, which was then replaced. Finally, a warning state measured by the MLC check lead to a motor replacement of one leaf. The latter probably prevented a problem with MLC to occur during the treatment day. Recently, the MLC check has been changed and now is performed with gantry angle at 270° instead of 0°. The reason for this change in procedure is to study if the use of a more demanding position (due to gravity) will lead to an increase in the detection of errors. This change was triggered by the fact that an error on a leaf motion was found during treatment, which had not been detected by the MLC test performed in that morning. Future changes in the MLC check will include also variations on the leaf gap speed.

The following subsections focus on QA protocols for *individual* patients, complementary to the linac QA.

8.4.1 Common approaches for individualised QA of IMRT

A common approach to check an IMRT treatment consists of three steps: (1) the verification of the MU calculation, (2) the verification of the data transfer from the treatment planning system to the accelerator, and (3) the treatment delivery.^{8,9,12,13} In the first step, the MU check is recommended to be performed by independent software. In the second step, the correct transcription of IMRT delivery parameters, such as leaf sequences and MUs, is often tested using a phantom plan methodology. This methodology includes a pre-treatment calculation of the dose in a standard phantom (regular geometry or anthropomorphic) using the MLC segments, leaf trajectories and MU of each IMRT field intended to be delivered to the patient. The phantom is irradiated and the dose is measured with ion chambers, film, or other detectors.^{10,12,14-17,26,39} The measured dose is compared with the corresponding calculated dose. If point detectors are used, film measurements may additionally be performed to verify the dose distribution in 2D.¹² The action level for these measurements is usually 3% to 4% in high dose and low gradient regions. Finally, at the time of treatment, *in vivo* dosimetry measurements are generally performed using diodes or TLDs.^{10,14,17}

Phantom measurements may be used to detect errors in the transfer of treatment parameters from the treatment planning system (TPS) to the treatment unit. Generally, a homogeneous, regularly shaped phantom is used, and the dose distribution in the phantom is not expected to be the same as in the patient. Therefore, these measurements do not allow complete verification of the TPS dose calculations for the (highly inhomogeneous) patient. Moreover, point measurements and 2D film measurements offer only partial verification of the full 3D dose distribution. Additionally, when anthropomorphic phantoms are used in combination with point detectors to verify the dose distribution, positioning of the detectors may be difficult, implying a less accurate verification.^{38,39} Another situation where the phantom measurements are not sufficient to verify the calculated dose is when the TPS includes the CT couch as part of the patient.⁹ In this case, several centimetres may be added to the radiological depths, and the corresponding beam intensities may be increased accordingly. When performing the phantom check, those intensities are applied to the phantom and match the phantom measurements. This type of error would probably only be discovered by performing 2D *in vivo* measurements.

8.4.2 Patient dose reconstruction using back-projection methods

As an alternative to the combined use of the MU-check, the pre-treatment phantom measurements, and *in vivo* point measurements for dosimetric IMRT verification, portal dose back-projection methods (i.e. a 2D or 3D dosimetric reconstruction inside the patient) have been investigated. Common to all published back-projection procedures is that measured portal doses *behind* the patient are used to derive the dose distribution delivered *inside* the patient.⁴⁰⁻⁴³ A prerequisite for accurately deriving the patient dose distribution by back-projecting portal doses is the knowledge of the patient geometry (set-up and (internal) anatomy) *at the time of treatment*, which may differ from the geometry during acquisition of the *planning* CT-scan. As mentioned in chapter 7, observed large variations in measured portal dose may be due to patient geometry and set-up variations. For prostate cancer patients, large internal anatomy variations have been observed due to gas pockets in the rectum of the patients.^{25,51} When using the *planning* CT-scan for back-projection, large errors may appear in the derived patient dose distribution that are either due to differences in the actual patient geometry, or due to fluence delivery errors by the linear accelerator. The SIFT method described in chapter 7 was developed to at least discriminate between these errors. However, also SIFT does not solve the problem of 3D interpretation of anatomy deviations in 2D portal images.

Exact knowledge of the patient geometry during treatment may be obtained using a CT device at the treatment unit.⁴⁴⁻⁴⁹ Nakagawa *et al.*⁴⁴ used MVCT in patient treatment as a positioning verification tool and as a real time monitoring of field position relative to the tumour site. But due to the high dose delivered with their MVCT approach, daily use of this technique appears hardly possible. Welsh *et al.*⁴⁸ used helical tomotherapy to generate CT images of the patient position from the treatment megavoltage radiation. MVCT images of 10 patients with non-small-cell lung cancer (NSCLC) were acquired. It was stated that further studies are needed to optimise MVCT imaging and better define its utility in patients with NSCLC. Siewerdsen *et al.*⁴⁹ evaluated the image quality obtained from scanning 8 patients with the kilovoltage cone-beam CT mounted on the accelerator. It was concluded that X-ray scatter was one of the largest physical limitations for image quality of the cone-beam CT. The image quality could be improved by using a large air gap and by exposing only what was needed to be visualised. The potential advantage of the cone-beam CT with respect to the MVCT is the use of kilovoltage beams. This allows better visualisation of soft tissue, and therefore may offer the possibility in a near future for 3D reconstruction of the dose delivered to the tumour and organs at risk.

8.4.3 The Rotterdam approach for IMRT quality assurance

The Rotterdam protocol for individualised dosimetric QA has two main components, one for verification of the 3D dose calculations of the applied TPS, the other to check treatment execution. The idea behind this protocol is that if (i) the patient dose distribution calculated for the established treatment parameters such as gantry angles, leaf trajectories, position of patient isocenter, etc. is correct; and (ii) the treatment is indeed delivered according to the established parameters, dose delivery to the patient is according to the plan as approved by the physician.

8.4.3.1 Dose calculation verification

Currently, for each patient a fully independent dose calculation is performed for a single point in the center of the tumour, using the treatment parameters (such as patient set-up and leaf settings), as established by the TPS. The treatment plan is accepted if the difference with the corresponding TPS dose is smaller than 5%. Work is in progress to replace this independent point dose calculation by a 3D Monte Carlo dose calculation. Compared to the phantom measurements described in section 8.4.1, the 3D dose calculation does allow for an exact verification of the full dose distribution expected in the patient. In contrast to the back-projection methods described in section 8.4.2, the calculation does not suffer from a changed patient anatomy, as both the TPS calculations and the redundant dose calculations are performed using the planning CT-scan.

8.4.3.2 Treatment execution verification

Treatment execution verification has two steps, involving pre-treatment EPID measurements, and in-vivo measurements. The pre-treatment measurements are performed to check the proper transfer of the treatment parameters from the TPS to the linac, prior to the first treatment fraction of the patient. It also ensures that, at least just before the first treatment fraction, the execution of the plan by the linac was correct, including delivery of the correct absolute fluence profiles. For each treatment beam, an EPID image is acquired during full IMRT delivery in absence of the patient; beams are delivered at the planned clinical gantry angles. This image is then converted into a portal dose image (PDI, an absolute 2D dose distribution at the plane

of the fluorescent screen of the EPID), which is compared with the PDI predicted by the TPS.⁵⁰ Disagreement between measured and predicted PDIs indicates discrepancies between beam parameters realised by the linac and the ones used by the TPS. If dose differences larger than 5% are detected, further investigations are performed. These additional ionisation chamber measurements are rare (once or twice per year). Pre-treatment verification with the EPID is now standard for all our IMRT patients. In around 200 checked patients, serious errors were found in two cases. In one case, the wrong treatment plan was imported for treatment. In the second case, the trajectory of one leaf was too slow during delivery.

For all IMRT patients, EPID images for static fields are acquired during the first treatment fractions for patient set-up verification. Another reason for acquiring these fields is that a relatively large difference in source-to-patient skin distance does translate in only a minor difference in measured portal dose. The no action level (NAL) off-line protocol is applied for set-up corrections, aiming at reducing the systematic errors.⁷ Set-up corrections may be based on bony anatomy shifts or on displacements of implanted fiducials. For some patient groups, EPID-images are also acquired for all IMRT fields during each fraction to verify treatment execution. These images are then acquired using the SIFT technique for delivery of the fields (see chapter 7). In the present version of our EPID software, acquisition, processing and storing of both static and modulated field images are performed automatically. This allows for SIFT to be performed every treatment day without significantly increasing the workload at the treatment unit. The purpose of SIFT is the accurate verification of the delivered fluence profiles, independent of changes in patient anatomy. SIFT has revealed that the sometimes large portal dose differences ($\sim 15\%$) should generally be attributed to patient anatomy variations. This phenomenon is being investigated in ongoing studies.

Since SIFT may be used to accurately verify the delivered IMRT fluence profiles, one can argue that the pre-treatment check may no longer be necessary. The latter would mean less workload, but occurring errors would only be discovered after the patient had been irradiated in the first fraction. In view of the serious errors found with the pre-treatment measurements, it has been decided to continue performing these measurements for each individual patient. In order to improve our procedures further, studies are being prepared to investigate the role, value and need of cone beam CT procedures for dosimetric QA of IMRT in the various patient categories.

8.5 Is validation of individual IMRT treatments necessary?

The choice for individualised QA for all our IMRT patients was made in view of the characteristics of IMRT, and the demand that this technique poses on the user and the equipment. Although one can argue that a lot of the sources of error can be checked by performing a proper commissioning of both the accelerator and the software used,⁵² human errors, remaining software errors, and mechanical errors, among others, cannot be excluded.

As mentioned previously, with our pre-treatment verification serious errors were found in 2 of around 200 checked patients. In one case, an (human) error occurred in the transfer of an IMRT file from the TPS to the linac, which was detected by the pre-treatment check (see Fig. 8-2). In this particular case, two IMRT plans were transferred to the record and verify system, both approved by the physician, but the wrong plan was imported for treatment. It was not clear which plan to import because of non-standard plan number terminology. The detection of this error, only possible with individualised QA, indicated a “leak” in our QA protocol, which, after being discovered, could easily be solved and incorporated in our treatment procedure. Perhaps there is a possibility of relying entirely on a good commissioning procedure. However, first an extensive evaluation must be made of the problems that occur in clinical practice. This should be performed by the institutions applying individualised QA. Nevertheless, other errors, like mechanical failures of the accelerator, which

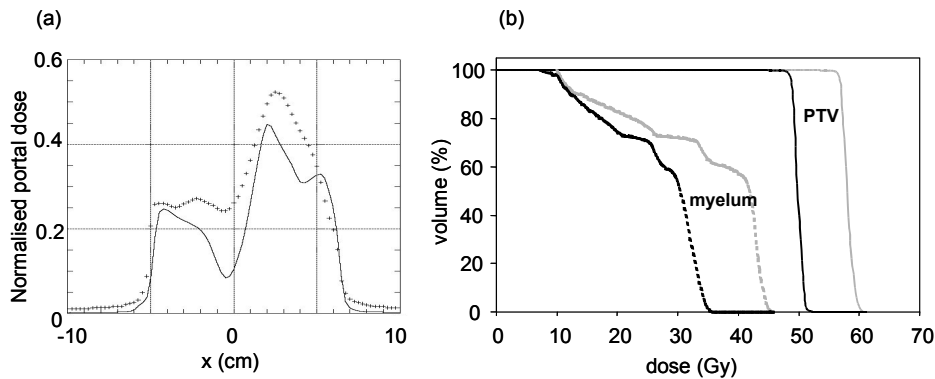


Figure 8-2 Error found during the pre-treatment check. (a) Difference between the calculated (plus) and the measured (line) portal dose profile. (b) Difference in the dose volume histogram for the PTV (line) and the myelum (dashed line), when using the corrected plan (black line) and the erroneous plan (grey line).

cannot be predicted, will remain. Moreover, if patient complications arise from the IMRT treatment, individualised QA is the only way to have a record of the treatment of that particular patient, and the sole, direct proof that the patient was treated according to plan.

An important point for not performing individualised QA is the time and workload it implies.⁵² This is understandable if point-detectors, gel or films are used, but with the EPID the argument holds less ground. Based on our findings, we think that individualised QA is indeed necessary to guarantee proper dose delivery to our patients. With the procedures and technology described in this thesis and summarized in section 8.4.3, redundancy in QA may be avoided, and the workload may be kept acceptable. More automation in some procedures, especially in data analysis, may further reduce this workload.

8.6 Conclusions

The introduction of IMRT in clinical practice is a challenge for any hospital. A major issue is adequate QA of the high precision-high dose treatments with a feasible amount of human resources. Therefore fast verification procedures and strategies have to be implemented in order to meet this challenge. An important part of this thesis was aimed at the development of an automated protocol exclusively dedicated to IMRT verification. This protocol was implemented in clinical practice making it available for all IMRT patients, i.e., not only for a group of research patients. The tools used in the protocol are accurate and user friendly. Another novelty of this thesis was the decision to use the EPIDs throughout the protocol, hence replacing the standard detectors used in radiotherapy: ionisation chamber and films. Only due to the development of EPID-based procedures, the required high level of treatment verification could be realized with the available manpower. Using EPIDs, much faster (2D) measurements can be performed offering the possibility to perform individual patient QA on a routine basis. Presently, many data on patient delivery and accelerator performance is being measured in our institution, which will be used to further improve our QA protocol in the future.

8.7 References

- ¹T. R. Bortfeld, D. L. Kahler, T. J. Waldron, and A. L. Boyer, "X-ray field compensation with multileaf collimators," *Int. J. Radiat. Oncol. Biol. Phys.* **28**, 723-30 (1994).

- ²D. J. Convery and M. E. Rosenbloom, "Treatment delivery accuracy in intensity-modulated conformal radiotherapy," *Phys. Med. Biol.* **40**, 979-99 (1995).
- ³J. R. Adler Jr, S. D. Chang, M. J. Murphy, J. Doty, P. Geis, and S. L. Hancock SL, "The Cyberknife: a frameless robotic system for radiosurgery," *Stereotact. Funct. Neurosurg.* **69**, 124-8 (1997).
- ⁴T. R. Mackie, J. Kapatoes, K. Ruchala, W. Lu, C. Wu, G. Olivera, L. Forrest, W. Tome, J. Welsh, R. Jeraj, P. Harari, P. Reckwerdt, B. Paliwal, M. Ritter, H. Keller, J. Fowler, and M. Mehta, "Image guidance for precise conformal radiotherapy," *Int. J. Radiat. Oncol. Biol. Phys.* **56**, 89-105 (2003).
- ⁵W. Duthoy, W. De Gersem, K. Vergote, T. Boterberg, C. Derie, P. Smeets, C. De Wagter, and W. De Neve, "Clinical implementation of intensity-modulated arc therapy (IMAT) for rectal cancer," *Int. J. Radiat. Oncol. Biol. Phys.* **60**, 794-806 (2004).
- ⁶A. Bel, M. van Herk, H. Bartelink, and J. V. Lebesque, "A verification procedure to improve patient set-up accuracy using portal images," *Radiother. Oncol.* **29**, 253-60 (1993).
- ⁷H. C. de Boer and B. J. M. Heijmen, "A protocol for the reduction of systematic patient set-up errors with minimal portal imaging workload," *Int. J. Radiat. Oncol. Biol. Phys.* **50**, 1350-1365 (2001).
- ⁸Intensity Modulated Radiation Therapy Collaborative Working Group (IMRTCWG), "Intensity modulated radiotherapy: current status and issues of interest," *Int. J. Radiat. Oncol. Biol. Phys.* **51**, 880-914 (2001).
- ⁹G. A. Ezzell, J. M. Galvin, D. Low, J. R. Palta, I. Rosen, M. B. Sharpe, P. Xia, Y. Xiao, L. Xing, and C. X. Yu; IMRT subcommittee; AAPM Radiation Therapy committee, "Guidance document on delivery, treatment planning, and clinical implementation of IMRT: report of the IMRT Subcommittee of the AAPM Radiation Therapy Committee," *Med. Phys.* **30**, 2089-115 (2003).
- ¹⁰C. Burman, C. S. Chui, G. Kutcher, et al., "Planning, delivery, and quality assurance of intensity-modulated radiotherapy using dynamic multileaf collimator: a strategy for large-scale implementation for the treatment of carcinoma of the prostate," *Int. J. Radiat. Oncol. Biol. Phys.* **39**, 863-73 (1997).
- ¹¹C. B. Saw, K. M. Ayyangar, W. Zhen, R. B. Thompson, and C. A. Enke, "Commissioning and quality assurance for MLC-based IMRT," *Med. Dosim.* **26**, 125-33 (2001).
- ¹²T. LoSasso, C. S. Chui, and C. C. Ling, "Comprehensive quality assurance for the delivery of intensity modulated radiotherapy with a multileaf collimator used in the dynamic mode," *Med. Phys.* **28**, 2209-2219 (2001).
- ¹³D. A. Low, "Quality assurance of intensity-modulated radiotherapy," *Semin. Rad. Oncol.* **12**, 219-228 (2002).
- ¹⁴J. S. Tsai, D. E. Wazer, M. N. Ling, et al., "Dosimetric verification of the dynamic intensity-modulated radiation therapy of 92 patients," *Int. J. Radiat. Oncol. Biol. Phys.* **40**, 1213-30 (1998).
- ¹⁵C. M. Ma, S. B. Jiang, T. Pawlicki, et al., "A quality assurance phantom for IMRT dose verification," *Phys. Med. Biol.* **48**, 561-72 (2003).
- ¹⁶S. L. Richardson, W. A. Tome, N. P. Orton, T. R. McNutt, and B. R. Paliwal, "IMRT delivery verification using a spiral phantom," *Med. Phys.* **30**, 2553-8 (2003).
- ¹⁷P. D. Higgins, P. Alaei, B. J. Gerbi, and K. E. Dusenbery, "In vivo diode dosimetry for routine quality assurance in IMRT," *Med. Phys.* **30**, 3118-23 (2003).
- ¹⁸C. Wagter, K. Vergote, C. Martens, L. Paelinck, S. Gillis, Y. De Deene, and W. De Neve, "Dosimetric verification as the ultimate QA test for the complete planning and delivery chain of IMRT," *Klinische Fysica*, 34-36 (2002).

- ¹⁹P. A. Jursinic, "Implementation of an in vivo diode dosimetry program and changes in diode characteristics over a 4-year clinical history," *Med. Phys.* **28**, 1718-26 (2001).
- ²⁰S. C. Vieira, M. L. P. Dirkx, K. L. Pasma, and B. J. Heijmen, "Fast and accurate leaf verification for dynamic multileaf collimation using an electronic portal imaging device," *Med. Phys.* **29**, 2034-2040 (2002).
- ²¹T. Loncol, J. L. Greffe, S. Vynckier, and P. Scalliet, "Entrance and exit dose measurements with semiconductors and thermoluminescent dosimeters: a comparison of methods and in vivo results," *Radiother. Oncol.* **41**, 179-87 (1996).
- ²²L. E. Antonuk, "Electronic portal imaging devices: a review and historical perspective of contemporary technologies and research," *Phys. Med. Biol.* **47**, R31-R65 (2002).
- ²³E. M. Franken, J. C. J. de Boer, J. C. Barnhoorn, and B. J. M. Heijmen, "Characteristics relevant to portal dosimetry of a cooled CCD camera-based EPID," *Med. Phys.* **31**, 2549-51 (2004).
- ²⁴E. M. Franken, J. C. J. de Boer, and B. J. M. Heijmen, "Portal dosimetry with a fluoroscopic EPID: a general approach based on direct imaging of position dependent crosstalk kernels," *Radiother. Oncol.* **73**/Supplement 1, S153 (2004).
- ²⁵M. Kroonwijk, K. L. Pasma, S. Quint, et al., "In vivo dosimetry for prostate cancer patients using an electronic portal imaging device: demonstration of internal organ motion," *Radiother. Oncol.* **49**, 125-132 (1998).
- ²⁶B. J. M. Heijmen, K. L. Pasma, M. Kroonwijk, V. G. M. Althof, J. C. J. de Boer, A. G. Visser, and H. Huizenga, "Portal dose measurement in radiotherapy using an electronic portal imaging device," *Phys. Med. Biol.* **40**, 1943-1955 (1995).
- ²⁷P. Munro and D. C. Bouius, "X-ray quantum limited portal imaging using amorphous silicon flat-panel arrays," *Med. Phys.* **25**, 689-702 (1998).
- ²⁸E. E. Grein, R. Lee, and K. Luchka, "An investigation of a new amorphous silicon electronic portal imaging device for transit dosimetry," *Med. Phys.* **29**, 2262-2268 (2002).
- ²⁹P. B. Greer and C. C. Popescu, "Dosimetric properties of an amorphous silicon electronic portal imaging device for verification of dynamic intensity modulated radiation therapy," *Med. Phys.* **30**, 1618-27 (2003).
- ³⁰B. M. McCurdy, K. Luchka, and S. Pistorius, "Dosimetric investigation and portal dose image prediction using an amorphous silicon electronic portal imaging device," *Med. Phys.* **28**, 911-24 (2001).
- ³¹A. Van Esch, T. Depuydt, and D. P. Huyskens, "The use of an aSi-based EPID for routine absolute dosimetric pre-treatment verification of dynamic IMRT fields," *Radiother. Oncol.* **71**, 223-34 (2004).
- ³²L. N. McDermott, R. J. Louwe, J.-J. Sonke, M. B. van Herk, and B. J. Mijnheer, "Dose-response and ghosting effects of an amorphous silicon electronic portal imaging device," *Med. Phys.* **31**, 285-95 (2004).
- ³³J. H. Siewerdsen and D. A. Jaffray, "A ghost story: spatio-temporal response characteristics of an indirect-detection flat-panel imager," *Med. Phys.* **26**, 1624-41 (1999).
- ³⁴S. Warkentin, S. Steciw, S. Rathee, and B. G. Fallone, "Dosimetric IMRT verification with a flat-panel EPID," *Med. Phys.* **30**, 3143-55 (2003).

- ³⁵R. J. Louwe, L. N. McDermott, J.-J. Sonke, R. Tielenburg, M. Wendling, M. B. van Herk, and B. J. Mijnheer, "The long-term stability of amorphous silicon flat panel imaging devices for dosimetry purposes," *Med. Phys.* **31**, 2989-95 (2004).
- ³⁶G. V. Menon and R. S. Sloboda, "Quality assurance measurements of a-Si EPID performance," *Med. Dosim.* **29**, 11-17 (2004).
- ³⁷J.-J. Sonke, L. S. Ploeger, B. Brand, M. H. Smitsmans, and M. B. van Herk, "Leaf trajectory verification during dynamic intensity modulated radiotherapy using an amorphous silicon flat panel imager," *Med. Phys.* **31**, 389-95 (2004).
- ³⁸D. Verellen, N. Linthout, D. van den Berge, A. Bel, and G. Storme, "Initial experience with intensity-modulated conformal radiation therapy for treatment of the head and neck region," *Int. J. Radiat. Oncol. Biol. Phys.* **39**, 99-114 (1997).
- ³⁹D. A. Low, R. L. Gerber, S. Mutic, et al., "Phantoms for IMRT dose distribution measurement and treatment verification," *Int. J. Radiat. Oncol. Biol. Phys.* **40**, 1231-5 (1998).
- ⁴⁰Y. Aoki, A. Akanuma, P. M. Evans, D. G. Lewis, E. J. Morton, and W. Swindell, "A dose distribution evaluation utilizing megavoltage CT imaging system," *Radiat. Med.* **8**, 107-110 (1990).
- ⁴¹V. N. Hansen, P. M. Evans, W. Swindell, "The application of transit dosimetry to precision radiotherapy," *Med. Phys.* **23**, 713-721 (1996).
- ⁴²T. R. McNutt, T. R. Mackie, P. Reckwerdt, and B. R. Paliwal, "Modeling dose distributions from portal dose images using the convolution/superposition method," *Med. Phys.* **23**, 1381-1392 (1996).
- ⁴³R. Boellaard, M. van Herk, H. Uiterwaal, et al., "First clinical tests using a liquid-filled electronic portal imaging device and a convolution model for the verification of the midplane dose," *Radiother. Oncol.* **47**, 303-12 (1998).
- ⁴⁴K. Nakagawa, Y. Aoki, M. Tago, et al., "Megavoltage CT-assisted stereotactic radiosurgery for thoracic tumors: original research in the treatment of thoracic neoplasms," *Int. J. Radiat. Oncol. Biol. Phys.* **48**, 449-457 (2000).
- ⁴⁵J. M. Kapatoes, G. H. Olivera, K. J. Ruchala, et al., "A feasible method for clinical delivery verification and dose reconstruction in tomotherapy," *Med. Phys.* **28**, 528-542 (2001).
- ⁴⁶D. A. Jaffray, J. H. Siewerdsen, J. W. Wong, et al., "Flat-panel cone-beam computed tomography for image-guided radiation therapy," *Int. J. Radiat. Oncol. Biol. Phys.* **53**, 1337-1349 (2002).
- ⁴⁷M. Partridge, M. Ebert, and B. M. Hesse, "IMRT verification by three-dimensional dose reconstruction from portal beam measurements," *Med. Phys.* **29**, 1847-1858 (2002).
- ⁴⁸J. S. Welsh, K. Bradley, K. J. Ruchala, T. R. Mackie, R. Manon, R. Patel, P. Wiederholt, M. Lock, S. Hui, and M. P. Mehta, "Megavoltage computed tomography imaging: a potential tool to guide and improve the delivery of thoracic radiation therapy," *Clin. Lung Cancer.* **5**, 303-6 (2004).
- ⁴⁹J. H. Siewerdsen, D. J. Moseley, B. Bakhtiar, S. Richard, and D. A. Jaffray, "The influence of antiscatter grids on soft-tissue detectability in cone-beam computed tomography with flat-panel detectors," *Med. Phys.* **31**, 3506-20 (2004).
- ⁵⁰K. L. Pasma, M. L. P. Dirkx, M. Kroonwijk, A. G. Visser, and B. J. M. Heijmen, "Dosimetric verification of intensity modulated beams produced with dynamic multileaf collimation using an electronic portal imaging device," *Med. Phys.* **26**, 2373-2378 (1999).
- ⁵¹K. L. Pasma, M. Kroonwijk, S. Quint, et al., "Transit dosimetry with an electronic portal imaging device (EPID) for 115 prostate cancer patients," *Int. J. Radiat. Oncol. Biol. Phys.* **45**, 1297-303 (1999).

- ⁵²C. Ramsey and S. Dube, "Point/Counterpoint: It is necessary to validate each individual IMRT treatment plan before delivery," *Med. Phys.* **30**, 2271-2273 (2003).
- ⁵³K. L. Pasma, M. Kroonwijk, J. C. J. de Boer, A. G. Visser, and B. J. M. Heijmen, "Accurate portal dose measurement with a fluoroscopic electronic portal imaging device (EPID) for open and wedged beams and for dynamic multileaf collimation," *Phys. Med. Biol.* **43**, 2047-2060 (1998).
- ⁵⁴M. Essers, J. H. Lanson, and B. J. Mijnheer, "In vivo dosimetry during conformal therapy of prostate cancer," *Radiother. Oncol.* **29**, 271-279 (1993).

CHAPTER 9. SAMENVATTING

9.1 Inleiding

Kanker is de ongecontroleerde proliferatie en verspreiding van cellen en kan zich manifesteren in bijna het hele lichaam. Meeste kankers worden behandeld met chirurgie, bestraling (radiotherapie), en/of met medicijnen (chemotherapie). De stralenbron voor radiotherapie kan zich buiten de patiënt bevinden (teletherapie) of kan in de tumor ingebracht worden (brachytherapie). Met teletherapie worden de stralenbundels (meestal hoge energie fotonen of elektronen) afgegeven met behulp van een lineaire versneller. De patiënt wordt bestraald onder verschillende hoeken om een homogene dosis aan de tumor te kunnen geven en om tegelijkertijd een verspreiding (en dus een vermindering) van de dosis in de normale weefsels te bewerkstelligen. Teletherapie kan in twee stappen ingedeeld worden: de voorbereiding en de behandeling. De voorbereiding begint meestal met het maken van hulpstukken om de patiënt op de behandelingstafels te immobiliseren. Vervolgens worden CT beelden van de patiënt gemaakt en naar het computer systeem gestuurd waar de behandeling wordt gepland. Een cruciale stap is het intekenen van de tumor en de normale weefsels op de CT beelden, en het vaststellen van de gewenste dosis. Vervolgens wordt het optimale aantal bundels, de bundelenergie en bundelgewichten bepaald. Als het behandelplan klaar is en goedgekeurd door de radiotherapeut(e), begint de patiënt met de behandeling. De totale dosis wordt meestal gegeven in meerdere fracties (>25), verspreid over enkele weken.

In teletherapie worden meestal vlakke en statische stralenbundels gebruikt. Soms is het evenwel niet mogelijk om zo een homogene dosis in de tumor te verkrijgen en tegelijkertijd de normale weefsels te sparen. Dit hangt af van de locatie (of de vorm) van de tumor. Om dit te kunnen verbeteren worden tegenwoordig intensiteits-gemoduleerde bundels gebruikt. De meest eenvoudige manier om een bundel te moduleren is door een wig te gebruiken. Dat wil zeggen dat een wigvormig stuk metaal in de bundel wordt geplaatst. Voor meer gecompliceerde modulatie, zoals gewenst in intensity modulated radiotherapy (IMRT) behandelingen, kan een multi-leaf collimator (MLC) gebruikt worden. De computer gecontroleerde MLC is bevestigd aan de kop van de versneller en bestaat uit een groep van metalen “vingers”, ook wel “leaves” genoemd.

Omdat teletherapie een complexe procedure kan zijn en omdat kleine fouten ($\approx 5\%$) in de gegeven dosis de patiënt kan schaden, maakt de verificatie van de gegeven dosis

een belangrijk onderdeel uit van de radiotherapie. Verificatie van de dosis kan, onder anderen, met behulp van een electronic portal imaging device (EPID) gedaan worden. De EPID wordt achter de patiënt geplaatst en gebruikt de behandelingsbundels om een digitaal transmissie beeld van de patiënt te nemen. De gebruikte EPID in dit proefschrift heeft een fluorescerend scherm, een spiegel en een gekoelde CCD kamera. Het doel van dit proefschrift was om het gebruik van EPIDs voor dosis verificatie in IMRT te ontwikkelen en analyseren. Een van de uitdagingen was om exacte methoden te verzinnen om de kleine, maar belangrijke, afwijkingen in de gegeven dosis te kunnen bepalen. Om deze ontwikkelde methoden in de kliniek te kunnen implementeren, moeten zij nauwkeurig, makkelijk om te gebruiken, robuust en snel zijn.

9.2 De EPID en de dosis verificatie van gemoduleerde stralenbundels

Om de afgegeven dosis met de EPID te kunnen verifiëren, moet het corresponderende transmissie beeld geconverteerd worden naar een dosis beeld, oftewel een portal dose image (PDI). De afgegeven dosis is correct als de gemeten PDI gelijk is aan de berekende PDI tijdens de planning (die de gewenste dosis representeert). In hoofdstuk 2 wordt een methode gepresenteerd om de PDI te kunnen berekenen voor wig bundels. Deze methode is getest met behulp van fantoom metingen. Om inhomogeniteiten mee te nemen is onder andere een thorax fantoom gebruikt. De metingen zijn uitgevoerd met hoge energie fotonen bundels van 6 en 23 MV. De overeenkomst tussen metingen en berekeningen was ongeveer 1%. Deze resultaten tonen aan dat dosis verificatie van wig bundels met de EPID kan worden gedaan.

In hoofdstuk 3 gaat de verificatie van bundelmodulatie een stap verder en worden zeer sterk gemoduleerde bundels zijn bestudeerd. In deze studie is een functie ontwikkeld om de afwijkingen tussen EPID-metingen en referentie-metingen (in water of film) van de sterk gemoduleerde bundels te kunnen verminderen. De afwijkingen worden veroorzaakt door verschillen in lateraal elektronentransport en optische fotonen tussen referentiesituatie en EPID scherm. Na toepassing van de functie op de EPID beelden, waren de verschillen tussen de meting en berekening in het centrale gebied van de profielen kleiner dan 2%, en in het penumbra gebied kleiner dan 0.3 mm. De conclusie van deze studie is dat de EPID een geschikt dosis verificatie methode is voor IMRT, zelfs als sterk gemoduleerde bundels worden gebruikt.

9.3 MLC kwaliteitscontrole

IMRT bestraling met een MLC kan op twee manieren uitgevoerd worden: met segmented multi-leaf collimatie (SMLC) of met dynamische multi-leaf collimatie (DMLC). Met SMLC is de stralenbundel uit tijdens de beweging van de leaves, terwijl met DMLC de bundel aan blijft tijdens de leafbewegingen. Leaf positie nauwkeurigheid is cruciaal voor IMRT behandeling, omdat onnauwkeurigheden in de leafposities kleiner dan een millimeter aanzienlijke dosis verschillen kunnen veroorzaken. In hoofdstuk 4 en 5 worden snelle en dagelijks tests voor de verificatie van DMLC en SMLC bestraling voorgesteld. Voor DMLC is de verificatie methode gebaseerd op een vlak en bewegend veld van 0.5 cm breed. Afwijkingen in de veldbreedte voor elke leaf worden afgeleid van het EPID profiel, en niet van directe positiemetingen van de leaves in het beeld. Er is software was ontwikkeld om de ruis in de beelden te verminderen. Deze ruis wordt veroorzaakt door het lage EPID signaal dat wordt gemeten met gebruik van het bovengenoemd veld. In hoofdstuk 4 is aangetoond dat zeer kleinen fouten in leaf positie (0.1-0.2 mm) kunnen worden gedetecteerd. Het is ook aangetoond dat de korte- en de lange termijn reproduceerbaarheid van de leafpositie voor alle gantry hoeken kleiner is dan 0.1 mm (1 SD).

In hoofdstuk 5 is een gelijksoortige procedure ontwikkeld voor de SMLC techniek. De test is gebaseerd op metingen voor Elekta, Siemens en Varian versnellers, gedurende een periode van 3 tot 8 maanden. Op elke meetdag zijn EPID beelden gemaakt van een veld met vijf langwerpige segmenten ($3 \times 22 \text{ cm}^2$) met elk 10 monitor eenheden (ME). De afwijkingen van de afstand tussen de leaves ten opzichten van de verwachte waarden zijn geanalyseerd. De hysteresis van de leafpositie is bestudeerd door de SMLC segmenten in omgekeerde volgorde te bestralen. De lange termijn reproduceerbaarheid van de afstand tussen de leaves (1 SD) was 0.09 mm, 0.22 mm, and 0.21 mm voor respectievelijk de Varian, de Siemens, en de Elekta versnellers. In alle gevallen, was de hysteresis verwaarloosbaar. Om de constantheid van de bundel met lage dosis te bestuderen, is een statisch $20 \times 20 \text{ cm}^2$ veld bestraald met ME waarden van 1 tot 50 ME. Voor bestralingen van 2 ME of hoger, waren de bundel output en de bundel profiel stabiel binnen respectievelijk 2% e 1%, voor alle versnellers. Bovenstaande bevindingen hebben geresulteerd in een snelle procedure (3-4 minuten) voor nauwkeurige en dagelijkse kwaliteitscontrole van een SMLC versneller.

9.4 Patiëntbehandelingen met IMRT

Sinds het begin van de radiotherapie, worden patienten tijdens de behandeling op een tafel gelegd. Tegenwoordig, met het gebruik van IMRT, komt het vaker voor dat de stralenbundels door de tafel en/of door immobilisatiehulpstukken heen stralen. In het zesde hoofdstuk, wordt de EPID gebruikt om de bundelverzwakking door de tafel en de immobilisatiehulpstukken te meten. De bundel verzwakkingen kunnen oplopen tot 15%, zelfs wanneer moderne, commerciële koolstof onderdelen worden gebruikt. Als gevolg van deze resultaten, is een hulpmiddel ontwikkeld waar tekeningen van de tafelstructuur en mogelijke bundel hoeken over elkaar heen geprojecteerd worden. Op deze manier worden de bundel intersecties met de tafel vermeden. Dit wordt tegenwoordig gebruikt tijdens de planning van de bestraling.

Tijdens de behandeling kunnen grote afwijkingen gevonden worden tussen de gemeten en de berekende PDI. Deze afwijkingen kunnen veroorzaakt worden door patiënt bewegingen tijdens de bestraling of door fouten in de gemoduleerde bestralingsbundel. In hoofdstuk 7 wordt een nieuw techniek, genaamd Split IMRT Field Techniek (SIFT), voorgesteld om dit probleem op te lossen. Met deze techniek wordt de bestraalde fluentie geverifieerd onafhankelijk van veranderingen in de patiënt geometrie. De methode is gebaseerd op de splitsing van het IMRT veld in een statisch (niet gemoduleerd) veld en een overblijvend gemoduleerd veld. Door de beelden door elkaar te delen kan een onderscheid gemaakt worden tussen veranderingen in patiënt geometrie fouten en fouten in de stralenbundel. Op deze manier een fundamenteel probleem van transmissie dosis metingen wordt opgelost. De geschiktheid van SIFT is aangetoond met behulp van fantoom metingen. De klinische implementatie van deze techniek is gedemonstreerd voor prostaat en hoofd/hals kanker patiënten. De fluentie kan geverifieerd worden met een nauwkeurigheid van 1% (SD), zelfs in geval van grote inter-fractie veranderingen in de patiënt geometrie plaatsvinden. De bestralingstijden met het gebruik van SIFT nemen weinig toe ten opzichte van de standaard IMRT.

LIST OF ABBREVIATIONS AND SYMBOLS

ADC	analog to digital conversion
CCD	charge coupled device
CT	computer tomography
DMLC	dynamic multileaf collimation
DNA	desoxyribo nucleic acid
DRR	digitally reconstructed radiographs
DVH	dose volume histogram
EHP	equivalent homogenous phantom
EPID	electronic portal imaging device
IC	ionisation chamber
ICRU	international commission of radiation units and measurements
IDL	interactive data language
IMAT	intensity modulated arc therapy
IMRT	intensity modulated radiotherapy
LDA	linear diode array
MLC	multileaf collimator
MRI	magnetic resonance imaging
MV	megavoltage
MU	monitor units
NSCLC	non-small cell lung cancer
NAL	no action level
PDI	portal dose image
PET	positron emission tomography

QA	quality assurance
SD	standard deviation
SDD	source to detector distance
SIFT	split IMRT field technique
TLD	thermo luminescence detector
TPS	treatment planning system
1D	one dimensional
2D	two dimensional
3D	three dimensional

ACKNOWLEDGMENTS

The first thought that came into my mind when I was beginning to write this section was that I would surely forget someone of the many people who collaborated in this thesis. So my first thanks go to that someone that I am almost certainly forgetting.

And furthermore....

To Ben Heijmen, my supervisor, for the always lively and interesting discussions, and for being there since the very beginning of this PhD. Doing research in another country is not easy, you understood that perfectly and supported me all the way, making this PhD happen.

To Maarten Dirkx, for his constant support and for having the patience of reading most of my manuscripts first hand. A PhD is a sum of stress with a lot of work, and you brought structure to all this and kept this PhD “on track”. Without you, I bet things were just going to be much more chaotic.

To my colleagues and co-authors, Hans de Boer, René Bolt, Robert Kaatee, and Kasper Pasma for their useful comments and support, and for teaching me all that I had to know about EPIDs. Working in the same room with Kasper and Hans, and talking with Robert, when I was just starting to find out what an EPID was, help me immensely and shortened considerably the time that I would certainly need to conclude this thesis. To René for his comments, interest, and for the frequent contact despite the distance between Nijmegen and Rotterdam. Our emails were so loaded with information that I had to print them all the time in order to be able to read them properly.

To Andries Visser for allowing me to come to Holland in the first place, and although I did not know at the time, for being the start of this thesis.

To Erik Loeff, Adri van den Biggelaar, and Martijn Hol, for helping me with the evening measurements and for turning a long evening into a pleasant laugh. To Jaco Barnhoorn, for answering all the questions about TNT that I bothered him with.

To my colleagues from de Daniel den Hoed, with Gerard Schaap as the “stuurman”, and to my ex-colleagues for always keeping it “gezellig” in the form of survival weekends, dinners, and visits to the Rotterdam film festival, and also for putting up with my Dutch. No doubt, the atmosphere in de Daniel den Hoed made what would

be at first a three-month stay for training in brachytherapy, into a 5 year one. And because the atmosphere starts actually in your working room, I would like to thank my recent roommates: Eric Franken and Valentina Schembri. To Eric for being always available for discussion about EPID dosimetry and for immediately being ready to go pay a visit to the cafeteria downstairs and fetch “snoepjes”, making me feel less guilty about it. To Valentina for bringing me the ways of the Mediterranean into my working space in Rotterdam (now I am not the only one who speaks mainly using the hands!). Tu sei molto brava.

To the department of MEA for explaining me the particularities of the accelerators. Especially to Martijn Laarhoven and to Hans Groen for teaching me about multileaf collimators and their calibration. Despite my constant questions about all the details, you were always very supportive and open for discussion.

To Bert van Wijk, Nadine Post, and other technicians for their help and availability. Implementation of research projects in clinical practice can be quite demanding, especially when there are few people to do the work and too much stress. With Ben and Nadine in command, things went quite fast and easy. To Theresa O’Neill for helping me with multi-access.

To the “automatisering” guys: Hafid Akhiat, Norman Driver, Bart Kanis, and Bert van der Leije, for solving all my computer problems avoiding me having a heart attack.

To the trainees Remco Dekker, Carmen Panneman, and Gijs van Schelven, for their contribution to this thesis and for their “simpatia”.

To the commission members under the supervision of Peter Levendag for reading this thesis and for their comments. Additionally to the names of members of the inner doctoral commission already mentioned in the cover of this thesis I would like to acknowledge the members of the plenary doctoral commission: Carel van Eijk, Frans van der Helm, and Ton van der Steen.

To the inhabitants of the “kippenhok” Jacqueline van der Valk-de Geus, and Jolanda van den Heuvel (also known by J&J), and to Lida Walburg for their support throughout this thesis, which included a wide range of things from helping me with the most difficult words in Dutch to telling me where to go for vaccination. J&J, you made me invent a new Dutch word: “chocoladegezelligheid”.

To Mieke Dekker and Carlos “Francês”, my “paranimfen”. To Mieke for the talks, for the lovely dinners together with Erik Loeff, and for always being positive. You are a

daring women! To Carlos for his support and friendship since the university days who by “forces of nature” now lives in neighbour Belgium.

And last but not least...

To my mother, sempre perto apesar de longe.

To my father and my sister, for being my supporting team in Portugal. Cada vez que volto a Portugal sinto-me a pessoa mais mimada do planeta. As muitas horas que passámos (e ainda passamos) ao telefone nunca são demais! To Joep, my supporting team in the Netherlands (yes, you are worth a team), for making things much easier. A Holanda mudou completamente depois de ti. Without these two teams, this “ride” would have been certainly longer and less smooth.

CURRICULUM VITAE

Sandra was born in 1971 in Lisbon, where she lived and studied. In 1989, she concluded her high school at the Liceu Pedro Nunes, and began her University studies in Physics in the University of Sciences in Lisbon (1989-1994). During the last year of her university, Sandra had the first contact with the radiotherapy field, by doing training in the department of radiotherapy of Santa Maria Hospital, in Lisbon. During this year, she had the opportunity to collaborate in the clinical implementation of radiosurgery, which resulted in the irradiation of the first patient with this technique in Portugal. This work was the theme of her dissertation with which Sandra got her university degree.

Afterwards, Sandra proceeded her study with a masters degree in Medical Physics and biomedical engineering at the University of Sciences (1995-1997), which she concluded with a dissertation on “Semiconductor detectors in Radiotherapy”.

Sandra initiated her professional activity working as a physicist in the radiotherapy department of the Santa Maria hospital (1997-2000). In 1998, she had her first professional contact with Holland when she went to do a 3 months training in brachytherapy at the Daniel den Hoed Cancer Center in Rotterdam. She had then the opportunity to mingle with the locals, taste haring, eat the delicious poffertjes, and dive into the divine chocolate “Droste”. For these, and other reasons too, Sandra decided to come back to Holland to do her PhD thesis in the Daniel den Hoed Cancer Center, which she has now (almost) completed.

